BRNO UNIVERSITY OF TECHNOLOGY

VYSOKÉ UČENÍ TECHNICKÉ V BRNĚ

FACULTY OF ELECTRICAL ENGINEERING AND COMMUNICATION

FAKULTA ELEKTROTECHNIKY A KOMUNIKAČNÍCH TECHNOLOGIÍ

DEPARTMENT OF PHYSICS

ÚSTAV FYZIKY

SYNTHESIS AND CHARACTERIZATION OF MULTIFERROIC THIN FILMS

SYNTÉZA A CHARAKTERIZACE MULTIFERROICKÝCH TENKÝCH VRSTEV

HABILITATION THESIS

HABILITAČNÍ PRÁCE

AUTHOR — Mgr. Dinara Sobola, Ph.D.

AUTOR PRÁCE

BRNO 2020

Abstract

Promising application potential and attractive physical phenomena brought multiferroic materials in the center of scientific interest, but development and production of structures for current technologies applications are stuck at material level. Presence of a large amount of parameters and factors that influences the properties of resulting materials forces scientist to work with epitaxial growth. Considering intriguing physical phenomena, this approach has a huge impact for fundamental science. Anyway, rapid development of electronics demands implementation of new prospective materials to existing techniques. Heteroepitaxial growth offers advances for design and engineering applications, which is essential for building integrated multiferroic sensors.

In this work I focus on deposition of bismuth ferrite (BFO) thin films on the foreign substrate and justification of the substrate's choice. BFO is of greatest interest for practical use, since it is the only single-phase material exhibiting both ferroelectric and antiferromagnetic ordering at room temperature. However, due to structural features, the magnetoelectric effect is suppressed in bulk materials. The transition to multiferroic phase requires huge magnetic fields (20 T) or a reduction in the size of structures (62 nm). Obtaining of BFO in the form of the thin film solve this problem. Decreasing of the size and deliberate creation of oxygen vacancy by variation of preparation parameters as well as defects, for example by ion etching, are technologically advanced ways of destruction of spin cycloid.

Structure of this habilitation thesis includes description of possible phases in Bi-Fe-O system and the most promising methods for thin films preparation as atomic layer deposition and pulse layer deposition. Supplementary material in appendixes contains more detailed information about materials (HOPG, SiC) that were chosen as substrates for BFO deposition. Among all characterization methods, a special attention is given to scanning probe microscopy, since this is the method to local non-destructive control of mechanical, piezoelectric and magnetic properties of the samples.

Novelty of this work is description of solid state-reaction on the graphite substrates for optimization of heterostructures preparation suitable in nowadays electronics applications. The experiments on preparation of BFO/TiO_2, BFO/Kapton, BFO/Pt/SiO_2/Si, BFO/HOPG and BFO/SiC were done and the most valuable issues in structure and properties are presented in this work. Research opportunities and preliminary issues are emphasized and outlined.

The pedagogical part of this habilitation is presented in a form of a summary of my recommendations and new methods for initiating newcomers into the arts of scanning probe microscopy and further development of their skills in this field. The recommendations are structured in such a way to best guide the learning process in an appropriate and effective manner to achieve understanding of the workings of the system, its advantages and limitations.

Abstrakt

Slibný aplikační potenciál a atraktivní vlastnosti vynesly multiferoické materiály do centra vědeckého zájmu, ale vývoj a výroba struktur pro technologie dnešní doby jsou limitovány možnostmi přípravy materiálu. Přítomnost velkého množství parametrů a faktorů ovlivňujících vlastnosti výsledného materiálu nutí výzkumníky využívat především epitaxní růst. Když vezmeme v potaz zajímavé fyzikální jevy, má tento přístup velký dopad na základní výzkum. Každopádně, rychlý vývoj elektroniky vyžaduje zařazení nových slibných materiálů do existujících postupů. Heteroepitaxiální růst nabízí možnost postupu v designu elektronických elementů, což je nezbytné pro konstrukci integrovaných multiferoických senzorů.

V této práci se soustředím na depozici tenkých vrstev feritu bizmutu (BFO) na cizí substrát a zdůvodnění jeho použití. BFO je výborné pro praktické využití, protože je to jediný jednofázový materiál, který má feroelektrické a antiferomagnetické uspořádání za pokojové teploty. Nicméně, kvůli strukturálním vlastnostem je magnetoelektrický jev potlačen v objemových materiálech. Přechod na multiferoickou fázi vyžaduje silné magnetické pole (20 T) nebo redukci velikosti struktur (62 nm). Získání BFO ve formě tenké vrstvy tento problém řeší. Zmenšení velikosti a záměrné vytvoření kyslíkových vakancí pomocí výběru parametrů přípravy a také pomocí defektů, například iontovým leptáním, jsou technologicky pokročilé způsoby destrukce spinové cykloidy.

Struktura této habilitační práce obsahuje popis možných fází v Bi-Fe-O systému a nejslibnější metody pro přípravu tenkých filmů pomocí metody depozice atomových vrstev nebo pulzní laserové depozice. Doplňkové zdroje v přílohách obsahují detailnější informace o materiálech (HOPG, SiC), které byly vybrány za substráty pro depozici BFO. Ze všech charakterizačních metod byla nejvíce používána skenovací sondová mikroskopie, protože je to nejvhodnější metoda pro lokální nedestruktivní kontrolu mechanických, piezoelektrických a magnetických vlastností vzorků.

Inovace této práce spočívá v popisu reakcí na povrchu grafitového substrátu pro optimalizaci přípravy heterostruktur vhodných pro dnešní elektronické aplikace. Byly provedeny experimenty s přípravou BFO/TiO_2, BFO/Kapton, BFO/Pt/SiO_2/Si, BFO/HOPG and BFO/SiC a nejcennější poznatky o struktuře a jejích vlastnostech jsou popsány v této práci. Výzkumné možnosti a předběžné problémy jsou zdůrazněny a nastíněny.

Pedagogická část mé práce je zařazena do habilitace ve formě přehledu mých doporučení a nových metod pro zasvěcení nových pracovníků do umění skenovací sondové mikroskopie a následné kultivace jejich dovedností v této oblasti. Tato doporučení jsou strukturována takovým způsobem, aby co nejlépe vedla proces učení vhodným a efektivním způsobem pro dosažení porozumění funkcí této metody, jejích výhod i omezení.

Keywords: atomic layer deposition, pulse laser deposition, bismuth ferrite, highly oriented pyrolytic graphite, scanning probe microscopy

Klíčová slova: depozice atomových vrstev, pulzní laserová depozice, ferit bizmutu, vysoce orientovaný pyrolytický grafit, skenovací sondová mikroskopie

Acknowledgments

My deep gratitude goes to Prof. Ing. Lubomír Grmela, CSc., head of the Physics Department, Faculty of Electrical Engineering and Communication, Brno University of Technology, for his constant support, as well as to our working team in the Physics Department for encouragement in my work, especially to Ing. Pavel Kaspar, Ph.D.

I would like to express great thanks to my friend and colleague Dr. Ramazanov from Dagestan State University for his precious advice, and for all his devoted time.

I also gratefully acknowledge help of colleagues from CEITEC BUT with samples preparation and compositional analysis.

I thank my family and my friends for their emotional support.

Research described in this thesis was supported Ministry of Education, Youth and Sports of the Czech Republic under the project CEITEC 2020 (LQ1601). CzechNanoLab project LM2018110 funded by MEYS CR is gratefully acknowledged for the financial support of the measurements/sample fabrication at CEITEC Nano Research Infrastructure.

CONTENTS

List of figures

List of tables

INTRODUCTION

Multiferroics are a class of crystalline solids in which at least two of the three types of order coexist: magnetic, electrical, or mechanical. Particularly, the attention is increased to multiferroics, in which magnetic and electrical ordering are present simultaneously. Progress in the field of materials for electronics on oxide systems (high-temperature superconductivity, giant magnetoresistance) led to the discovery of materials that exhibit magnetoelectric properties at room temperatures and in magnetic fields. Nevertheless, study of stable stress structures for preparation of magnetoelectric functional devices is of current interest.

In 2000 the paper named “Why Are There so Few Magnetic Ferroelectrics?“[1] was published. Despite the fact that the phenomenon of electromagnetism has been known since the 60s, recently this direction has attracted enormous attention. 11 years later, an article with the opposite name was published «Multiferroic magnetoelectric fluorides: why are there so many magnetic ferroelectrics?»[2]. Previous works [3] noted bismuth ferrite as only one single phase room temperature multiferroic material. It makes scientific and applied results regarding Bi-Fe-O system useful for potential application in microelectronics, nanotechnology, energy, communications technology and medicine.

The character of the magnetoelectric effect depends not only on the phase composition, but also on the crystallite size of bismuth ferrite. According to practical [4] and theoretical [5] studies, the magnetoelectric properties of bismuth ferrite are observed in the case of suppression of a spatially modulated spin cycloid (rotation of the spins along the direction of the wave vector) with 62 nm period. In comparison with a large number of works devoted to the study of obtaining of nano-sized bismuth ferrite (nanopowders, nanowires, nanorods, nanosheets, nanoflowers, etc.[6]), its doping methods and properties, there is a gap in understanding of the Bi-Fe-O system formation in form of heterostuctures.

Herbert Kramer, the 2000 Nobel Prize winner in Physics, said that "the interface is the device". It is clear that epitaxial growth allows one to obtain higher-quality films with a low defect density, with the possibility of controlling the structure from monocrystalline to polycrystalline with a defined orientation. But defects, vacancies and active centers arising due to mechanical stresses of the film-substrate interface are responsible for inhomogeneous distribution of charge and spin densities. Distortions and displacement of structure contribute to spontaneous polarization. Substrate material determines the type of growth and the presence of stress in the film.

Structures based on multiferroics can become the basis of spintronics, memory modules, electrically switched magnets, MEMS, sensors and devices of the terahertz range. The properties and, consequently, application potential of films grown by various deposition methods differ significantly and their morphology strongly depends on the substrate material. For this reason, the study of multiferroics, namely, obtaining accurate and reliable data on the processes of nucleation, growth, stability, is a relevant scientific field.

1. MOTIVATION

Over the past 15 years, new device technologies that aimed at replacing or supplementing the limited scaling of flash memory have become widespread. Memristive devices are the most promising for creating next-generation memory cells, as they have low power consumption and provide high integration density and access speed [7]–[12].

In recent years, researches have been actively investigated the possibility of controlling resistive switching with the help of various external influences. Additional control parameters for resistive switching can significantly expand the scope of application of memristive devices. There is evidence that visible radiation can be used as a new resistive switching control tool [13]–[15]. Some papers have reported using a magnetic field as an additional control tool [16]–[18]. It was reported that «diluted magnetic semiconductors», as a result of the exchange interaction, possess both spin and charge degrees of freedom [19], which ensures the internal ability to control ferromagnetism by electric fields. However, the main disadvantage of the majority of published studies on this topic is that these effects were found at low temperatures (less than 200 K), limited by the Curie temperature [20]–[22]. In 2011, Yamada et al.[23] showed the presence of ferromagnetism induced by an electric field in a diluted magnetic semiconductor oxide (Ti-Co)O_2 at 300 K, which gave impetus to the development of memristive devices of semiconductor spintronics operating at room temperature. However, the carrier density varied within small limits at various voltages. In this regard, it is relevant to develop memristive devices in which resistive switching can be obtained by inducing magnetic modulation, which can provide a unique opportunity to encode information in these states to obtain four logical states.

Recently, interest in the generation and detection of terahertz electromagnetic waves has increased. A number of new methods were proposed, including the use of such “new” materials as grapheme [24] and carbon nanotubes [25], [26]. One of the promising directions is the use of spin injection in magnetic transitions [27], [28], resulting in the inverse population of spin energy subzones. The authors of papers [29], [30] under the leadership of Yu.V Gulyaev (academician of the Russian Academy of Sciences in the town of Fryazino) obtained experimental results confirming the possibility of generating THz radiation from the use of magnetic transitions. In this connection, interest arises in systems which are resonant in the terahertz region and could be used as receivers of THz radiation.

According to an analytical company Webfeet Research in 2016 the turnover of the non-volatile memory market amounted to 48.4 billion US dollars. Toshiba and SanDisk also postponed the transition to Resistive Random Access Memory (RRAM) until 2020. The following companies are involved in the development of THz radiation detectors and their serial sales: LASER COMPONENTS (Germany); Laser Components, Standa Ltd, (Lithuania); TK Instruments (UK); LASER BLV (USA). Most commercial THz detectors operate on the basis of pyroelectric or thermoelectric (THz-D) effects and their average cost is about 12 million rubles. Under the guidance of Mona Jarrahi, an assistant professor of electrical engineering and computer science, and members of the University of Michigan research team, a super-sensitive terahertz source and detector system were developed.

All these studies were accompanied by intensive work in the field of solid-state physics and chemistry. The scientific interest lies in the fact that the film-substrate interface may have properties that are not observed at epitaxially grown film, nanopowder, or bulk material. The film-substrate interface can create the prerequisites for the magnetoelectric effect, which can propagate in the thickness of the material. Due to the distortion of the crystal structure, it is possible to achieve high values of spontaneous polarization and the destruction of cycloidal ordering (Fig. 1.1), which will ensure the presence of antiferromagnetic ordering with weak ferromagnetism.

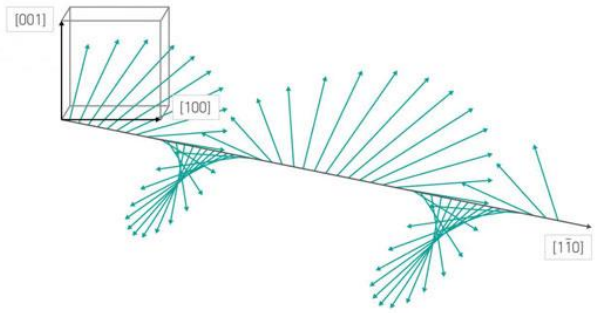

Figure. 1.1. The spin cycloid structure in $BiFeO_3$ [5], [31].

In addition, heteroepitaxy also allows one to obtain structures with a sharp interface when it is necessary to avoid the mixing effect, as is required in the preparation of tunnel barriers. The feasibility of deposition on substrates from other materials is also explained by the elaboration of the process for their preparation, wide distribution, accessibility, and relatively low cost.

2. METHODOLOGY

2.1. Phases of Bi-Fe-O system

Bi-Fe-O based compounds have a wide range of features that are of interest both for basic science and for applied research. The Bi-Fe-O material, identical in chemical composition but different in structure, has a number of promising optical, magnetic, electrical, and mechanical properties. Practically significant is the ability to control and manage these properties through external influences. The problems of materials science, which can be found in pure phase preparation, make the progress of Bi-Fe-O adaptation slower for new-generation electronic devices as spintronic, quantum optics, magnetooptics, etc

In the presence of a mixture of phases, each contributes to the magnetic properties. $Bi_2Fe_4O_9$ - antiferromagnet with Néel temperature of 264 K; $Bi_{25}FeO_{39}$ - Paramagnet (from 5 K to 950 K) (from 5 K to 950 K) [32], ferrimagnetic and paramagnetic regions of $Bi_3Fe_5O_{12}$ was found to be reported on yttrium iron garnet substrates [33]. Each phase individually has a number of features that expand the use of the Bi-Fe-O system in various fields of science and production.

Thus, $Bi_2Fe_4O_9$ is promising for the manufacture of semiconductive chemical gas sensors and as a cheap replacement of catalysts in the oxidation of ammonia to NO in industrial production of nitric acid. It has a photocatalytic activity for organic contaminant with absorption in near-infrared region [34]. $Bi_2Fe_4O_9$ electrode is reported to be a photoanode for solar water splitting [35]. $Bi_2Fe_4O_9$ has an orthorhombic structure of mullite, a space group Pbam with coexistence of [FeO_6] octahedra and [FeO_4] tetrahedra and its band gap with reported to be 1.57 - 2.01 eV [36].

$Bi_{25}FeO_{39}$ in nanodispersed state also exhibits photocatalytic properties in the visible range (during the decomposition of phenol and orange methylene), however, it is inferior to the properties of $BiFeO_3$ and $Bi_2Fe_4O_9$. Besides optical and piezoresponse, its humidity sensing application was recently mentioned due to effect of rendering charge carriers caused by water [37]. $Bi_{25}FeO_{39}$ has a cubic structure of selenite with space group I23 [38]. Electrical properties of this was reported as mixed conductor of oxide ions and electronic holes [32].

Amorphous Bi-Fe-O nanoparticles was shown in recent works [39] to have photo-Fenton-like catalytic activity for typical organic contaminant RhB. Band gap $2.2 \sim 2.8$ eV make it useful for photo catalysts activated by visible-light. Amorphous composition prepared with Zn inclusion indicates speromagnet structure [40]. Such structures was recently reported for “ideal” high-entropy alloys [41].

The greatest interest of researchers is attracted to the $BiFeO_3$ phase due to the presence of the magnetoelectric effect at room temperature. Pseudocubic unit cells are interconnected along a diagonal line passing through their center. This arrangement forms a rhombohedral, ABO_3 distorted perovskite structure. An electric dipole moment is formed as a result of the displacement of bismuth atoms relative to the FeO_6 octahedron. For the presence of the piezoelectric effect, the paired bismuth electrons (6s2) respond. The partially filled 3d orbitals of ferric iron determine the presence of antiferromagnetism. In the R3c crystal structure, spontaneous polarization arises in the [111] direction of 6.1 μC cm^2, and in the direction [100]

with magnitude of 3.5 μC cm^2. The properties could by tuned by variation of morphology, thickness, microstructure, crystallinity [42].

2.2. Technology for preparation

The presence of a large number of methods for producing multiferroics, as well as the influence of various parameters on the resulting sample, makes the assessment of their properties a challenging task. Pulse laser deposition (PLD) and atomic layer deposition (ALD) are effective methods for the low-temperature synthesis of thin bismuth ferrite films. The ability to vary temperature over a wide range is important in the production of functional structures of optical devices (optical sensors, solar cells, light-emitting diodes) and electronics (memory cells, magnetic field sensors, etc.) due to the possible reaction of other materials and components to the temperature.

2.2.1. Atomic Layer Deposition

Atomic layer deposition belongs to a group of methods based on chemical processes. This technology is based on sequential chemical reactions between the gaseous precursor and the substrate material. When using multiple precursors to produce films of complex composition, the precursors are introduced alternately. As a result of repeated reactions of precursors with a surface, a thin film is deposited. The ALD process is a self-regulatory process. Due to the fact that the reactions are self-limiting, the amount of precipitated material in each reaction cycle is constant. Self-limitation of surface reactions makes it possible to control deposition at the atomic level.

ALD supports the use of large geometric dimensions of samples with high uniformity. Substrates can be of various shapes and structures. It is also possible to obtain films of transparent conductive coatings with good optical and electrical characteristics at relatively low substrate temperatures. The advantage of ALD over other epitaxy methods (plasma layer deposition, magnetron sputtering, electron beam sputtering) is the possibility of more detailed control of growth. This avoids the violation of stoichiometry and structure of the films. ALD provides choice of various precursors and options for the Bi-Fe-O composed films preparation. It creates opportunities for controlling stoichiometry and perfection of the films. At the same time, this complicates the task of evaluation of the properties and parameters of the prepared structures before the processed will be completely tuned. By varying the concentration of precursors interacting with the surface layer of the substrate material, it is possible to self-organize nanoparticles of individual reaction components on the surface without additional thermal annealing.

The literature provides information about the production of films of bismuth ferrite by ALD method and the experience of foreign researchers in this direction. The best quality nanolayers were obtained by the authors [43]. They report the preparation of Bi-Fe-O epitaxial thin films grown by the ALD method on single-crystal (001) $LaAlO_3$ and (001) $SrTiO_3$ substrates. When growing films on (001) $LaAlO_3$ using laser sputtering, due to the high mismatch of the lattice parameters and the corresponding epitaxial deformation, the $BiFeO_3$ film structure becomes

tetragonal and exhibits ferroelectric properties that are different from the rhombohedral modification. At the same time, $BiFeO_3$ films on (001) $LaAlO_3$, obtained by the ALD with subsequent annealing, demonstrate stress relaxation and the absence of periodic misfit dislocations. Since Bi-Fe-O films are grown from organometallic precursors, carbon atoms are present as in them an impurity, which negatively affects the dielectric properties. This leads to an increase in leakage current and the emergence of charge trap centers; therefore, control of carbon impurity is important for achieving the desired ferroelectric and dielectric properties of oxides grown by ALD.

2.2.2. Pulse Laser Deposition

The method of pulsed laser spraying belongs to the group of methods of physical deposition from the gas phase. The process of laser ablation occurs when focusing high-power laser radiation on the surface of a solid target. The effect of the laser on the substance leads to the rapid absorption of radiation energy, heating and explosive evaporation of the substance from the target surface. The process is accompanied by the propagation of a shock wave in the environment. As a result of the interaction of radiation with the target material, the matter is removed from the target and ionized. The resulting hot plasma expands, during the expansion, the plasma experiences additional heating by laser radiation. Depending on the intensity of the laser radiation, the ablation products can be either atoms, ions, molecules of a substance, or formed clusters and nanoparticles emanating from a zone of exposure with high kinetic energy. Atoms ablated at high temperature can interact with environmental molecules to form new compounds.

Deposition can also be accompanied by partial mixing of the surface layer due to thermal motion and diffusion. An increase in the energy of the laser flow, accompanied by an increase in ionic collisions, can compensate for a decrease in the temperature of the substrate, which in turn will lead to an increase in the crystallization of the film. The required chemical composition of the film is achieved by varying the gas pressure, the temperature of the substrate during deposition, and the modes of subsequent annealing and the type of gas used during it.

The energy of the deposited material flow affects the adhesion coefficients and the formation of chemical bonds. This has a double effect: on the one hand, it can be effectively used to control the film growth mechanism, and on the other, it leads to modification of the surface of the sprayed target. As a result, the selected power of the deposition laser affects not only such parameters of the film as the crystal structure and orientation of the film, density and content of defects, but also the composition of the film due to degradation of the initial material. The high energy of the erosive laser emitter particles allows the synthesis of films at low (down to room) substrate temperatures.

As for the distance from the target to the substrate, it is usually chosen empirically, taking into account the characteristic distance of the plasma. This is the distance over which the flow loses direction and disperses. There are several models describing optimal geometry: the model of a “strong shock wave”, “entrainment force”, etc.

The electrical and optical parameters of samples obtained by pulsed laser deposition even at room temperature of the substrate are comparable with the parameters of films obtained by other methods at higher temperatures.

However, despite the technological simplicity, physical phenomena such as self-atomization, the interaction of atoms with the surface, kinetic diffusion, island formation, and the shadow effect complicate the explanation of the film growth mechanism.

The data about growth bismuth ferrite of PLD present in literature. Mostly it concerns such substrates as SrTiO3 [44], $SrRuO_3$[45], FTO glass [46], and even specific like $Ca_{0.96}Ce_{0.04}MnO_3$ [47],etc. The structures proved to be prospective besides ferroelectricity and magnetic ordering, even demonstrated photovoltaic behavior. Nevertheless, a number of questions, such as influence of oxygen vacancies or type of electrode (or substrate) material are s till open for discussion.

Advantages of PLD:

- ✓ with the exception of the cleaning, there is no need to activate the surface of the substrate;
- ✓ simple and chemically pure synthesis of end products;
- ✓ high degree of compliance of cationic stoichiometry of the formed films with the composition of the target material;
- ✓ the possibility of the formation of metastable phases;
- ✓ high deposition rate of thin films;
- ✓ direct relationship between the energy parameters of radiation and the kinetics of layer growth;
- ✓ obtaining films with a high degree of crystallinity;
- ✓ strict dosage of material supply, including multi-component ones with high evaporation temperature.

Disadvantages:

- the possibility of contamination of the film by the products of the melt of the target material at high laser powers;

- small geometric sample size.

2.3. Probe characterization techniques

Application of scanning probe microscopy (SPM) is essential for the description of surface properties. In comparison with other techniques of surface imaging (scanning electron microscopy or optical methods) SPM is more reliable for 3D analysis of the surface topography or modification of the surface with precise values of Z-axis. The most widespread SPM type is atomic force microscopy (AFM). Basis of the AFM measurement process is the interaction between a probe and a sample surface.

In addition to topography with real values of heights, AFM has a number of modes that make possible studying the electrical and magnetic properties of materials. The use of scanning microscopy of the piezoelectric response (PFM) and magnetic force microscopy (MFM) was described in [48], [49]. In the study of magnetoelectric materials, AFM measurements using a conductive probe allows both local (units of nanometers) polarization of the sample and measurements its characteristics the microscale.

The results allow evaluation of the domain structure, including the size and morphology of the domains. In addition to recording the displacement of the probe due to presence of electric and magnetic domains, it is possible to carry out the polarization of surface areas and its subsequent registration. The use of external influences (temperature, magnetic field) and various configurations of the electrodes allow in-situ determination of the physical characteristics of the samples (Fig.2.1). The probe is in the form of an elastic cantilever with a sharp tip (10 nm) on its free end is used in this work for PFM and MFM. It allows to trace surface topography and its electrical properties with nanometer resolution.

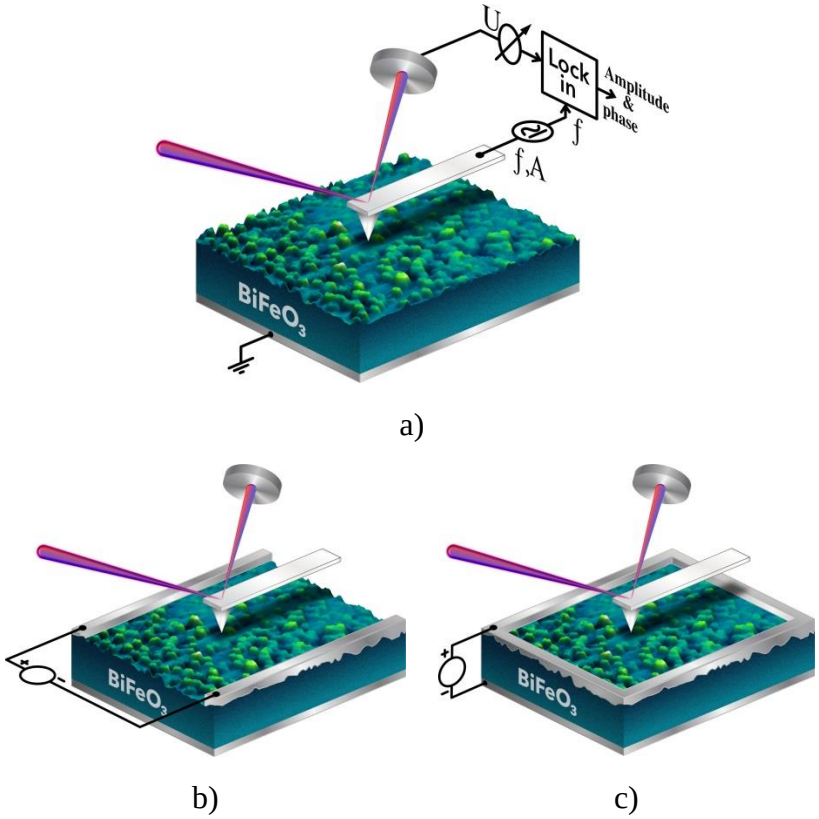

Figure 2.1. Measurement of electrical characteristics by AFM:
a) using metal conductive probe and b,c) using external contacts.

I used the set-up with optical system of cantilever deflection during. Bending of the cantilever is often detected by a laser beam reflected from the probe to a detector. Location of the incident beam on the detector is then looped back to move the probe up or down to preserve constant force between the probe and the sample, thus forming 3D image of the surface [50]. The scheme at figure 1 demands use of the tips with conductive or magnetic properties. Application of additional contacts (Fig.2.1. b, c) to the sample has some advantages as possibility to apply higher voltages (independent on microscope configuration) and different geometry of contacts to measure PFM at different planes. In this case there is no necessary to use conductive probe for PFM and even sub nanometer local bending of the sample will be detected. In this case there is also choice of scanning mode; both non-contact, tapping and contacted modes could be used.

The rest of scanning parameters should be well-adjusted, for example set-point and feed-back loop parameters or scanning rate. The last was mentioned by Ch.C. Glover et al.[51] Considering set-point and humidity conditions. This phenomenon is also described on calibration samples in Appendix 1.

3. FINDINGS AND DISCUSSION

3.1. $BiFeO_3$ on TiO_2 nanotubes surface

ALD synthesis has been performed to obtain perovskite/TiO_2 nanotube heterostructure. Perovskite nanolayers were grown on the surface of TiO_2 nanotubes. UV-visible (UV-vis) diffuse reflectance spectroscopy indicated that the absorption spectrum of the perovskite/TiO_2 composite extended into the visible-light region. The optical energy band gap for direct and indirect transition was determined for the perovskite/TiO_2 composite which is 2,31 and 2,67 eV, respectively. Main application potential of this structure is application in memristive devices. They have large polarization ability, as will be shown using PFM below. The design of structure is shown in figure 3.1. The work on these heterostructures is still in progress in collaboration with scientists from Dagestan State University (Orudzhev F.F., Ramazanov Sh.M., Isaev A.B., Alikhanov N.M.-R.), National Research Centre“Kurchatov Institute (Presniakov M.Yu), UNESCO-UNISA Africa Chair in Nanoscience's/Nanotechnology Laboratories and Nanosciences African network (K. Kaviyarasu).

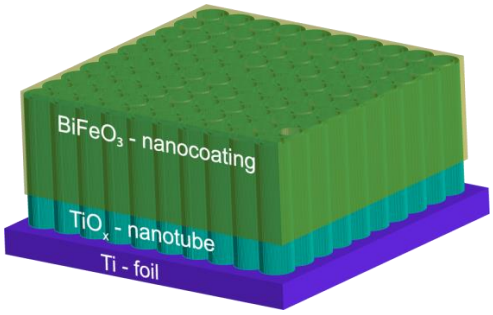

Figure 3.1. Suggested design of memristive structure.

Titanium dioxide nanoparticles are widely used as a heterogeneous photocatalyst for the photodegradation of pollutants in wastewater due to its high photocatalytic activity, low cost, non-toxicity and high stability in aqueous solution [52]. However, an important drawback of TiO_2 for photocatalysis is that its band-gap is rather large, 3.0–3.2 eV, and a small fraction of the solar spectrum is absorbed. Another problem of TiO_2 is high recombination photogenerated electron-hole pairs rate [53]. The vertically oriented TiO_2 nanotubes, synthesized on Ti plate by electrochemical anodization, currently have more attention compared with TiO_2 nanoparticles and nanowires. This is related to their oriented charge transfer channel, large surface area and the lower recombination rate of photogenerated electrons and holes [54]. Sensitizing TiO_2 nanotubes with other semiconductors is an efficient way to fabricate TiO_2-based catalysts with extended absorption in the visible and higher photocatalytic activity. The separation of photoinduced hole-electron pairs can be accelerated by the potential difference at the semiconductors heterojunction interface [55]. Recently it was discovered that a composite material based on TiO_2 and Bi_2O_3 is a good photocatalyst for use to photocatalytic water splitting. This catalyst has unique optoelectronic and catalytic properties, with a band gap of 2.8 eV, can oxidize water and generate highly reactive particles

to initiate re-oxidation reactions [56]. The Bi^{3+} including to the TiO_2 lattice facilitated the extended absorption in the visible part of spectra [57]. Most often, catalysts are obtained by liquid-phase methods, including impregnation, self-assembly, and hydrothermal synthesis [58]. However, in traditional methods, additional steps are necessary to remove excess metals or solvents and other reagents. To deposition other semiconductors into nanotubes, there are few methods, which have problems to precisely regulate the thickness of the shell material, size and composition, etc. In addition, the implementation and assembly of multifunctional active centers in a closed nanospace remains is one of difficult tasks of today. Therefore, to solve the problems of heterojunction interface preparation, advanced technologies are needed. The ALD is an excellent method for the preparation of heterojunction interface by direct deposition of highly dispersed particles (metals, oxides) into porous materials. Compared to conventional liquidphase methods, the ALD does not require the additional steps necessary to remove excess metals or solvents and side reagents. The experiment represent a loading of layered perovskites onto a TiO_2 electrode with a highly ordered vertically oriented nanotube array prepared by atomic layer deposition. The simple and green process makes this method a highly attractive one among all the existing methods for the preparation of TiO_2/perovskites nanocomposites.

3.1.1. Synthesis procedure

The TiO_2(Nt) heterolayers were grown in an ALDCERAM ML-200 (USA) atomic layer deposition reactor. As the substrate was used the TiO2(Nt)/Ti structures obtained as described in works [59]. Bi(mmp)3 (tris(1-methoxy-2methyl-2- propoxy) bismuth (Sigma-Aldrich American Elements, PN: BI-OMX-03M-C, 99.9%) and Ferrocene (Fe(cp)2, (Sigma-Aldrich F408) was taken as a source of bismuth and iron. In a typical experiment, the precursors were delivered to the ALD chamber with the assistance of N_2 carrier gas 99.999% purity. The Bi (mmp)3 evaporation temperature interval was 135-145 °C and the ferrocene precursor evaporate temperature was 91 °C. The $Bi(mmp)_3$ provides a higher growth rate than $Fe(C5H5)_2$ and the ratio between the times of NFe: NBi pulses action was 5:3. The ALD of BiOx consisted of a Bi (mmp)3 precursor pulse (1,2 s) - N2 purge (15 s) - ozone pulse (5 s) - N2 purge (15 s) (subcycle 90 cycles). Then FeOx ALD cycles was applied by 90 subcycles as well. The Fe(C5H5)2 precursor cycle pulse was 2 sec. The Inlet gas pipelines transporting precursors were at a temperature of 150 °C. The substrate was placed 4 cm from the inlet and the chamber was heated evenly to 250 ° C. The gas at the outlet was kept at a temperature of 150 ° C. Annealing of grown amorphous films was carried out in air at atmospheric pressure at the temperature of 660-680 ° C. The annealing time is 45-60 minutes.

3.1.2. Characterizations

Characterization of obtained atomic layer deposited perovskites was performed using SEM and TEM microscopy, UV-vis diffuse reflectance spectra. Raman spectra were examined by a Laser Raman 3D scanning confocal microscope (Ntegra Spectra, Russia) using a green laser (532 nm) with a spot size is 1 μm and a resolution of 0.5 cm-1. UV–vis diffuse reflectance

spectra were achieved using a UV–vis spectrophotometer Shimadzu UV3600. Both direct and indirect optical bandgaps were determined by using the Tauc relation [60].

The morphology of the as-anodized TiO_2 arrays (Fig. 3.2.a) is investigated using SEM measurements. Anodization of Ti plate resulted in the formation of a self-organized nanotubular structure. The average diameter of the TiO_2 nanotubes is around 60-80 nm and the tube length is ∼2 μm. Perovskite atomic layer deposited onto the TiO_2 nanotubes were investigated using transmission electron microscope. Figure 3.2b is a single nanotube TEM image, showing that many perovskite particles have been deposited onto the surface of the TiO_2 nanotube. Especially from Figure 3.3.b, the interface between the TiO_2 wall and perovskite coating is well distinguishable. There are actually two interfaces between the TiO_2 wall and perovskite coating, as the perovskite coating is deposited inside (interior coating) and outside (exterior coating) the TiO_2 tube walls.

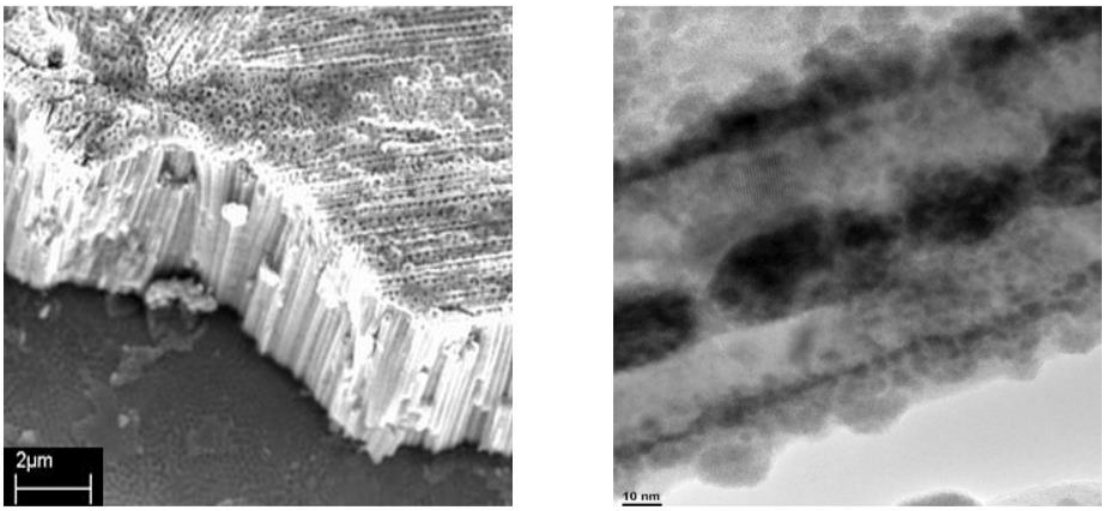

a) b)

Figure 3.2 (a) SEM image of Ti/TiO_2 nanotubes; (b) TEM image single perovskite deposited TiO_2 nanotube.

The complex layered structure of the material is formed. Qualitative distribution of the elements is shown by Energy-dispersive X-ray spectroscopy (EDX) (Fig.3.3).

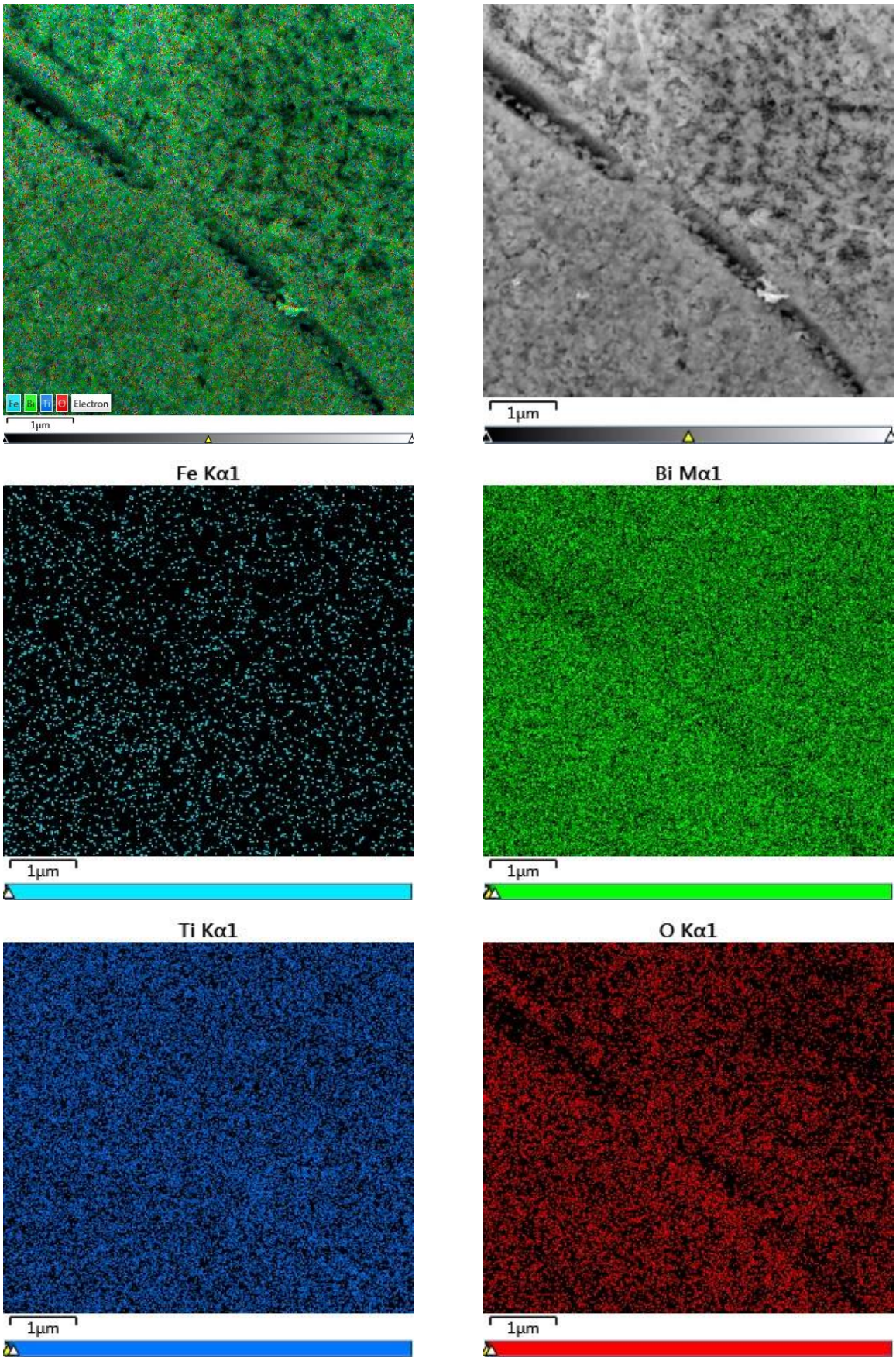

Figure 3.3. EDX spectra of the BFO/TiO_2, showing homogeneous distribution of elements.

The crystal lattice of all phases is constructed out of perovskite-like layers $(A_{m-1}B_mO_{3m+1})^{2-}$, which alternate with bismuth-oxygen layers $Bi_2O_{22}^{+}$ having the structure of the phase with the number of perovskite-like layers in the package n = 4. In the synthesis of bismuth titanates with other compounds $Bi_4Ti_3O_{12}$ (n = 3) is often present as an additional phase. Formation of compounds has already been studied at the phase boundary between Bi_2O_3 and TiO_2 in the composition of the TiO_2 – Bi_2O_3 – TiO_2 sandwich [61]. As a result of this study, it was concluded that, in the first place, a stable compound $Bi_4Ti_3O_{12}$ is formed in the place of the Bi_2O_3 layer. From Figure 3.2 staggered stacking defects are observed along with the thickness of the unit cell. However, the perovskite structure is preserved in the future, and the defects, apparently, influence the occupation of the regions in the crystal, and not their general layout. Ions in a narrow range of 0.58– 0.65 can replace Ti^{4+} in an octahedral cell. So the ionic radius of Fe^{3+} is slightly larger than Ti^{4+} (6%). This will displace these ions relative to the $(Bi_2O_2)^{2+}$ layer. In addition, these step defects can be attributed to the steps in the substrate, as well as to the presence of surface groups of TiO^2 nanotubes.

These data are confirmed by the results of Raman scattering presented in the Figure 3.4. As can be seen from Figure 3.4, for the structure, characteristic modes appear, corresponding to TiO_2 in the anatase and rutile phases [62]. The peaks at 567, 844 cm^{-1}, which are characteristic of layered perovskites, also clearly manifest themselves. These are peaks of stretching vibrations. According to previous studies on perovskite oxides [63], [64], they are due to the stretching of the TiO6 octahedron and exhibit A1 character.

The diffuse reflectance UV-vis spectra of the perovskite/TiO_2 nanotube heterostructure samples, expressed in terms of Kubelka-Munk equivalent absorption units, are presented in Figure 3.5. The absorption spectra of the perovskite/TiO_2 nanotube show a stronger absorption in the visible light region and a red shift in the adsorption edge.

Tauc Mott plot is used to calculate the bandgap of these materials. The Tauc formula depicting the relationship between absorption coefficient and incident photon is as follows (1):

$$\alpha h\gamma = A\,(h\gamma - Eg)^n \qquad (1)$$

Where, α is absorption coefficient, A is constant and n can be 2 (direct transition) or 0,5 (indirect transition) [60].

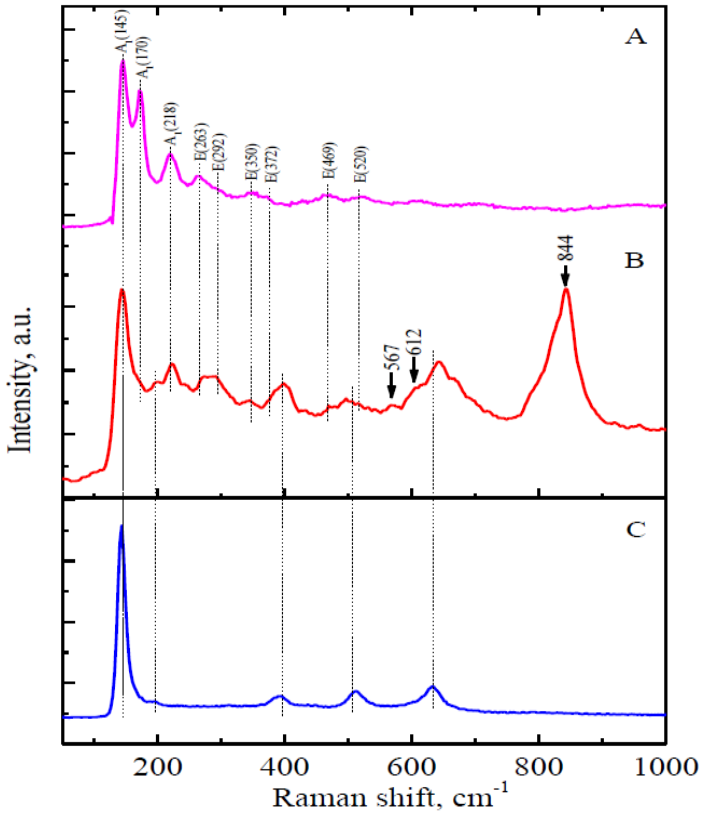

Figure 3.4. Raman shift spectra of ALD synthesis perovskite/TiO_2 nanotube composite.

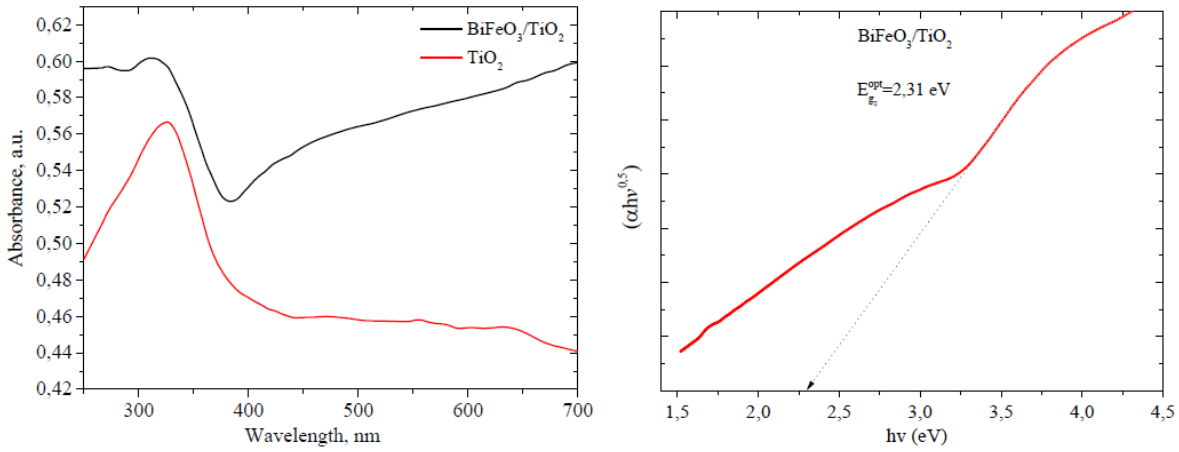

Figure 3.5. UV-vis (a) and Tauc Plot (b) of ALD synthesis perovskite/TiO_2 nanotube composite.

The optical energy band gap for direct E_{g1}^{opt} and indirect E_{g2}^{opt} transition was determined by plotting $(\alpha h\nu)^{1/2}$ and $(\alpha h\nu)^2$ as a function of photon energy ($h\nu$). The respective values of E_g^{opt} are obtained by extrapolating to $(\alpha h\nu)^{1/2} = 0$ for indirect transition and $(\alpha h\nu)^2 = 0$ for direct

transition. The value of direct and indirect band gap for the 3D NG is 2,31 and 2,67 eV, respectively.

The localization of electronic states density is determined by the physical characteristics of material, such as optical absorption, conductivity and photoconductivity. The density of electronic states localization in synthesized 3D NG can be determined from the Urbach energy value calculated from the rate of exponential decay of the "tail" on the absorption spectrum presented in semi logarithmic coordinates. The calculated Urbach energy values is 0,36 and 0,22 for TiO_2 NT and 3D NG respectively. The decrease of Urbach energy values of the perovskite/TiO_2 composite indicates a decrease in the density of localized electronic states and, as a consequence, of a lower electrical conductivity.

Microscale and macroscale electric properties are shown in figures 3.6 and 3.7. PFM shows obvious polarization of the sample at +5V that was still present in reverse voltage.

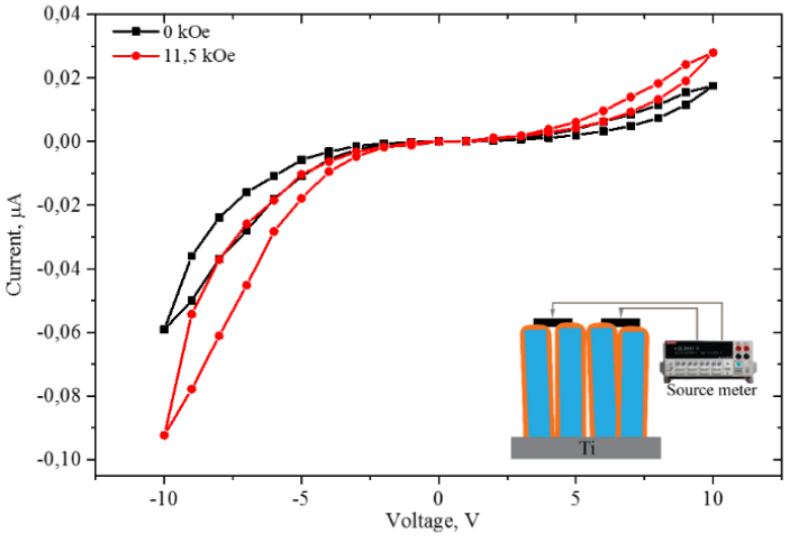

Figure 3.6. Current-voltage characteristics of $BiFeO_3/TiO_2$(Nt)/Ti structure.

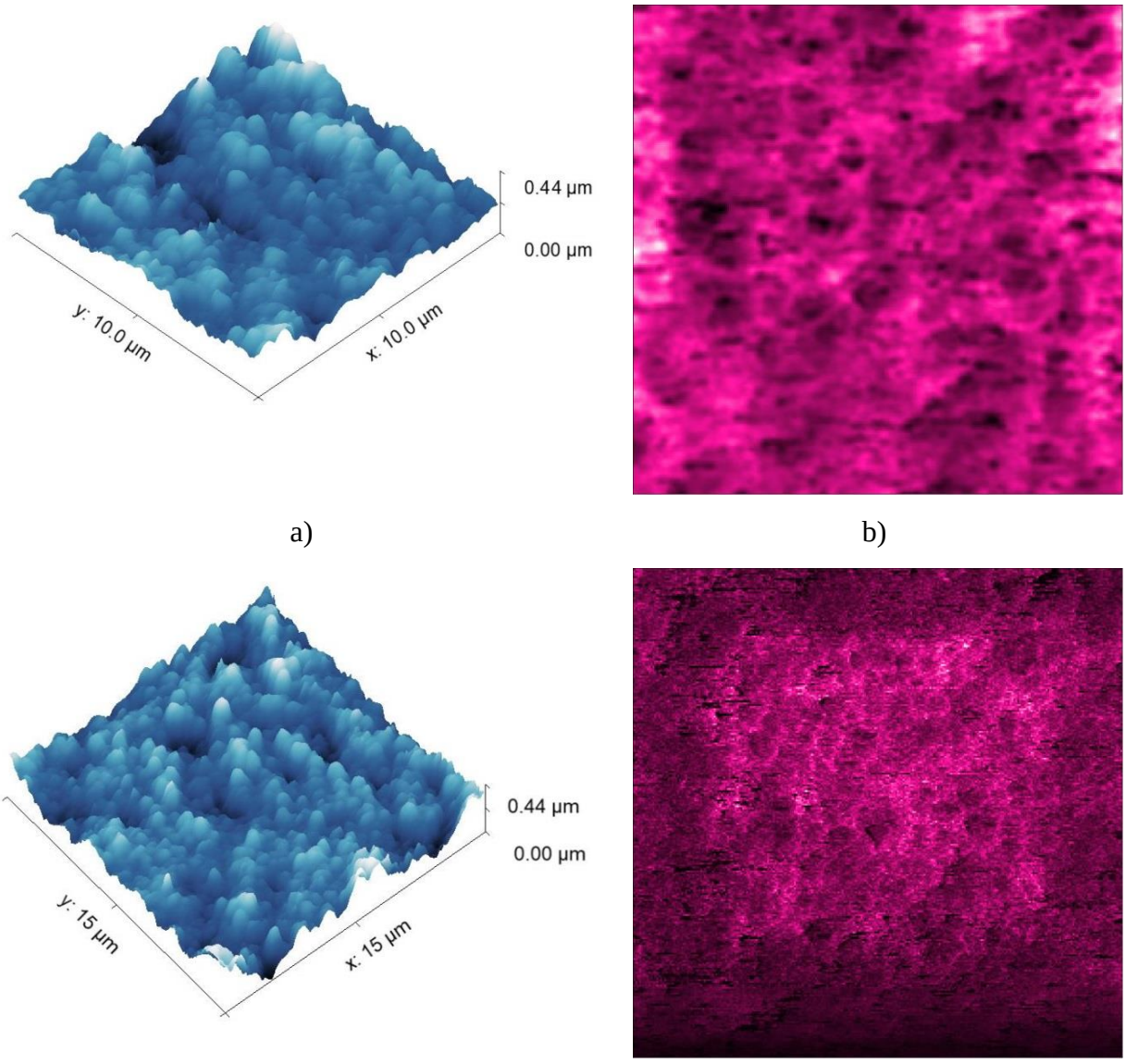

Figure 3.7. PFM of the sample: a,c) topography and b,d) amplitude piezoresponse signal;
a,b) scanning with bias voltage +5V, area 10x10 µm,
c,d) scanning with bias voltage -5V, area 15x15 µm.

In summary, a composite of perovskite/TiO_2 heterostructured nanotubes was synthesized via an ALD method. SEM and TEM observation revealed that the as-synthesized sample is nano-sized self-organized nanotubular structure hierarchy configuration consisted of $BiFeO_3$, $Bi_4Ti_3O_{12}$ layers decorated with the primary TiO_2 submicron nanotubes. Extension of the light absorption from the ultraviolet region to the visible-light region was confirmed by UV-vis absorption spectra.

3.2. Bi-Fe-O composition on highly oriented pyrolytic graphite

Here the ultrathin films of Bi-Fe-O composition prepared by atomic layer deposition on highly oriented pyrolytic graphite (HOPG) substrates is described. The films thickness is ~ 40 nm from one technological cycle of BiO_x and FeO_x layers deposition. Qualitative and quantitative analysis shows good mixing of the components with partial formation of the bismuth ferrite phase at a growth temperature of 523 K. Due to the presence of weak Van der Waals bonds between the layers during the oxidation process, swelling and delamination of the near-surface on highly oriented pyrolytic graphite layers occurs. According to the X-ray photoelectron spectroscopy, blisters and flake structures with graphene layers on the underside of the $BiFeO_3$ film are created as a result of redox reactions on the surface. The proposed method allows obtaining of the bismuth ferrite/graphene structure with no peeling of highly oriented pyrolytic graphite required.

As was mentioned above, various phase compositions of Bi-Fe-O system is of interest because of its electric,[65] magnetic,[66] piezo,[67], [68] ferroelectric,[69] dielectric,[70] memristive[71], [72] and optical[73]–[76] properties and capable of large energy density accumulation (roughly ~ 70 $J \cdot cm^{-3}$).[77] It makes BFO/Graphene important for application as electrode material for supercapacitors. Other potential use of these structures is proposed by Zhenhua Qiao, et al.,[78] where authors presented a calculation system for graphene adsorbed on the (111) BFO surface. Hyun Wook Shin and Jong Yeog Son[79] presented the Graphene/BFO/HOPG capacitor structure obtained by pulsed laser deposition and showed multiferroic properties, namely, ferroelectricity and ferromagnetism. The substrate temperature in this case was ~ 1073 K, at which it was more likely that additional phases would precipitate alongside the polycrystalline BFO phase.[80] Besides, it is still impossible to use it as a supercapacitor. Successful realization of this structure will lead to huge technological leap.

HOPG itself is an important and promising material for future electronics, and the source of graphene materials. To improve the quality of solid-state energy storage devices, carbon-based materials are used as electrodes. In addition, the use of graphene significantly increases their efficiency[81] and makes it possible to use them in flexible electronics.[82] Because of this there is great interest in the search and development of new efficient and more active electrocatalytic materials. It was shown by Sharel E. et al.[83] that modification of the (HOPG) surface by producing surface bubbles leads to the formation of electrode material with significantly increased electrochemical activity.

HOPG variant of carbon is produced through pyrolysis of carbon-containing steam at high temperatures of about 2300 K and subsequent annealing at a temperature of about 3275 K. The resulting material forms an almost pure sp^2 hybridized hexagonal structure with very strong bonds in the graphene plane and weak bonds between the planes, which allows relatively easy separation. Pressed HOPG of high quality, regularity and smoothness at the nanoscale is divided into varieties,[84] some of them are the ZYA brand has a mosaic distribution of 0.8° ± 0.2° and the grain size is up to 10 μm, the ZYB brand has a mosaic distribution of 1.2° ± 0.2° and the grain size is up to 1 μm, and the ZYH brand has a mosaic

distribution of 3.5° ± 1.5° and a grain size of 30–40 nm. In this work, ZYB HOPGs of 7 × 7 mm dimensions (purchased from NT-MDT) were used.

3.2.1. Synthesis procedure

It is well known that the nucleation of ALD films of metal oxides on chemically inert sp^2 carbon surfaces is a very difficult task. It was shown that on untreated sp^2 carbon surfaces, the nucleation of films can be observed only at lattice defects or the edges of steps [85]–[89]. In this work, HOPG substrates were pretreated with argon ions (Ar^+). To clean and functionalize the surface of the sample and for a more detailed understanding of the boundary reactions between the film and the substrate, the surface was partially subjected to electron bombardment in a vacuum of 10^{-8} torr and annealed at temperatures up to 1173 K for 20 minutes. After annealing, the sample was subjected to Ar^+ ion bombardment for three cycles, each lasting 5 minutes. A difference in the miscibility of the components on the treated and untreated surface of the substrate is explored as well.

To obtain a layer of amorphous bismuth ferrite on the HOPG surface by the ALD method, the ALDCERAM® ML-200 set-up was used. Tris(1-methoxy-2-methyl-2-propoxy)bismuth ($Bi(mmp)_3$) (Sigma-Aldrich) was used as the Bi containing organometallic precursor. The evaporation temperature was in the range of 408-418K. Ferrocene $Fe(C_5H_5)_2$ (Sigma-Aldrich) was used as the Fe containing precursor. The optimal evaporation temperature of ferrocene was 364 K. For oxidation, O_3 was introduced into the chamber through an ozonizer. The purge was carried out using carrier gaseous N_2, with a purity of 99.999%. The substrate was placed at a distance of 4 cm from the inlet. The chamber heated up evenly T = 523 K. The preliminary vacuum in the chamber was 10^{-3} torr. The purge gases at the outlet were held at a constant temperature of 423 K. The process was carried out in 150 sub cycles with each precursor in one technological mode. Figure 3.8 shows the sequence of the ALD process, where the duration of the t_{Bi} sub cycle is 15.2 sec and the t_{Fe} sub cycle is 16 sec. At the beginning, the BiO_x layer and then the FeO_x layer were obtained. The thickness of the Bi-Fe-O film was about 40 nm. A simple method for producing graphene from HOPG by oxidation with ozone and at low temperature (530 K) was reported by M. J. Webb, et al. [90].

The result is a modification of graphite near-surface layer, containing graphene and a small amount of oxygen and hydrogen. The mechanism occurs in our case during obtaining of BiO_x layer at the initial stage of growth.

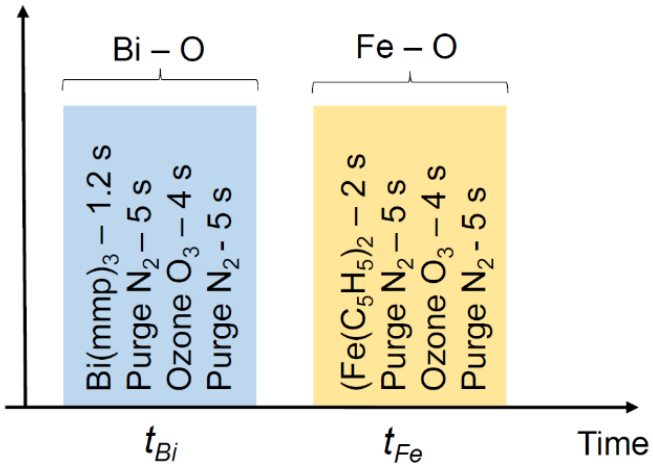

Figure 3.8. Sequence of ALD process including sub-cycles for bismuth and iron.

The pretreated HOPG substrates and the resulting Bi-Fe-O/HOPG structure were studied using scanning electron microscopy and Raman spectroscopy. The surface of the samples was studied by the atomic force microscopy. Using the Time-of-flight secondary ion mass spectrometry (TOF-SIMS), a qualitative analysis of the processed Ar^+ and untreated sections of the samples in depth was carried out, as well as a distribution of Bi, Fe, C elements on the surface was performed. Then, the X-ray photoelectron spectroscopy (XPS) method was used to study the binding energy of the constituent components with the possibility of in-situ heating to a temperature of 923 K.

3.2.2. Characterizations

Acquisition of SEM images of treated HOPG surfaces was performed using scanning electron microscope Magellan (Thermo Fisher). Figure 3.9 shows the relative darkening of the treated (Ar^+) region. Raman spectroscopy was performed using an Invia spectrometer (Renishaw) with green laser (DPSS 532 nm, P = 30 mW). Raman spectra of the substrate treated, and untreated locations are shown in figure 3.9b.

As can be seen from figure 3.9b, HOPG surface after the treatment with argon ions is partially destroyed and peak D appears at 1358 cm^{-1}, which is associated with the formation of defects, surface amorphization, and disruption of lattice symmetry [91]. It indicates the disruption of sp^2 carbon bonds and a possible formation of oxide on the treated surfaces. According to T. Shimada, et al., [92] 1754cm^{-1} peak refers to the overtone of the out-of-plane transversal optical phonon. One more overtone band can be found at 2442 cm^{-1} and assigned to 2LO phonon [93]. Both treated and untreated spectra contain G and 2D peaks (1581 cm^{-1} and 2728 cm^{-1}, respectively) responsible for the HOPG structure. The G-band peak is due to the Raman active E_{2g} mode and is characteristic of carbon forms with sp^2 hybridization.

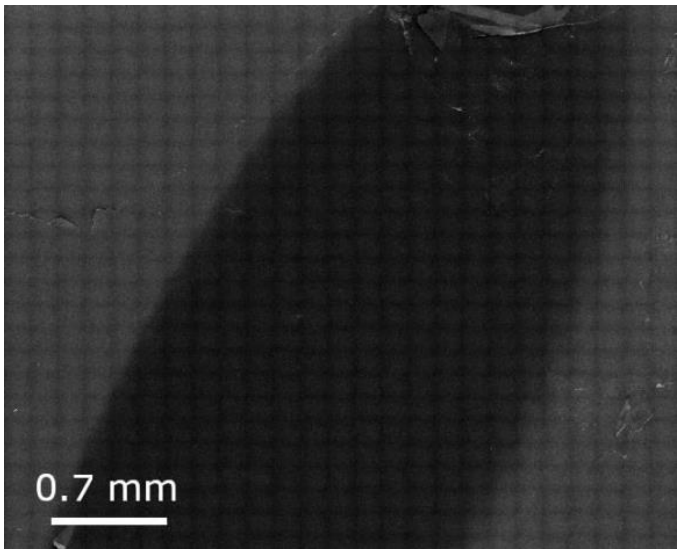

a)

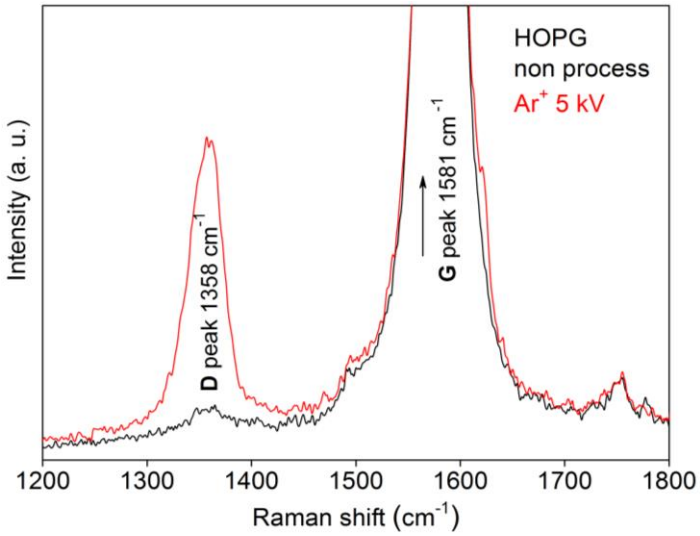

b)

Figure 3.9. (a) SEM image of HOPG surface, dark region is the treated area; (b) Raman spectroscopy of the treated and untreated HOPG surface areas:
black line - before processing by Ar^+, red - after processing by Ar^+.

Asymmetry of the 2D peak according to literature depends on the number of layers of graphene. In our case, the form corresponds with HOPG [94]. The relative intensity of the 2D peak is higher for treated graphite. It is also related to the formation of defects resulting from bombardment. The resulting Bi-Fe-O films were inspected using SEM Verios (ThermoFisher), AFM (ICON Bruker) and Raman spectroscopy. Morphology of the obtained samples is shown in figure 3.10 and figure 3.11.

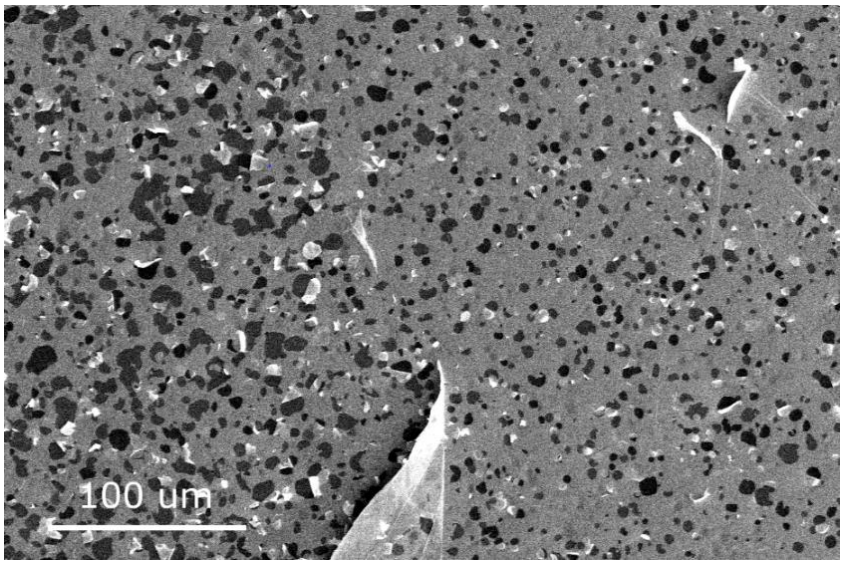

Figure 3.10. SEM image of the surface of the Bi-Fe-O/HOPG structure, right side from the center is the film on the treated surface of the substrate, on the left the film is on untreated.

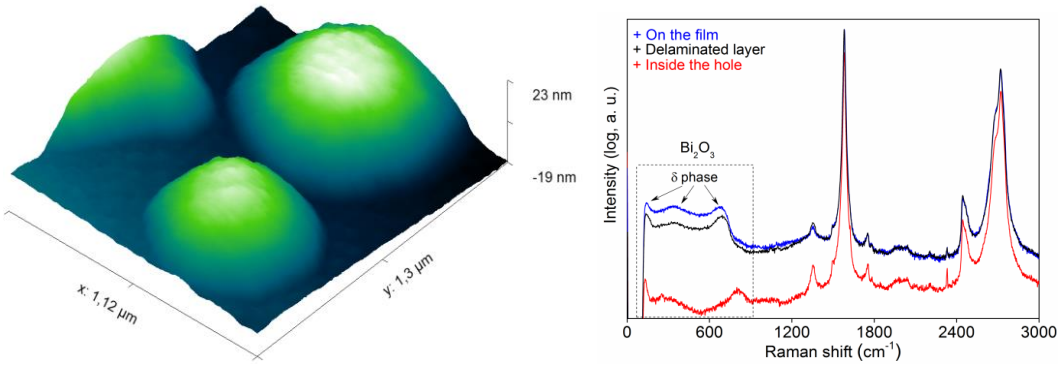

a) b)

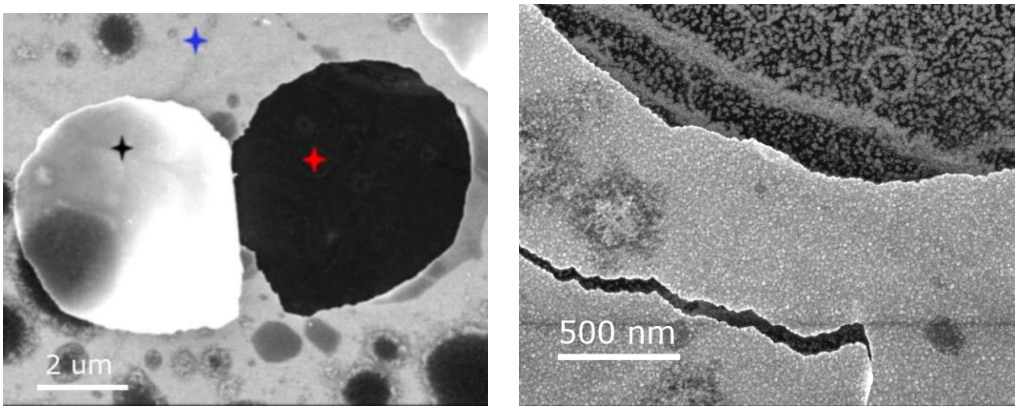

c) d)

Figure 3.11. a) AFM image of the surface of the Bi-Fe-O/HOPG sample; b) Raman spectroscopy of the surface areas marked in SEM image (c) (the color of the line corresponds to the color of the selected areas); c, d) SEM patterns of a single open bubble (flakes) and an enlarged image of film-substrate interface.

Surface differs in the number of open bubbles (flakes) of the treated and untreated sections of HOPG, as can be seen in figure 3.11. Due to dangling carbon bonds on the treated surface, intermediate compounds between bismuth ferrite and the carbon layer are formed more actively and, accordingly, the number of bursting bubbles is greater. Delamination depends on several factors, including sample size, substrate quality, film unevenness, degree of adhesion, crystal lattice parameters of the substrate and the thin film, and the difference in temperature coefficients. Presented steps, dislocations and grain boundaries on the surface of HOPG could induce the bulking [95].

AFM of a film surface prior to SEM analysis was carried out and is shown in figure 3.11a. In the process of oxidation of the HOPG surface, the upper graphene layers rise, the number of organized layers is approximately 1-5 [96]. Upon further growth and under the influence of technological factors, they burst into the flakes state [97]. Figure 3.11c shows a single bursting bubble. Raman spectra were analyzed in the same area and presented in figure 3.11b. These bubbles open likely due to the influence of additional vacuum pulling during the study and the introduced energy of electron beam and the resulting morphology is shown in figures 3.11c and 3.11d.

A more intense delamination on the treated side of graphite is a consequence of the presence of defects in the substrate, as can be seen using Raman spectra in figure 3.11. The peaks at the beginning of the spectrum correspond with the nanocrystalline phase of Bi_2O_3. Liu Liwei et al. [98] note that δ-Bi_2O_3 can exist at temperatures below 473 K and undergo a sequence of phase transitions $\delta \rightarrow \beta \rightarrow \alpha$ with increasing annealing temperature above 473 K. In this case, the bismuth oxide phase is already formed during the growth process, and the iron oxide phase is still in the amorphous state.

The occurrence of displacements in the film-substrate interface in the presence of bismuth atoms was observed by Xueyong Pang et al.[99]. Presence of a larger bismuth atom leads to deformation of the surface layers lattices. In addition, unpaired $6s^2$ electrons of bismuth Bi^{3+} contribute to its integration into a defective medium. Due to the presence of weak Van der Waals bonds between the layers, swelling and delamination of the surface layers occurs [100]–[102]. Delamination also confirms the fact that the observed spherical elements of the surface topography (figure 3.11 a) are hollow and do not represent compounds of a different composition, except for the possibility of forming a gas phase from adjacent compounds (CO, CO_2, etc.).

During film deposition, ozone is introduced into the chamber; it oxidizes the surface of HOPG and forms nanobubbles. As was also noted in Appendix 2, the oxidation of HOPG with HNO_3 also clearly forms bubbles over the entire surface. Further SEM-image (figure 3.10b) shows that the exfoliated layer is relatively transparent to electrons. The Raman spectra of the lower part of the flakes and the film surface almost coincide with the peaks in the region of 50-700 cm^{-1}. Due to carbon composition of the substrate, it is difficult to apply Raman spectroscopy for evaluation of number of delaminated layers. Transparency of the film during SEM imaging assumes up to 5 graphene layers of delaminated blisters.

Depth profiling was performed by SIMS and using Bi^+ 30 kV analysis beam of 200 μm^2 area used in imaging mode, and O_2^+ 500 V for sputtering. The O_2^+ beam have also an enhance

effect on signals intensity. The analyses were carried out at TOF-SIMS[5] set up (IONTOF). The argon-processed area of HOPG has a deeper penetration of Bi^+ and Fe^+ ions inside the near-surface area. Figure 3.12 shows SIMS images of the components Fe^+, Bi^+, C^+ and their RGB composite image.

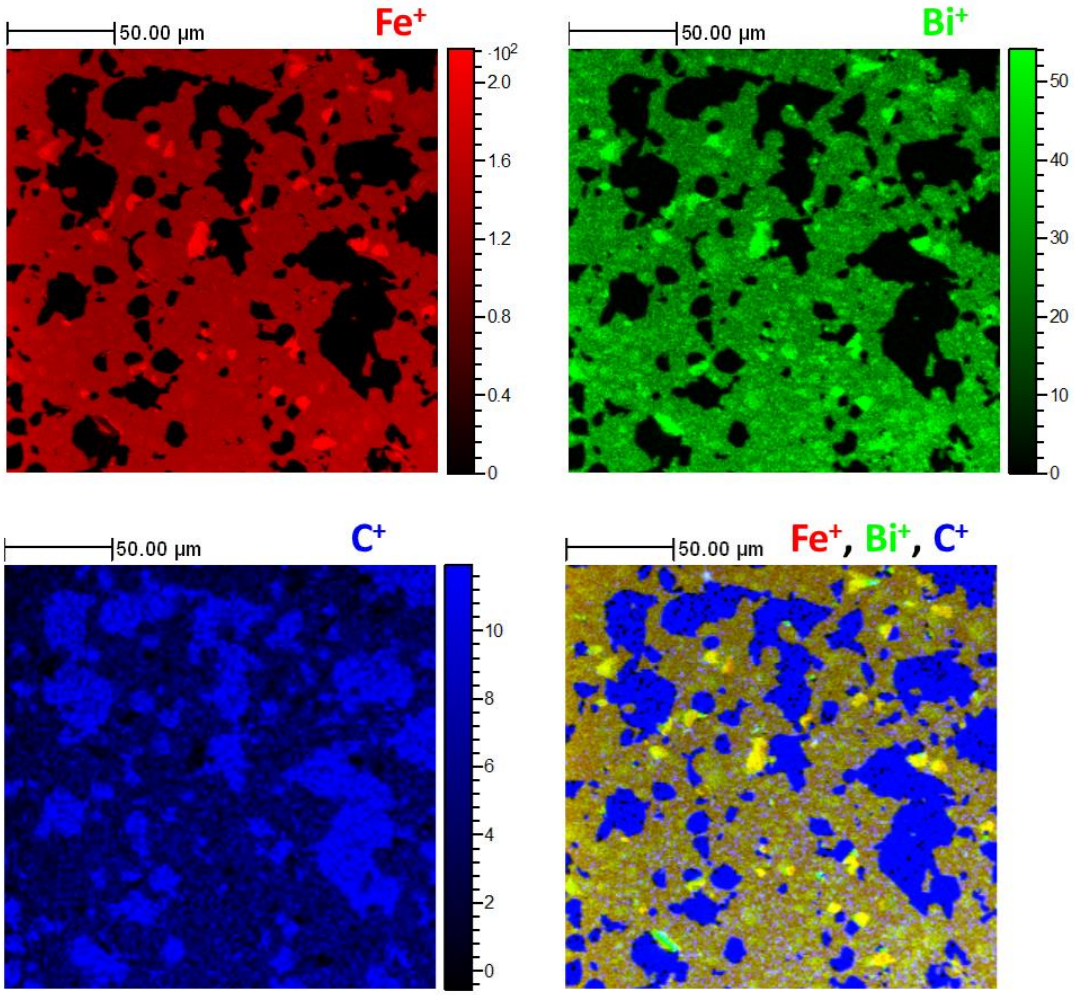

Figure 3.12. SIMS of the sample surface: composition of the components Fe, Bi, C and their combined image. The combined image demonstrates presence of Bi-Fe-O phase obtained in the process of the film deposition.

Yellow sections in picture with all the compounds of figure 3.12 indicate partially formed bismuth ferrite at 523 K. Green sections indicate the amount of bismuth in the near-surface region.

Figure 3.13 and figure 3.14 show the measured profiles for elements and compounds obtained using the TOF-SIMS system for the Ar^+ treated and untreated HOPG section, where the analyzing Bi beam was set at 30 keV, 200 × 200 μm^2, 128 × 128 px^2, and etching O_2^+ beam at 1 keV, 340 × 340 μm^2. The measurement was done in spectroscopy mode with mass resolution m/Δm 6000. The appearance of elongated inclusions at the bottom of three-dimensional images is associated with the presence of islands on the surface. This effect is

caused by uniform etching of the surface. Therefore, the surface in the images is flat, even though the etching starts directly from the surface, which, according to the AFM, is not smooth. The depth of the analyzed area in figure 3.13 and figure 3.14 is approximately 70 nm. SIMS gives us the opportunity to qualitative observation of Bi, Fe, C and BiO_x and FeO_x fragments.

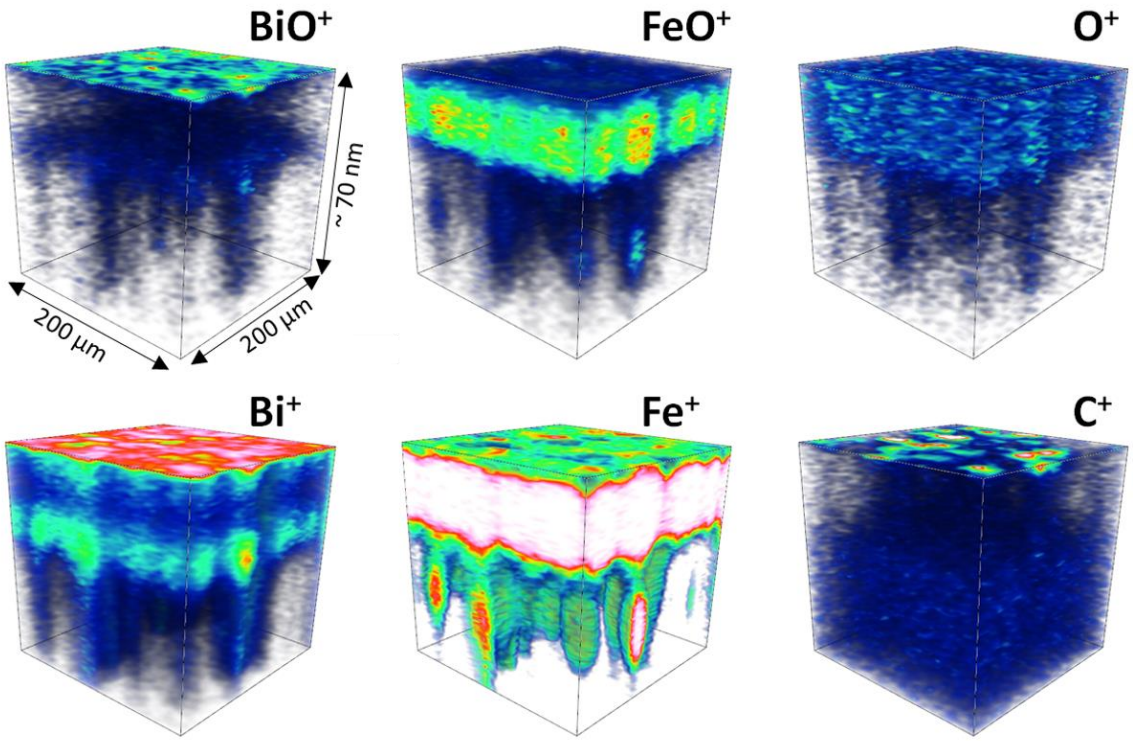

Figure 3.13. SIMS 3D Rendering image of HOPG surface without Ar^+ treatment. Presented cube area is 200 × 200 μm^2 square and 70 nm depth.

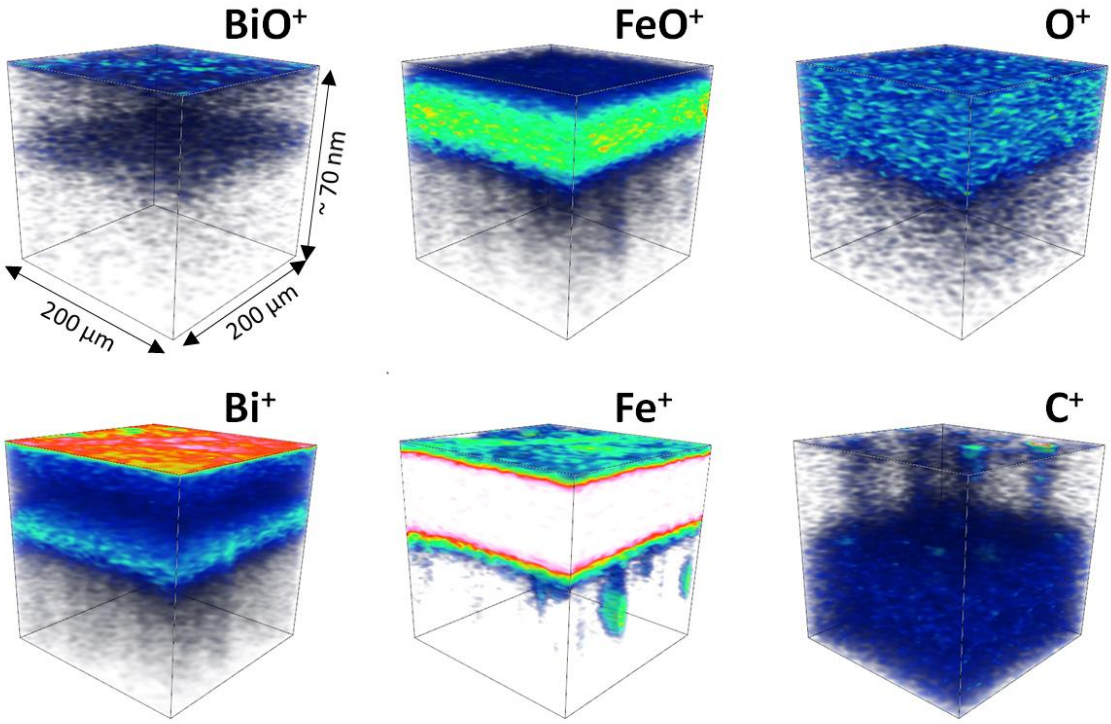

Figure 3.14. SIMS 3D Rendering image of HOPG surface after Ar^+ treatment. Presented cube area is 200 × 200 μm^2 square and 70 nm depth.

The TOF-SIMS analysis confirms good miscibility of the elements of bismuth ferrite composition. Considering the elements and their oxides, it can be seen that bismuth has higher concentration on the surface than iron. This confirms the greater solubility of bismuth. Analyzing Fe^+ and FeO^+, it is possible to conclude that iron is completely oxidized, probably in the amorphous phase. Analysis of O^+ ions shows a greater and more uniform depth of oxygen penetration between graphite layers. Distribution of C^+ component shows that amount of carbon is lower on the treated area. All this indicates a more conformal and high-quality formation of the Bi-Fe-O composition on the surface of the ion-treated HOPG region.

To understand the reactions occurring between the components of the film and the substrate, the samples were studied by XPS with the possibility of in-situ heating. Annealing lasted for 5 min for every used temperature. The study was conducted using the tool AXIS SupraTM (Kratos), vacuum during the measurement was about $2 \cdot 10^{-8}$ torr. The sensitivity of this method is up to 5 nm. XPS spectra were taken several times from both processed and unprocessed areas of the samples. Only a slight difference of components proportion was observed. It can be caused by a non-homogeneous distribution of bulking and delaminated areas. The type of chemical bonding according to peak shapes is the same over the whole surface. The size of the investigated region was 300 × 700 µm. After calibrating the spectra at the C1s position corresponding to C–C bond (284.8 eV), the positions of the high-resolution Fe, Bi, and O peaks were evaluated. Detailed information about peaks was obtained by subtraction of Shirley background using CasaXPS software. Normalized spectra are given in figures 3.15 c-d for a comparative analysis at different annealing temperatures. XPS spectra of

Fe has $2p^{3/2}$ and $2p^{1/2}$ peaks, which can be fitted as two peaks for Fe^{2+} and Fe^{3+} (Figure 3.15a). Bi^{3+} oxidation state is observed at peaks $4f^{7/2}$ and $4f^{5/2}$ located at 159.2 eV and 164.5 eV (Figure 3.15b). According to the literature,[103], [104] the largest peak of oxygen near 529 eV could be assigned to oxygen in BFO structure and the oxygen peak at 530.1 eV corresponds with dangling bonds of oxygen (Figure 3.16c). Peaks at the binding energies of 710 eV and 724 eV represent a doublet of Fe $2p_{3/2}$ and Fe $2p_{1/2}$, which becomes more prominent as a result of the spin-orbit interaction. In this case, the energy of spin-orbit splitting of the doublet is ~ 13.7 eV, in contrast with the theoretical value (ΔFe2p) of 13.6 eV for Fe_2O_3.[104] In addition, the peaks of Fe $2p_{1/2}$ and Fe $2p_{3/2}$ at high temperatures are shifted by 0.9 eV and 0.5 eV, respectively. The redshift suggests a certain electronic interaction between BFO and RGO sheet[105] due to difference in the electronic configuration of Fe^{2+} (d_6) and Fe^{3+} (d_5) ions. Satellite peaks are very often used to determine the chemical state of iron. As can be seen from figure 3.15, all satellite peaks appear at 8-8.5 eV higher binding energy than corresponding main peaks in the experimental spectra of Fe2p. This result convincingly indicates the existence of only the Fe^{3+} state for all samples, since the satellite peaks arise at a binding energy of 6 eV higher than the corresponding main peak for the Fe^{2+} state [106].

The narrow-band spectra of Bi4f level, characterized by the presence of a doublet peak consisting of $Bi4f_{7/2}$ (158.2 eV) and $Bi4f_{5/2}$ (163.5 eV) are presented in figure 3.15b. Although a shift in the position of the peaks towards higher binding energies (159.2 eV and 164.5 eV, respectively) is observed with increasing temperature, the energy of the spin-orbit splitting of the Bi4f doublet remains unchanged (5.3 eV), which is in good agreement with theoretically calculated values (5.31 eV) [104]. The positions of the Bi4f peaks confirm the presence of the Bi^{3+} state in the sample and are identified as a signal from Bi-O bonds,[105], [107] which is manifested on XPS at annealing temperature of 773 K. During further annealing, a shoulder appears to the right of the $4f_{5/2}$ and $4f_{7/2}$ peaks in the high-energy region. This is probably due to the formation of Bi^{5+} and its corresponding peaks $4f_{5/2}$ and $4f_{7/2}$. As was already mentioned in literature [107], the results indicate the formation of “final” and “bridging” superoxide particles, which are trapped in the vacant oxygen centers of Bi_2O_3. Bi(IV) and Bi(V) centers are also formed, where O_2^- interacts with Bi(IV) centers yielding two superoxide adducts with temperature-dependent relative amounts of Bi(IV)-O_2^- and Bi(IV)-O_2^--Bi(III). In this regard, the wide peak in the region of 532.2 eV in the O1s spectrum (figure 3.15c), which is detected at annealing temperature of 673 K, can be attributed to superoxide bonds in the BFO film. XPS of bismuth bonds also demonstrate a small change in the binding energy with increasing annealing temperature, followed by a decrease and the appearance of a peak in the region of 153.4 eV, which can be attributed to the plasmon peak associated with charging effects [108].

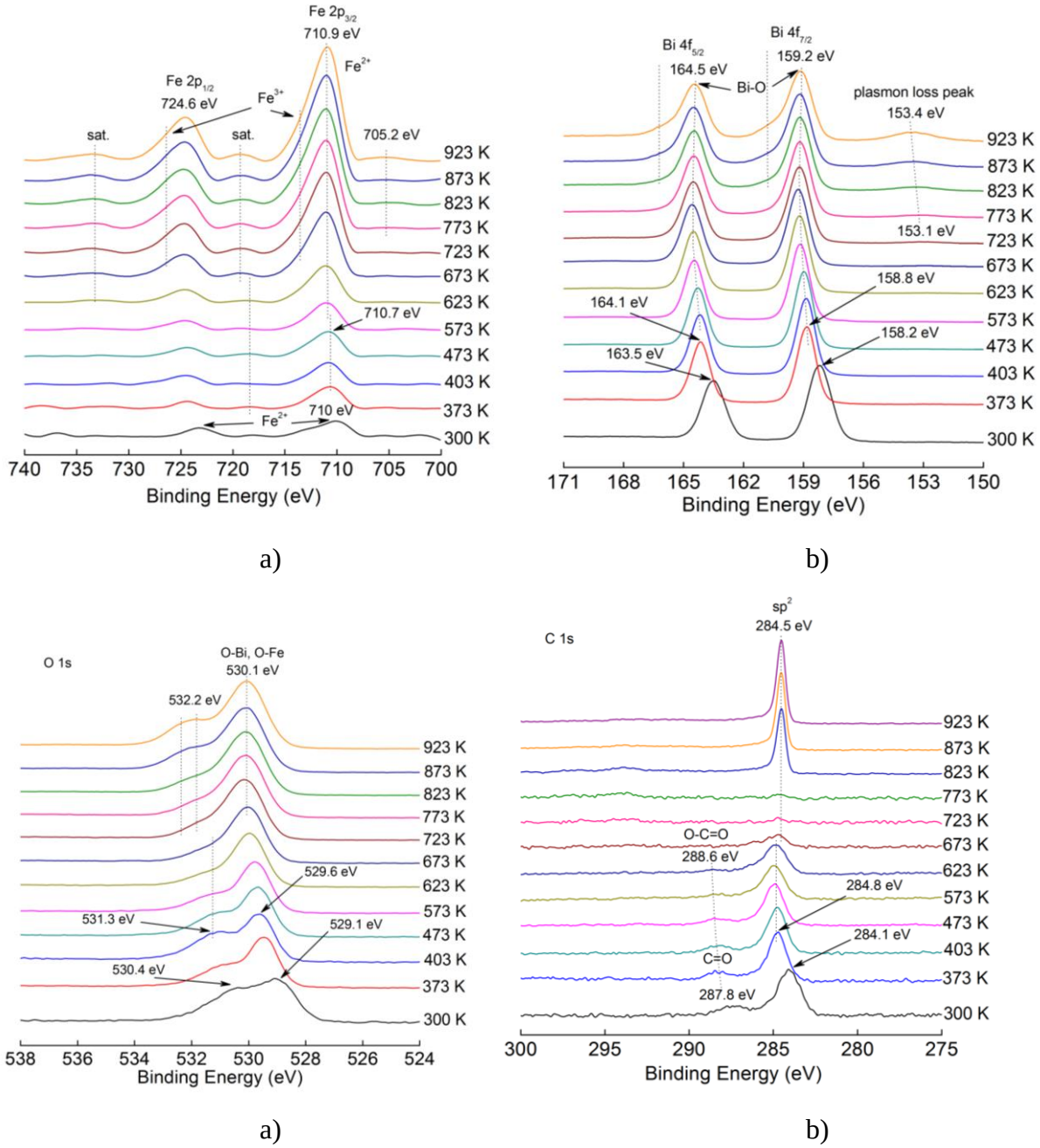

Figure 3.15. XPS BFO/HOPG structure: (a) high-resolution Fe 2p spectra; (b) high-resolution Bi 4f spectra; (c) high-resolution O 1s spectra; (d) high-resolution C 1s spectra.

Two regions are clearly observed in the narrow-band spectrum of C1s. They are characterized by a small chemical shift depending on temperature at binding energies of about 284 eV and 288 eV, respectively [109]. The broad peak with a binding energy of about 284.5 eV can be attributed to the non-oxygen sp^2 carbon C=C, which represents the structure of HOPG graphene layers [110]. The presence of a wide shoulder in the region of 285 eV indicates the bonding of carbon atoms with oxygen in hydroxyl (C–OH) or epoxy (C–O) functional groups located in the basal plane of graphene sheets, responsible for the presence of defects in the plane [111]. A peak in the region of about 288 eV characterizes bonds of carbon atoms in

carbonyl groups (>C=O), corresponding with COOH functional groups, usually located at the edges of graphene sheets [112]. After 823 K, only one region remains in the spectrum characterizing the non-oxygen sp2 carbon bond C=C, which indicates the deoxygenation of the delaminated surface of graphene-like HOPG layers [113].

Figure 3.15d shows the peak associated with the formation of C=O (at annealing temperatures up to 623 K), as well as its transitions to O–C=O in the region of 288.8-288.6 eV with increasing annealing temperature. It was also observed during the formation of a thin layer of iron with self-organization of the Fe_2O_3 phase on the HOPG surface [114]. This is likely due to the catalytic properties of iron oxide itself [115]. The sp^2 intensity becomes almost invisible in the spectrum during annealing at 723-773 K. This is due to the formation of a BFO film in the crystalline phase and the initial stage of carbon reduction in the near-surface region. At an annealing temperature greater than 823 K, a graphene layer with cohesion energy of 284.5 eV is formed on the lower surface of the already formed BFO film.

Peaks for Fe-O and Bi-O bonds are around 530.1 eV and 531.8 eV respectively for all temperatures [116], [117]. Bi_2O_3 exists in several polymorphic modifications, and also as a material with oxygen vacancies $Bi_2O_{2.33}$ [118]. The peak near 531.3 eV grows up to 403 K, then decreases and disappears, which indicates the formation of oxygen vacancies [119] and their growth with the release of CO_2 [120]. The BFO phase starts forming at 723 K. The solid-state reaction that occurs at the interface region of Bi_2O_3 and HOPG can be written by equation 2:

$$Bi_2O_3 + CO \rightarrow Bi_2O_{3-\delta} + CO_2^- \quad (2)$$

δ depends on the annealing temperature in vacuum.

At the beginning the FeO_x amorphous phase turns into Fe_2O_3 with increasing annealing temperature, and then it partially converts into the Fe_3O_4 and into the BFO phases (equation 3).

$$3Fe_2O_3 + CO \rightarrow 2Fe_3O_4 + CO_2 \quad (3)$$

The final reaction in the solid-state process with formation of BFO and reduction of carbon could be continued as in equation 4:

$$3Bi_2O_3 + 2Fe_3O_4 + CO \rightarrow 6BiFeO_3 + C \quad (4)$$

The binding energy components located at 532-533 eV (C=O and C–O) are attributed to residual oxygen-containing groups in RGO[121]. These peaks are more pronounced at high temperatures, since the delamination intensity of graphene-like layers increases. A small shift of the peak toward higher binding energies indicates an increase in the bond of the film with the substrate due to the occurrence of solid-phase chemical reactions with the formation of Bi-O-C and Fe-O-C bonds.

Vibrating sample measurement (VSM) analysis

Magnetic measurements were carried out using a vibrating magnetometer (Cryogen-Free High Field Measurement System from Cryogenic Limited) in which a linear magnetometer vibrates a sample mounted on a rod. A magnetic field (up to 1 Tesla) is created using a superconducting magnet with liquid helium. The sample oscillates with a frequency of 21 Hz

near the detector coil, where the induced voltage is amplified and detected, locking time constant 0.3 sec. The measurements were carried out at a low 10 K and a room temperature of 300 K. In order to provide information on the saturation magnetization and coercivity of the samples, hysteresis loops (M-H curves) were constructed. This is done by measuring the magnetization (M) of the sample, depending on the applied magnetic field strength (H) at a fixed temperature. The hysteresis loops are plotted taking into account the antiferromagnetic (AFM) and weak ferromagnetic (FM) contributions. The M-H magnetic hysteresis loops for BFO/HOPG samples before and after annealing, measured at 10 K and 300 K, are shown in figure 3.16 when the magnetic field is applied in parallel to the sample surface. It is known that BFO exhibits low-temperature ferromagnetic behavior, exhibiting hysteresis; one way to verify this observation is to perform a measurement with cooling at low temperatures (10 K). All BFO systems (bulk and thin-film) exhibit weak magnetization due to spin rotation caused by the tilt of the oxygen octahedron, which is characteristic when the temperature drops below Neel.

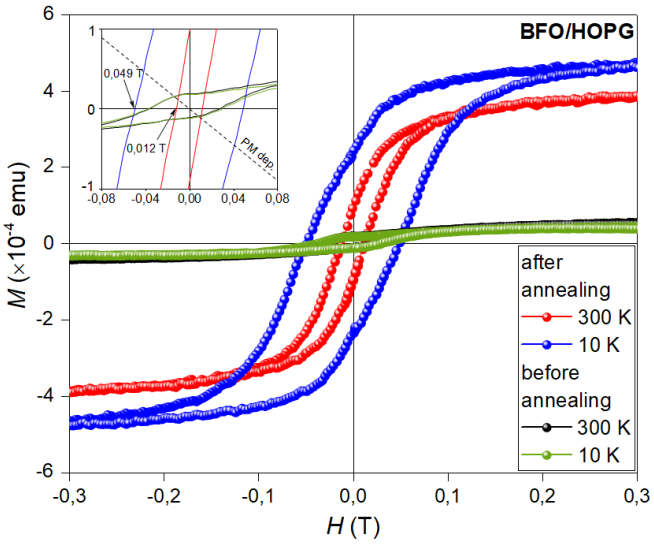

Figure 3.16. The hysteresis loop of the BFO/HOPG structure of the unannealed and annealed sample at 927 K, M-H dependences recorded at room (300 K) and at low (10 K) temperatures. The tab shows an enlarged image of the region with magnetization M = ± 0.0001 emu, at fields H = ± 8 mT.

As can be seen in figure 3.16, the M-H hysteresis loop of the unannealed BFO/HOPG sample practically does not change at room and low magnetization removal temperatures. A soft ferromagnet-like behavior is observed, probably related to the obtained nanoscale structure, which contributes to the appearance of small spin twisting in the structure of the AFM phase film. It is also partially associated with defective inclusions in HOPG formed at the stage of obtaining the ALD layer (Fe-C bond).

In addition, the nature of M-H can be affected by the diamagnetism (DM) of reduced graphene layers in HOPG, which have different values depending on the direction of the applied external field, where $\perp \sim 950$ ($\chi \times 10^{-6}$) and $\parallel \sim 85$ ($\chi \times 10^{-6}$). At the stage of the ALD process, upon separation of the surface region and the formation of bubbles, these values are

mixed and form an intermediate state, which is also associated with the nanoscale formed crystalline phase of the BFO film. A certain AFM(–FM)/DM heterostructure is formed. It is likely that graphite layers affect the overall magnetization of the system, which prevents the growth of film magnetization at low temperatures (10 K) of the unannealed sample. The electronic subsystem of bonds –C=C, –C=O with the obtained film does not allow the AFM state to twist in the film up to low temperatures. Probably, another factor affecting the overall magnetization of the system is the spin-orbit interaction of the reduced graphene layers on the underside of the exfoliated film, which creates anisotropy by partially "blocking" the crystal field, and suppresses the electron spin moment in the AFM phase of the film. It can be assumed that the magnetic properties of the rGO sublayer compete with the spin magnetic subsystem of the BFO film.

Heat treatment of a BFO/HOPG heterostructure sample at 927 K induces crystallization of the deposited films of amorphous-like nature. After annealing, the BFO/HOPG structure behaves differently showing a more significant FM character (figure 3.16), the magnetization grows, and the coercive force also grows from H_c = 12 mT to H_c = 49 mT due to the FM properties of the BFO film. The paramagnetic (PM) contribution of the system has an inclination angle of ~ 42 °, which confirms the existence of oxygen vacancies (V_o). The origin of ferromagnetism in the BFO can be explained by the double exchange interaction. According to the double exchange interaction, the electron transfers from Fe^{2+} to O^{2-} and at the same time, the electrons jump from O^{2-} to Fe^{3+}, thereby completing the electron transfer from Fe^{2+} to Fe^{3+}. More and more theoretical and experimental works provide evidence that magnetic ordering is closely related to V_o [122]. Where V_o additionally cause lattice distortion and leads to an increase in FM. The enhancement of the FM state is likely to be a paradox resulting from the competition between the orbital hybridization of $Fe_{3d} – O_{2p}$ and the crystalline field of FeO_6. When the interfacial region is suppressed in one direction at the interface, the lateral MAE increases. In a recently published paper by Pingfan Chen et. al.[123], the enhancement of magnetic anisotropy and the violation of orbital symmetry in manganite heterostructures is described at length. Authors Yan-Fei Wu et al. [124] reported the effect of magnetic proximity in the graphene/BFO heterostructure leading to strong Zeeman splitting in graphene with an exchange field of up to hundreds of teslas.

Thus, it can be assumed that the great part of the BFO/HOPG structure magnetization is due to two reasons: the charge redistribution on V_o and the contribution of the exchange field of the superlattice at the interface. Due to the creation of a new magnetic configuration in the $Fe^{3+} – O – Fe^{3+}$ sublattice of the BFO structure caused by strong hybridization at the interface as a result of the superexchange interaction with the FM sublattice which is formed at the film/substrate interface, the film substrate (reduced Graphene with Fe-C bonds). The calculation of the FM state magnetization from the obtained values: the saturation magnetization at room temperature M_s = V/M gives the value of M_s ~ 220 emu/cm^3.

3.2.3. Complementary SEM-AFM of swelling Bi-Fe-O film on HOPG substrate

SEM and AFM are the most popular methods in material science for study of surface appearance. They allow diagnostics and investigation of surface and near-surface area in high

resolution. In case of correlative SEM-AFM microscopy SEM provides both imaging and navigation through the region of interest. The same sample can be subjected to AFM measurement for nanoscale data acquisition about surface height. Installing AFM in SEM has several advantages, protecting the device from acoustic vibrations, thermal drift and other noise exposure in the chamber of an electron microscope. In this work, the delamination of bismuth ferrite on a HOPG substrate was investigated. The formation of swelling and bubbles is possible both in heterostructures and in materials of the same chemical composition. Swelling and bubble formation can be both an undesirable result of the film production process and intentional surface modification, for example, by laser irradiation [125].

Morphology of the films depends on parameters of preparation methods and chosen substrate material. The combination of bismuth ferrite and HOPG makes it possible to obtain simultaneously thin films with a magnetoelectric effect and an electrode in the form of a two-dimensional layer of graphite (multi-layer graphene). The symmetry of bismuth ferrite allows the existence of a linear magnetoelectric effect, a spontaneous magnetization, and a toroidal magnetic moment. Observation of these phenomena in bulk samples is impossible because of the presence of a spatially modulated spin structure. The destruction of the latter is possible, both with the replacement of bismuth ions by isovalent cations and by preparation of thin films [126]–[128].

Investigation of delaminations is of interest for both practical applications and the detecting of rare physical effects in this structure. In the near-surface region of the substrate, significant residual stresses arise due to the formation of highly nonequilibrium nanostructured and nano-phase states. The patterns of formation of such states, as well as issues related to their stabilization, are not well-studied yet.

3.2.3.1. Depth analysis of composition

To preserve the stoichiometry of the film during future annealing, it is necessary to create an amorphous layer supersaturated with bismuth. Second ion mass spectroscopy (SIMS) (Fig. 3.17) shows an increased bismuth content at the surface. The bismuth atom is relatively large and has the ability to concentrate on surface defects. The incorporation of bismuth into the defective surface layer of graphite leads to the breaking of weak Van der Waals bonds. The resulting stress in the film leads to the appearance of cracks and peeling. Gaseous reaction products formed during sputtering are caught in the surface layers of graphite, causing swelling. Bismuth near the surface is in the oxidized state, forming inclusion islands. SIMS confirms the uneven distribution of elements on the surface associated with the redistribution and self-organization of elements due to delamination of the substrate.

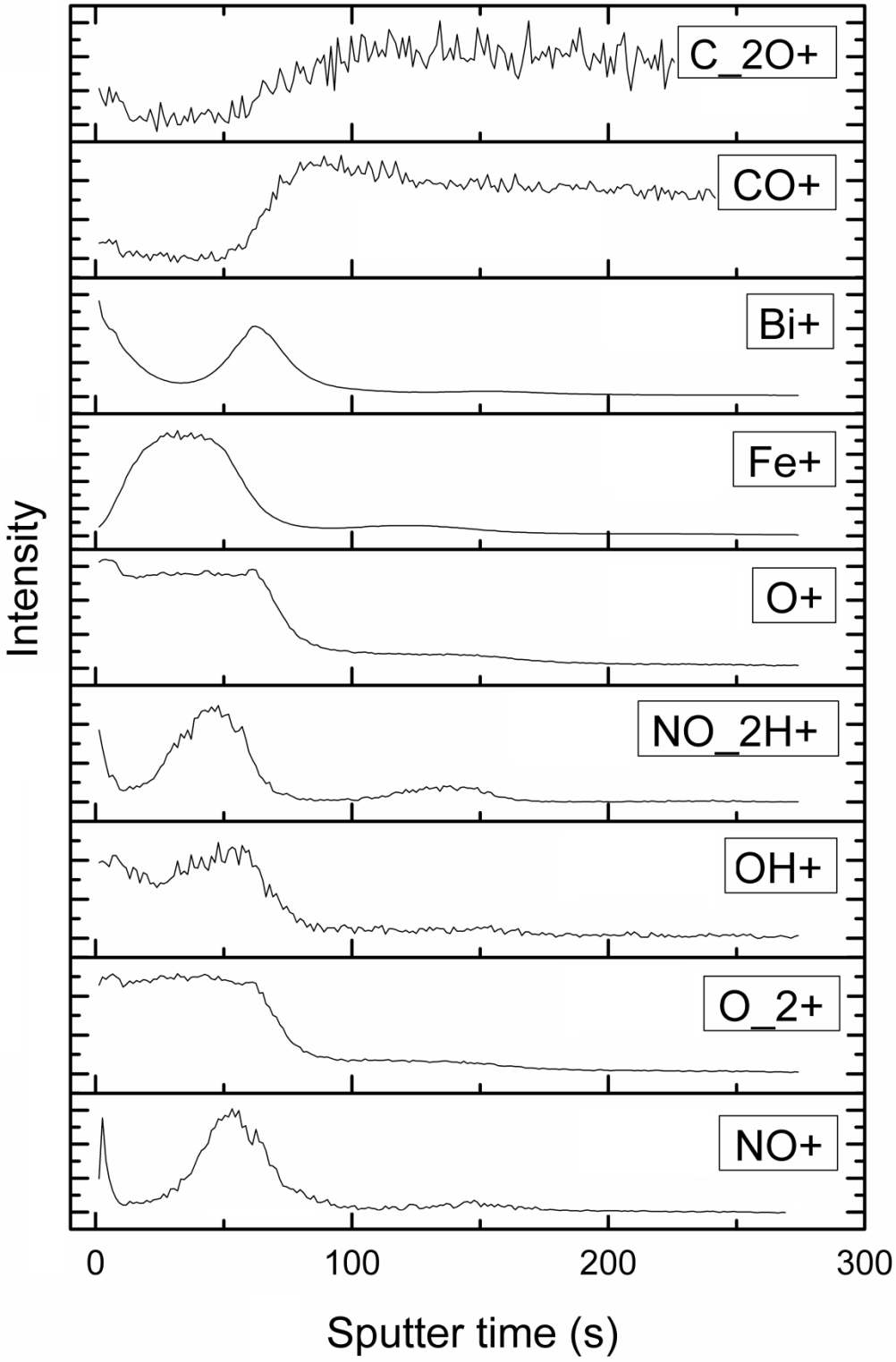

Figure 3.17. SIMS surface component distribution profile.

Oxygen is distributed evenly over the thickness of the film and is a part of iron and bismuth oxides and is also in the combination of gaseous products. The presence of OH bonds is necessary during the ALD process; they are a binding component in the adhesion process. Bismuth concentration is higher on the surface and near the substrate, i.e. on parts of the film with the greatest number of defects and dangling bonds. The use of nitrogen to get rid of residues of the self-limiting ALD reaction led to the formation of nitric oxide on the surface. Bismuth surfactant properties contributed to the retention of gas molecules under the surface of the bubbles and the initial adhesion of the reaction products on the surface of the substrates.

Raman depth mapping is provided by the presence of self-organized bismuth ferrite. It should be noted that Raman spectra depend on the scattering plane (Fig.3.18). The presence of LO and TO phonons is described based on a literature analysis. [129], [130].

a)

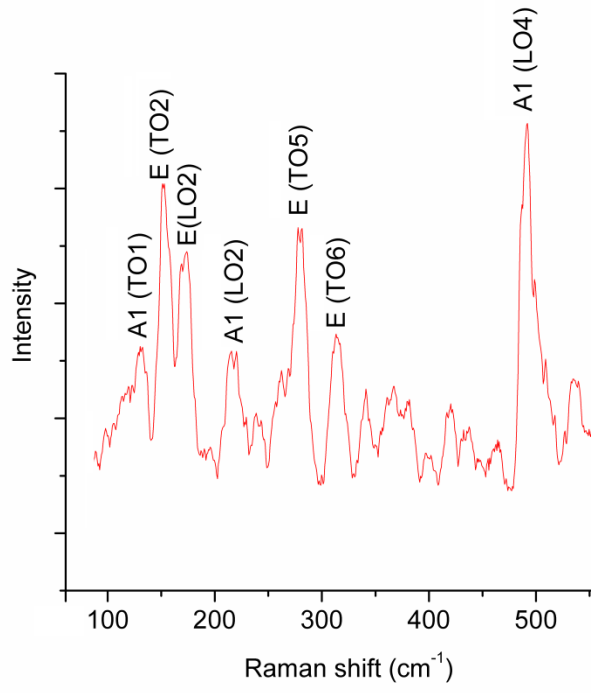

b)

Figure 3.18. Raman spectra a) depth profile and
b) spectra corresponding to bright areas at profile map.

The bright areas in the Figure 3.18a. relate to the places where phonons appear: their intensity is represented in Figure 3.18b on the spectrum A_1 (TO1) 133 cm^{-1},E (TO2) 153 cm^{-1}, E(LO2) 172 cm^{-1} , A_1 (LO2) 216 cm^{-1} , E (TO5) 280 cm^{-1} , E (TO6) 314 cm^{-1} , A_1 (LO4) 489 cm^{-1}. For a detailed study of the surface composition, etching was carried out by a cluster source with an argon ion with the following characteristics: 5 keV Ar500+, 2 mm × 2 mm etching area, 5 sec of pre-etching and post etching time, etching time of one circle was 1800 sec and the depth profile is shown in graph (Fig. 3.19). The data were calculated from surface spectra using CasaXPS software by peaks of Bi4f and Fe2p electrons (Fig.3.20). The reason of low energy and longtime etching is the prevention of preference etching of oxygen. X-ray photoelectron spectroscopy (XPS) shows a significant change in the chemical state of iron [114] and a different degree of oxidation of bismuth during depth profiling. In correlation with SIMS, it also shows a high concentration of bismuth on the surface. XPS data were calibrated to carbon peak at 284.8 eV

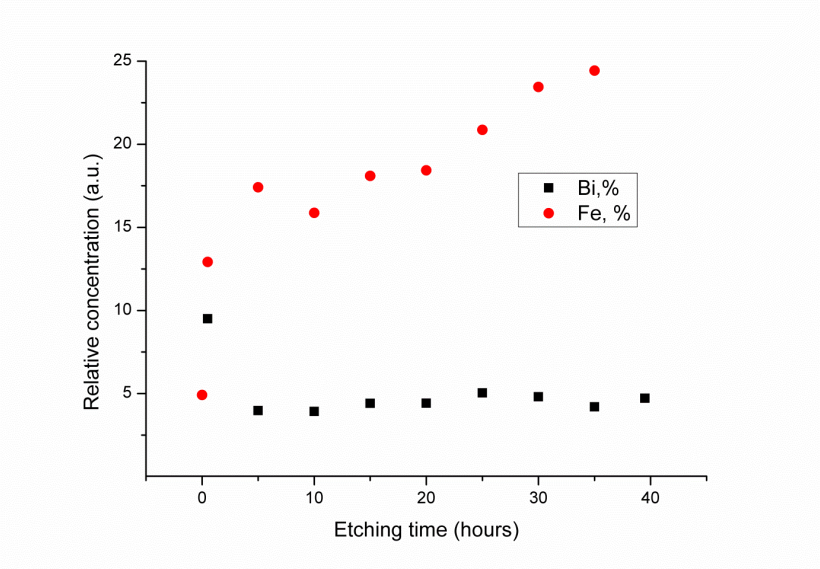

Fig. 3.19. Dependence of relative concentration of bismuth and iron on etching time.

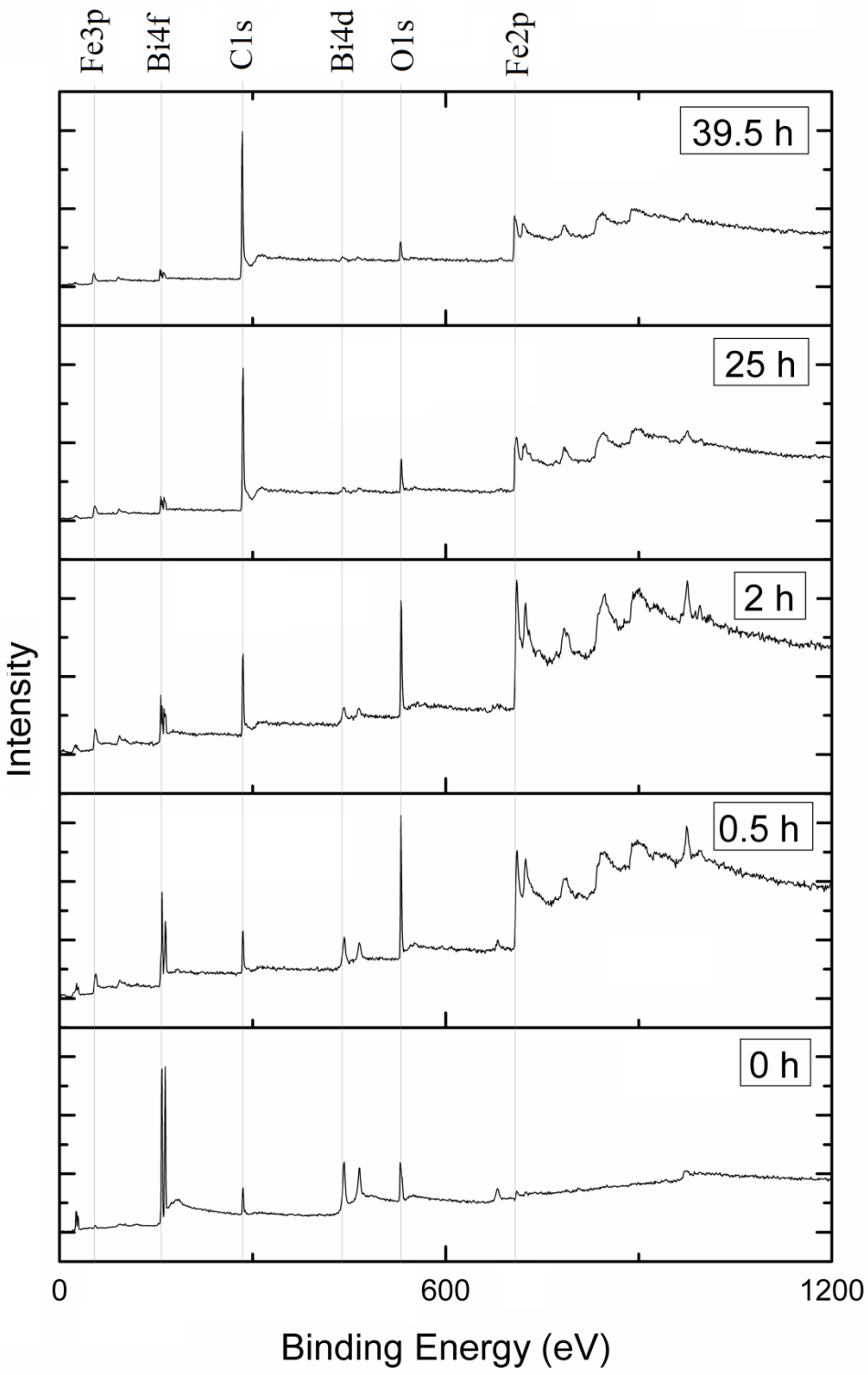

Figure 3.20. XPS survey spectra of the etched surface.

The Fe $2p_{3/2}$ peak shows Fe^{3+} state at 710.8-710.6 eV at the surface and near-surface area (Fig. 3.21). Difference between Fe 2p3/2 and Fe 2p1/2 peak about 14 eV is an evident of presence of Fe^{3+} oxidation state [131]. Slight shift of Fe $2p_{1/2}$ (724,6 – 723 eV) confirms the

appearance of Fe^{2+} oxidation state during etching. Chemical state of Fe^{2+} appears after 39.5 hours of etching at 709.4 eV [132]. Peaks at 707.5 eV and 706.8 eV correspond to Fe-C and pure Fe [133]. They occur after 20 hours of etching and could be clearly observed in Figure 3.21 after 25 hours of etching. Even after 39.5 hours of etching the characteristic Fe^{3+} peak could be observed at 719 eV and 720 eV satellite peaks. The surface before profiling is converted by Bi^{3+} and shows XPS peaks of Bi $4f_{7/2}$ and Bi $4f_{5/2}$ at 158.9 eV and 164,3 eV [134]. After 0.5 hours of etching the splitting occurs indicating appearance of metallic bismuth alongside of bismuth oxide (Fig.3.22). Shift of the binding energy to lower energies for Bi4f spectra is connected with presence of defects and amorphization of bismuth closer to HOPG substrate. Increasing number of free electrons caused by broken Van der Waals bonds also contribute to low-energy shift of the spectra due to increasing length of Bi-O bond. Spectra displacement after long-time etching to smaller binding energies also indicates decreasing of interaction between bismuth oxide and oxidized graphite surface [135]. Etching over 39.5 hours reveals bismuth peaks at 164.08 eV and 158.78 eV which are assigned to bismuth subcarbonate composition [136].

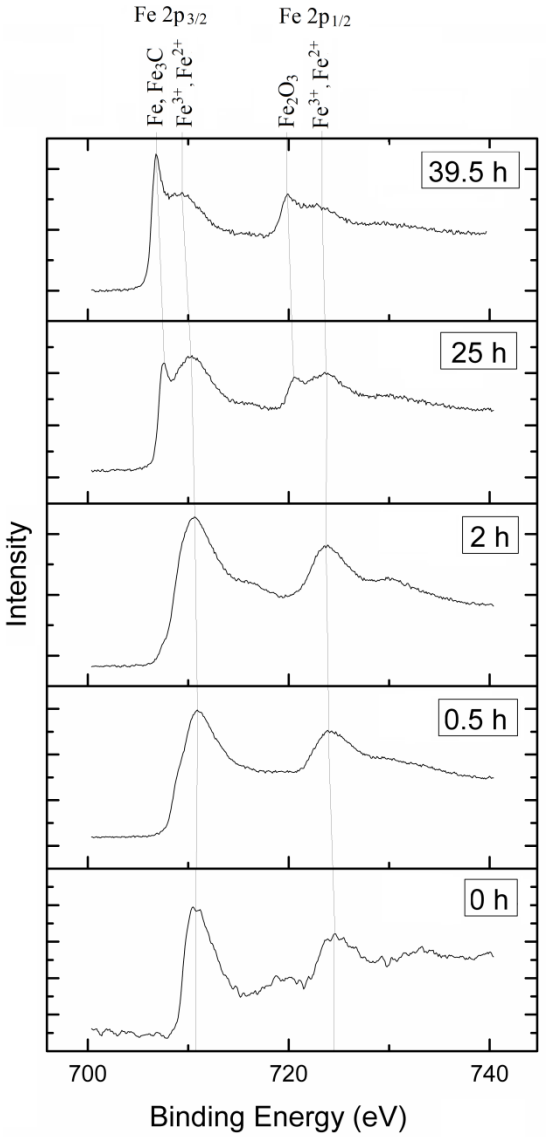

Figure 3.21. XPS spectra of Fe2p of the etched surface.

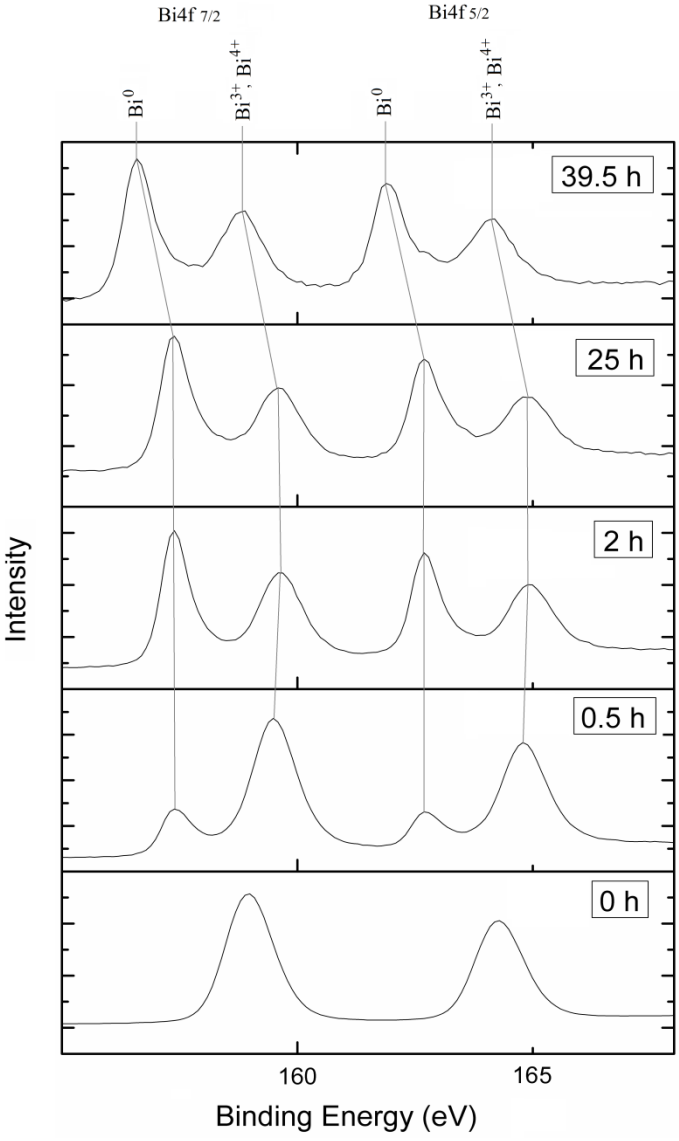

Figure 3.22. XPS spectra of Bi4f of the etched surface.

According to Jaiswar Sh. and Mandal K.D. [137], O1s XPS peaks at lower binding energy (529–530.7 eV) are attributed to lattice oxygen. Carbon oxide on the surface of the samples is reflected by O1s XPS peak at 532 eV. After etching of the film, this peak appears as a part of the shoulder at 531–532 eV. The spectra shoulder around 531 eV refer to excess oxygen (marked as O^-) [138]. Incorporated nitro (532.7 eV) [139] and hydroxyl (533 eV) [140] groups cause shift of O1s and are responsible for the high-energy shoulder (Fig. 3.23). Besides the calibration of C-C peak, C-O-C bond could be observed at 286 eV at the shoulder of C1s peak (Fig.3.24).

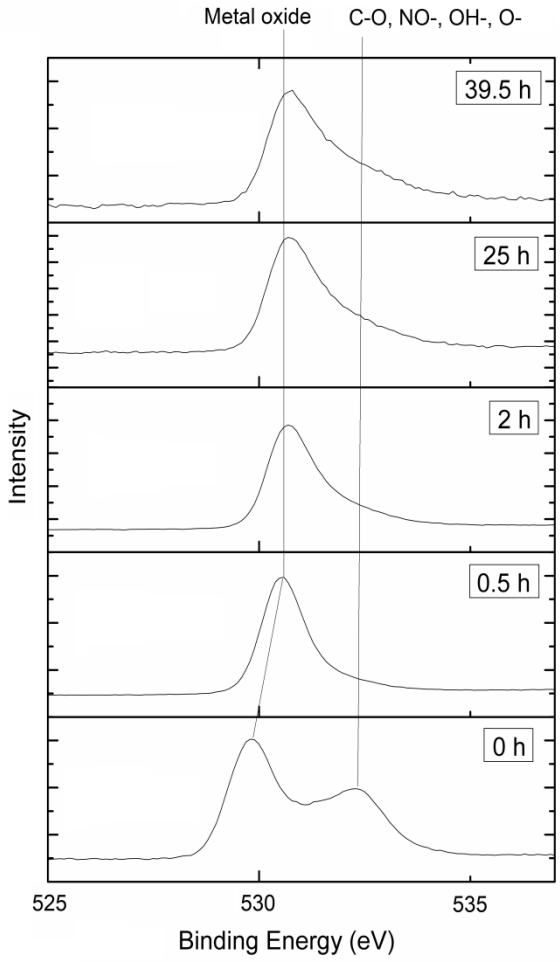

Figure 3.23. XPS spectra of O1s of the etched surface.

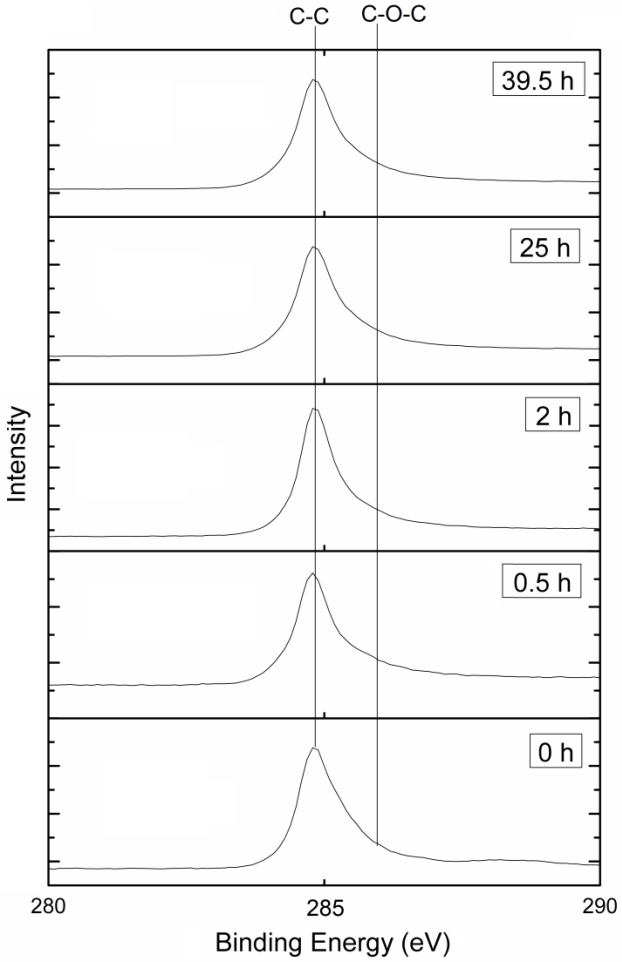

Figure 3.24. XPS spectra of C1s of the etched surface.

3.2.3.2. Correlative SEM-AFM analysis

The experiments were carried out using a scanning probe microscope. Litescope (Nenovision) integrated to SEM Lyra 3 (Tescan). Topography detection is, in this case, performed by self-sensing Tuning Fork probes, which detect the change in their resonance properties due to the change of distance to the sample.

Chamber pressure during measurement was 10^{-2} Pa. When measured in air, the pressure was normal, equal to 101.325 Pa. Scanning of topography at atmospheric pressure was carried out immediately after scanning in vacuum. This allowed to avoid excessive pollution from outside and accidental jumps to another area, which could be the result of mechanical manipulations. To confirm the reliability of the results, the depth of the craters, formed at the places where the film is no longer, was measured. It remained virtually unchanged both in vacuum and at normal pressure. The difference was a slight decrease in the noise signal when measured in vacuum (Fig. 3.25). However, the height of the “bubbles” was changing and was greater than the “bubble” itself was originally. This is due to the high gas content in it.

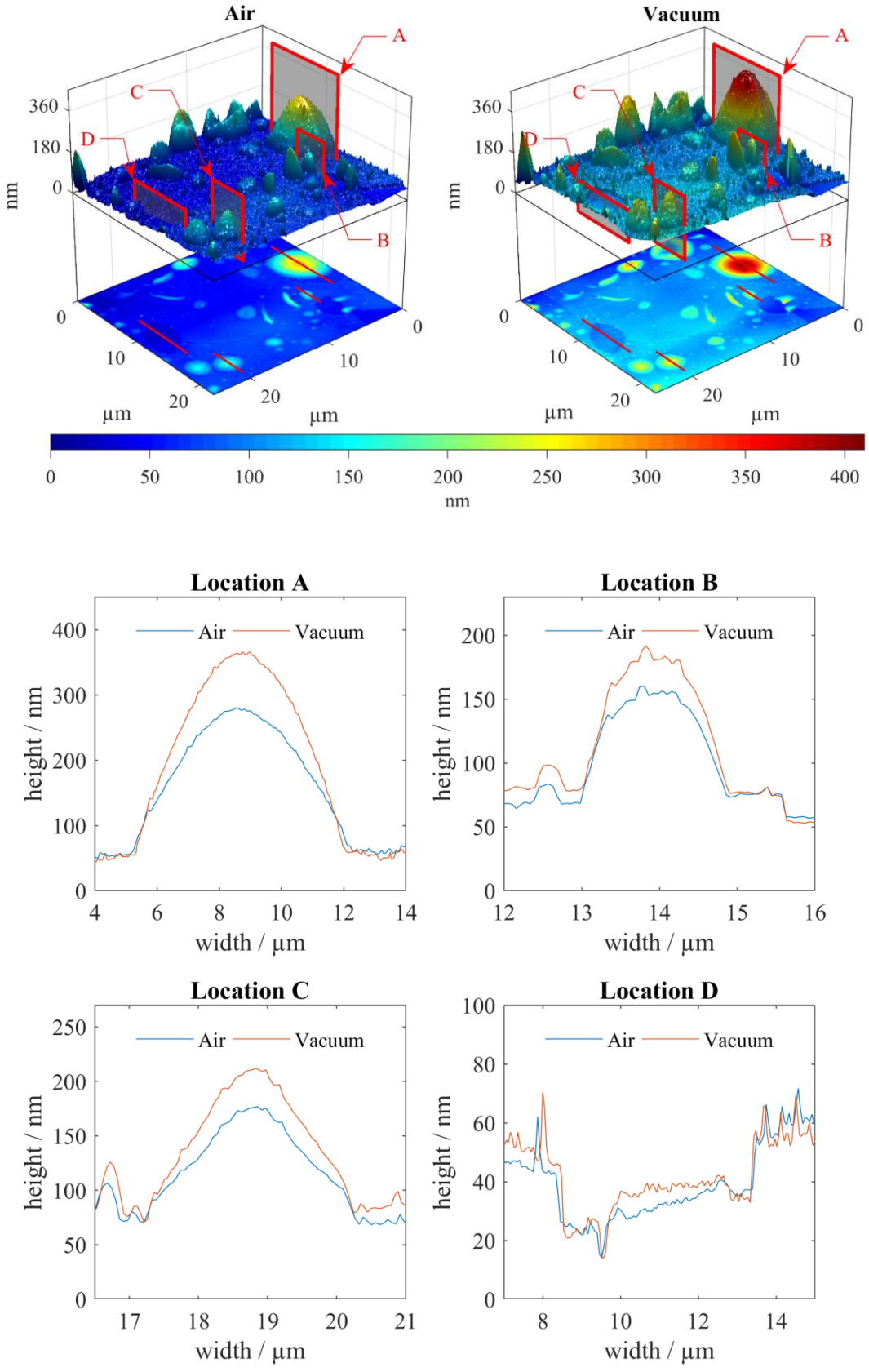

Figure 3.25. The image of the swollen part in vacuum and in air, and also comparative profiles of the height of the bubbles and holes.

The results aim to fill the space in the field of BFO preparation on graphite substrates. The presented data demonstrate the first step of BFO preparation by the ALD method. It is worth noting that further annealing is required for the crystallization of BFO. The observed film delamination effect can be used to further obtain 2D nano dimensional materials by mechanical (for example, ultrasonic) collection of exfoliated flakes.

AFM measurements show dome-like structures and holes on the sample. When the topography imaging by AFM is merged with SEM material contrast, a distinct difference between holes and surrounding material can be seen, as well as the height and thickness of the film. Formation of these bubbles can be explained as a local delamination caused by compensation of surface tension created by differing crystal conformation of the substrate and the thin film [141].

Combination of SEM and AFM is useful in many ways. SEM allows for precise navigation of the AFM tip on the surface, and for a constant tip quality control as well. Because the same areas are being measured by two techniques, overlapping of the results provides better material and topographical information than just one method on its own. SEM measurement can also provide additional information about electric and magnetic properties, which would not be seen under AFM. This makes the AFM and SEM combination an ideal measurement tool for evaluation of nanomaterials, especially carbon-based nanostructures [142].

When in proximity to the measured sample, the probe can be affected by a number of forces: mechanical contact force, van der Waals forces, capillary forces, electrostatic and magnetic forces, Casimir forces, chemical bonding, solvation forces etc. depending on the setup of the microscope and the probe [143]–[145]. These probes consist of a silicon fork and a tip. Alternating current is used to induce vibrations in the fork on its resonance frequency.

This allows the probe to function as a detector as well, as any changes in the frequency after calibration show the change in forces affecting the probe, and therefore difference in sample topography. Semi-contact mode has been used here. A probe is kept in such a distance from the surface, that during vibration of the cantilever it comes into brief contact with the surface [146]. Due to lower lateral and capillary forces than other measurement modes, semi-contact mode reaches higher resolutions, while being more stable and friendlier to the sample as well.

Correlative SEM-AFM allows fast and easy comparison of images from both techniques regardless. Localization of the region of interest using SEM allows to quickly focus on the surface of the sample by selecting the desired scan area (Fig. 3.26). At certain values of the electron beam parameters, a thin film of the material can be transparent. In the images presented in this work, under the transparent film, topography elements of the lower layers were visible. AFM makes it possible to simultaneously determine the height of a transparent (under the given SEM conditions) nanoscale layer. The high sensitivity of the AFM in vacuum allows you to accurately determine the height of the material located on the substrate.

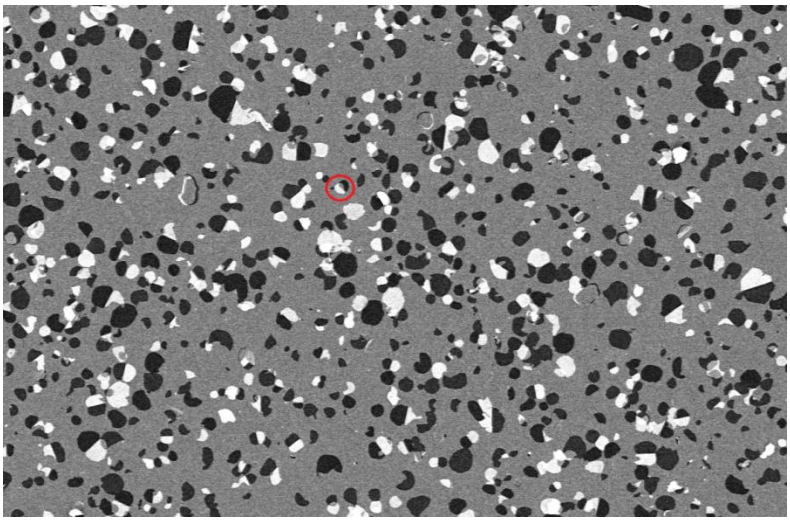

a)

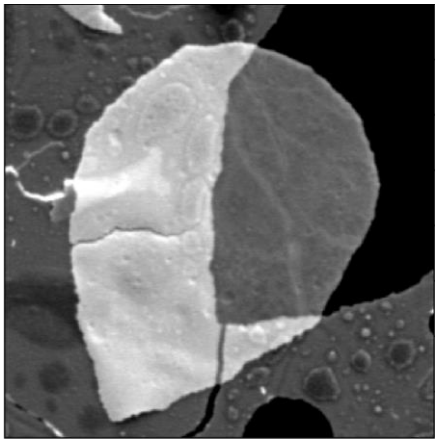

b)

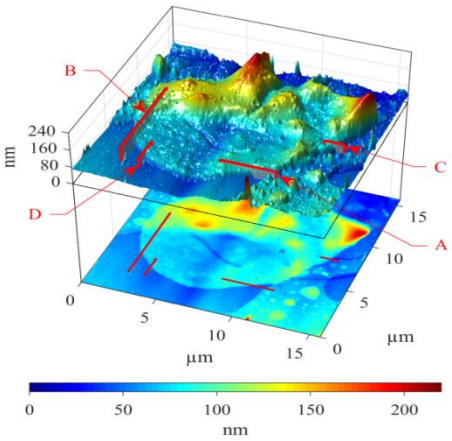

c)

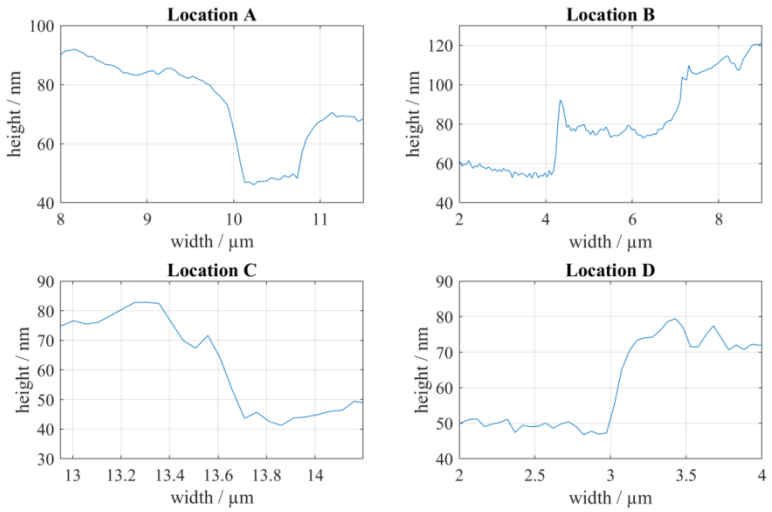

d)

Figure 3.26. SEM and AFM of the detached portion of the film and held on the surface of the sample by electrostatic interaction: a) large area SEM image, b) detailed SEM image, c) AFM image of the region of interest, d) profiles of the chosen areas at AFM image.

HOPG can be considered as graphene layers connected by van der Waals forces. Graphene, in turn, is known as a material capable of retaining substances in a gaseous state. The problem of adsorption of ferrocene compounds on the HOPG surface was theoretically and practically considered in [147], where the increased adsorption of molecules resulting from redox reactions on surfaces exposed to atmospheric conditions was confirmed. Adsorption is expected to be enhanced due to the presence of ozone and surface defectation by intercalated bismuth atoms. This leads to swelling, as a result of gas aggregation under a growing film layer. The carbon oxide on the surface of HOPG in defective areas also contributes to swelling and delamination of the film.

The reactive gas inside the chamber was only partially ionized. Due to the presence of non-ionized oxygen atoms, reactions are possible (5):

$$\begin{aligned} N_2+O_2&=2NO \\ NO+O_3&=NO_2+O_2 \\ NO_2+O&=NO+O_2 \\ NO_2+CO&=NO+CO_2 \end{aligned} \qquad (5)$$

These reaction products can be captured by surface defects, causing even more stratification of the surface. The presence of the described compounds is confirmed by SIMS data. The XPS spectra of oxygen also indicate the possible presence of a bond of oxygen with nitrogen. The observed swelling is a consequence of compressive mechanical stress as well as the presence of gas products, which can form even more in a vacuum. Kinks and cracks arise as a result of tensile deformations.

Only spherical elements of a swollen film is considered. Knowing the pressure difference and the change in the radius of the film, the following values can be calculated using following equations.

According to [148], swelling can be calculated (6):

$$S=(V-V_0)/V_0, \qquad (6)$$

Where V_0 in our case is the volume under normal pressure, and V is the volume in vacuum.

The swollen element has the shape of half an ellipsoid, the volume of which can be calculated as half the volume of an ellipsoid (7):

$$V=(1/2)\ (4/3)\ \pi \cdot a \cdot b \cdot c \qquad (7)$$

a, b and c are the radii of the ellipsoid. In the process of evacuating the vacuum, only one radius changes (denoted by a1), the other two characterize the circle on which half of the ellipsoid (b, c) rises. For location A in Figure 3.25, swelling is S=0.52.

Using data on the height of the tension (swelling) in vacuum, you can calculate the surface tension. Inside the bubbles, there is excess pressure, which is compensated by the action of surface tension forces.

The excess pressure under the surface of half an ellipsoid can be described as (8):

$$\Delta p = 2\sigma/a \quad (8)$$

The total pressure exerted on the film consists of the pressure of the medium and the excess pressure of the gases inside. Comparing the total pressure in vacuum and at normal pressure we get (9):

$$10^{-2}\ \text{Pa} + 2\cdot\sigma/a = 101325\ \text{Pa} + 2*\sigma/a1 \quad (9)$$

Substituting Location A Figure 3.25, the surface tension σ is equal to 6,2 mN/m.

Based on the available data, one can also calculate the excess potential energy of surface molecules ($\Delta E = \sigma\cdot\Delta S$, here σ- surface tension, ΔS - area of the layer) and other parameters.

Upon rupture of the swelling region, a hole is formed, which modifies the surface of the graphite substrate. Bubble rupture is associated with both internal factors, (the amount of gas contained in them and their shape), as well as external ones (pressure and temperature [148]).

This expansion is limited to its height only, however, and does not increase the width of the bubble, which supports the case for this expansion being a result of pressure change. A rupture occurs as a result of local stress exceeding the elastic ability of the thin film to compensate, resulting in formation of the hole and exposing the material beneath.

The results show that simultaneous SEM-AFM contributes to obtaining of structural information from local regions as morphological, geometric, physical and chemical characteristics. This is important for a better understanding of the many aspects of materials science such as defects, phase transformations etc. and correct interpretation of surface topographic features as well as its functional role for the test surface in relation to material performance and lifetime.

The obvious advantage of a combination of these techniques is to obtain more complete information about surface morphology. This technique is useful for evaluating the interaction of a material with an electron beam as a function of film thickness. The ability to conduct probe scanning in vacuum and in air, on a site localized by SEM, allows us to study the mechanical properties of nanoscale structures.

Effect of swelling should be taken into account during deposition of the next layers. Appearance of the delamination changes potential energy of the surface which is dependent on its area.

3.3. $BiFeO_3$ on silicon carbide

Appendix 3 contains the information about the importance of silicon carbide (SiC) as a material and its possible incorporation into silicon technology. The structures were obtained by the procedure for HOPG ALD described above. The samples annealed up to 920K at air and in vacuum. Annealing in vacuum caused formation of oxygen vacancies. VSM data confirm possibility of control magnetic properties by oxygen termination. The presented curve was not corrected by subtraction of diamagnetic contribution.

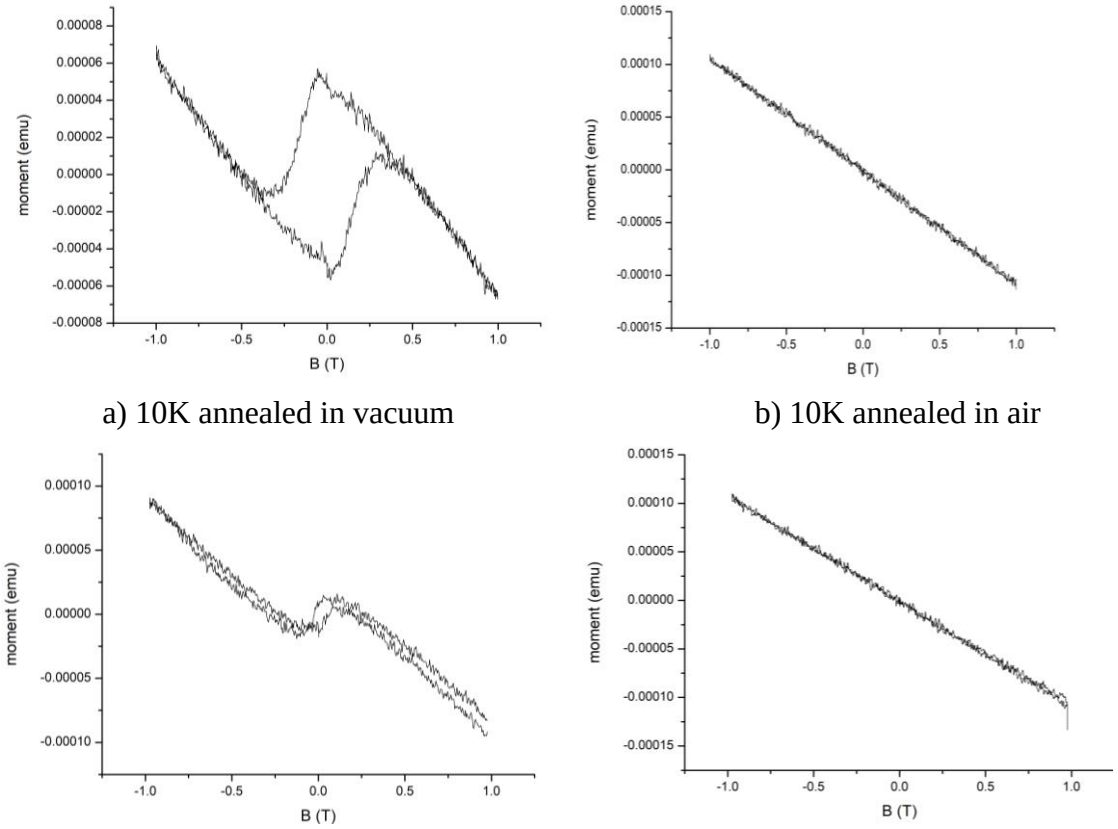

a) 10K annealed in vacuum b) 10K annealed in air

c) 300K annealed in vacuum d) 300K annealed in air

Figure 3.27. VSM of the samples at 10K and 300 K for BFO/SiC a,c) BFO/SiC annealed in vacuum and b, d) BFO/SiC annealed in air.

The presence of oxygen vacancies is confirmed by fluorescence measurements (Fig.3.28). Fluorescence of the samples is caused by defects, such as vacancies, adsorbed molecules that influences charge state of the thin film. Fluorescence data are related to the Fermi level. Studies of Fermi level and the bandgap information were obtained from UPS (Fig. 3.29).

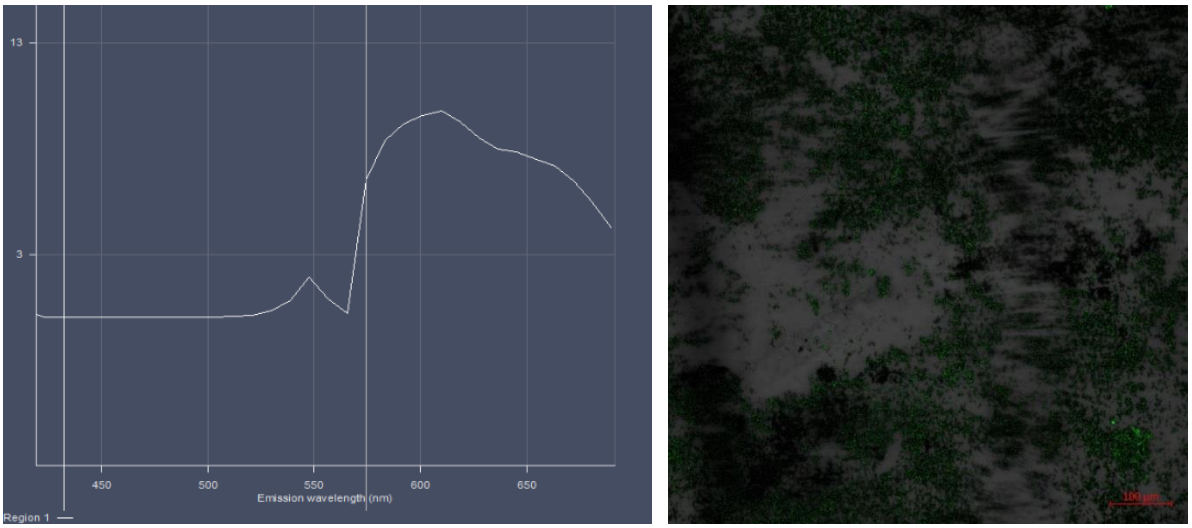

Figure 3.28. Surface fluorescence of a $BiFeO_3$ sample of a film obtained on a SiC substrate; on the left is the total spectrum from the film.

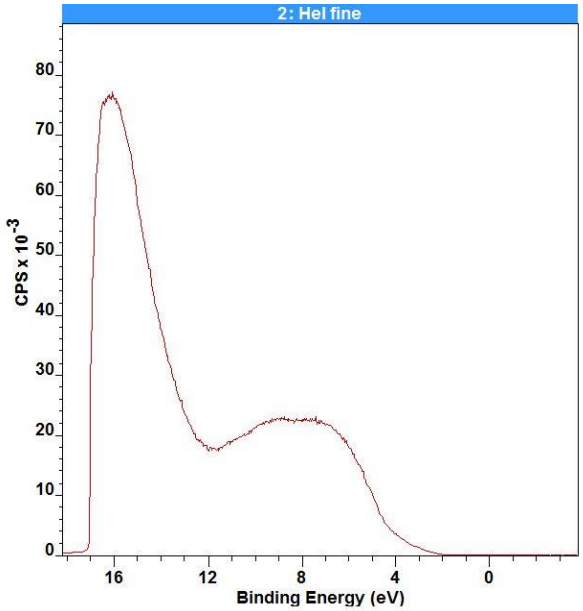

Figure 3.29. UPS spectra of the BFO/SiC annealed in vacuum.

The UPS spectrum shows that the band gap is approximately 2.4 eV, which is in correlation with optical measurements and the ellipsometry model. For control of surface conditions the AR-XPS measurements were done. The results are shown in figure 3.30.

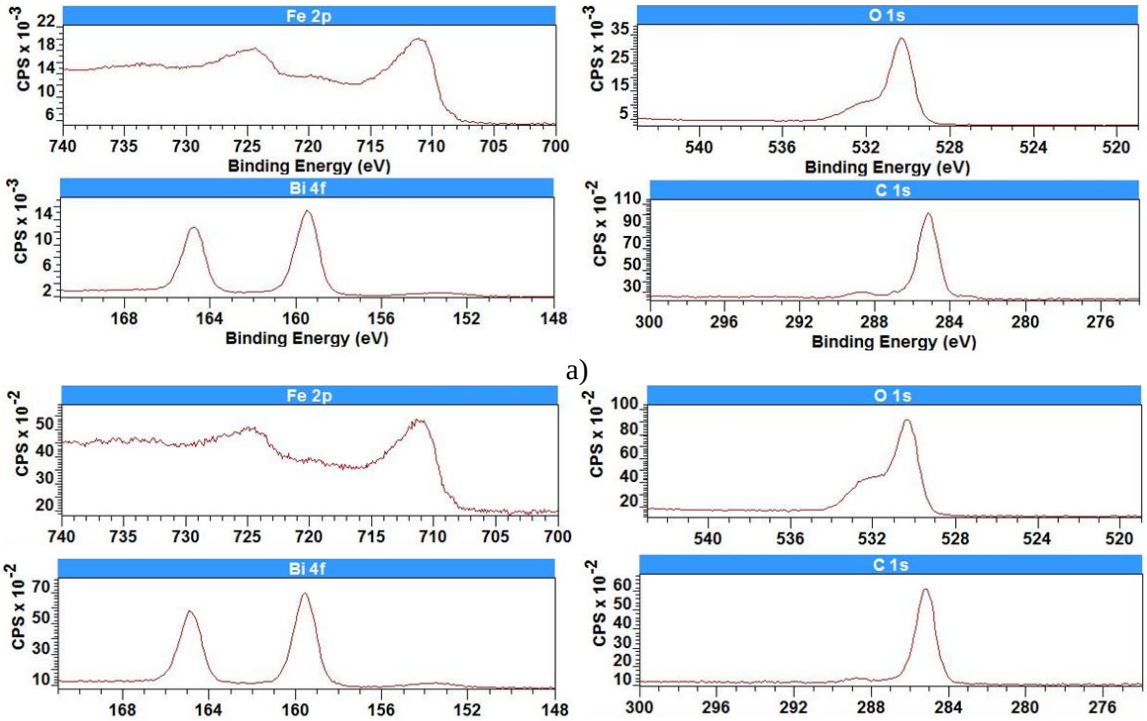

a)

b)

Figure 3.30. AR-XPS of iron 2p, oxygen 1s, bismuth 4f and carbon 1s:
a) at 0 degree; b) at 63 degree.

As can be seen from the AR-XPS figures, the relative concentration of oxygen vacancies at the peak in the region of 532 eV decreases; the ratio of Fe^{2+} and Fe^{3+} changes over the Fe2p spectrum, which is associated with oxygen in the crystal lattice of the obtained bismuth ferrite film. Bismuth is practically unchanged. The carbon peak shows the surface residual carbon on the surface of the sample over which the main peaks of the spectrum were aligned.

The scans and profiles presented in figures 3.31 show piezoresponse behavior of the films applying voltage of 10V and -10V. Changing the voltage of the cantilever changes almost the entire surface. According to AFM (first figure) and the average value of the profile, it can be seen that the film is nanocrystalline. Possible to speculate that the BFO film has grown oriented in one direction. Further, when studying PFM scans, the film surface is charged in a certain way, without supplying voltage, it partially has a charge, which can probably be associated with the piezoelectric property of the film and, under mechanical pressure, the cantilever responds to external influences. The occurrence of dielectric polarization under the action of mechanical stress. When a positive potential of U = 10 V is applied, the film reacts entirely, small surges appear, and in addition a modulating signal appears at a distance of 3-4 nm, which is probably associated with the inverse piezoelectric effect. Perhaps this is due to the two-phase nature of the formed structure of the BFO film (rhombohedral and tetragonal). When the supply potential changes to the reverse U = -10V, the modulating signal disappears but the charge on the surface changes, which indicates the heterogeneity of the electric polarization in the resulting film. This is probably due to the magnetoelectric effect in the BFO film due to the inhomogeneity of the internal magnetic field and the uncompensated charge Fe^{2+-} Fe^{3+}.

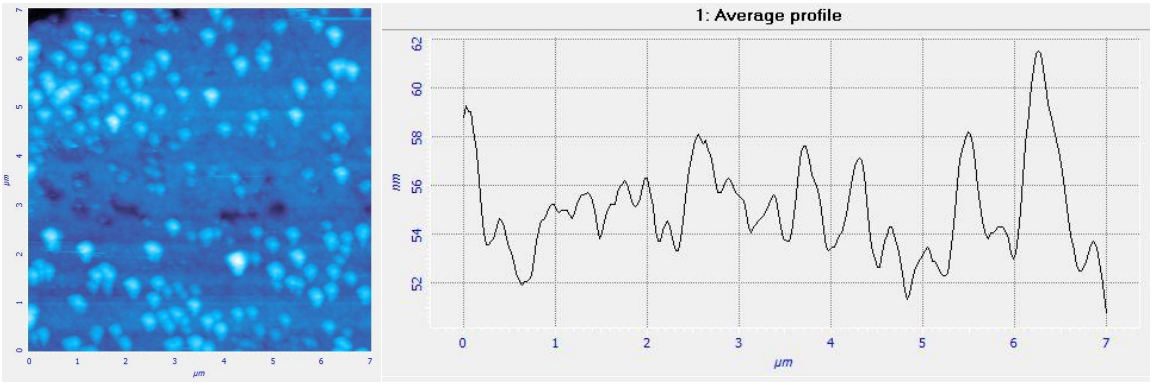

a)

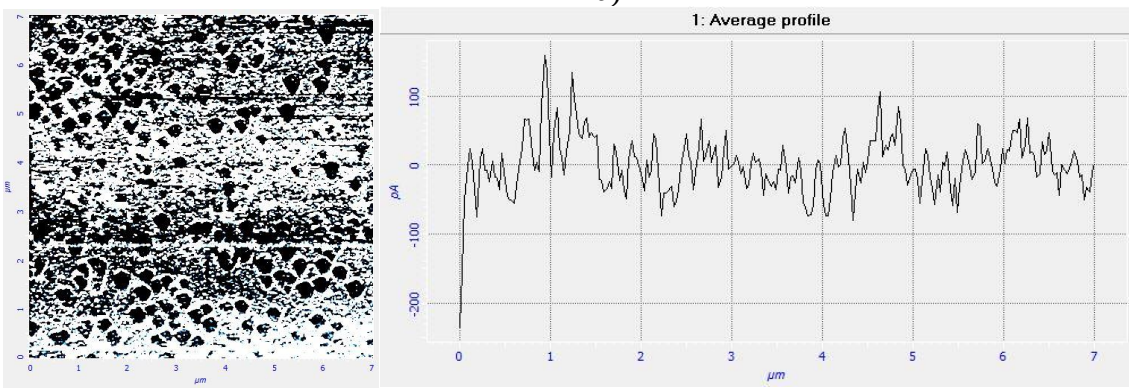

b)

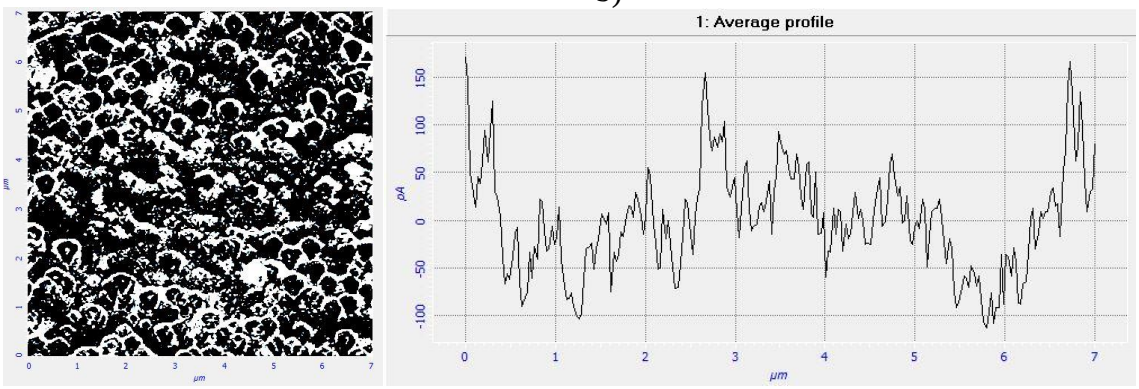

c)

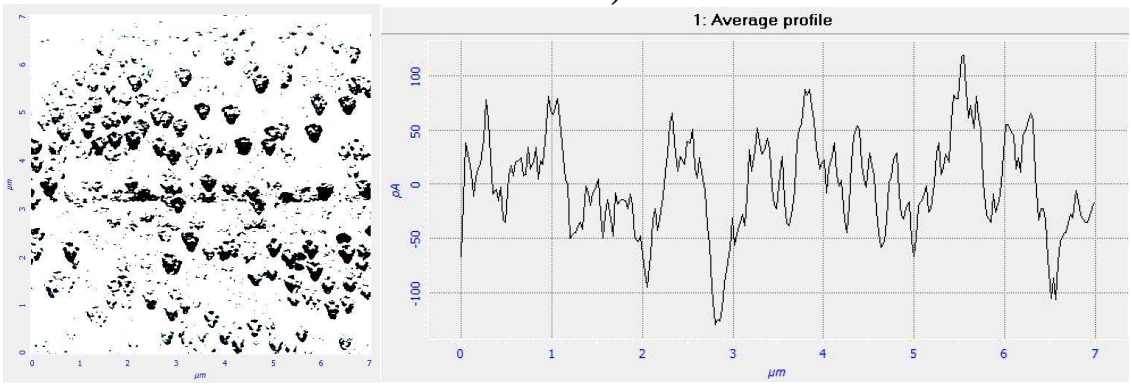

d)

Figure 3.31. PFM of the BFO/SiC annealed in vacuum: a, b) topography and amplitude PFM signal at 0V bias voltage; c) amplitude PFM signal at 10V bias voltage; d) amplitude PFM signal at -10V bias voltage.

MFM was carried out without and in presence of electric potential between the probe and the sample (Fig.3.32). The distance between probe and surface during MFM was 100 nm.

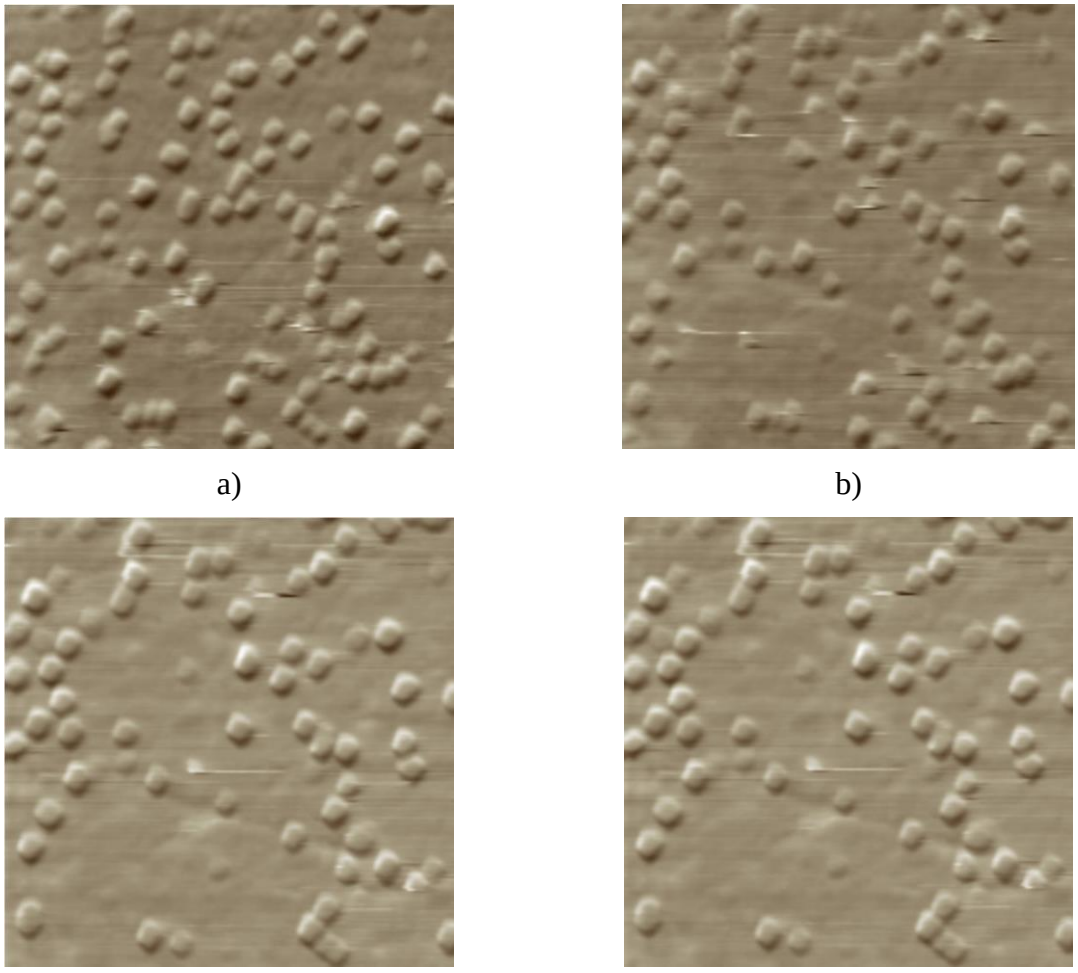

a) b)

c) d)

Figure 3.32. MFM of the BFO/SiC annealed in vacuum: a) at 0V bias voltage; b) at 1V bias voltage; c) at 5V bias voltage; d) at 10V bias voltage.

As can be seen from the figures, ferromagnetic inclusions occur in the antiferromagnetic phase of bismuth ferrite. When the switching voltage changes, some inclusions disappear, which tells us about the magnetoelectric coupling in the film. Most likely, due to the appearance of oxygen vacancies in the lattice during annealing in vacuum, the $BiFeO_3$ phase partially transforms to magnetite Fe_3O_4. During annealing, Bi atoms from the near-surface region are depleted and also form vacant Bi_o sites.

3.4. BFO on Kapton tape

Polyimide Kapton is a material developed by DuPont company, with many interesting properties. It mostly takes shape of a tape or a thin film covered laminated with other materials or without any lamination. The material takes a form of polymerized aromatic dianhydride with aromatic diamine [149](Fig. 3.33).

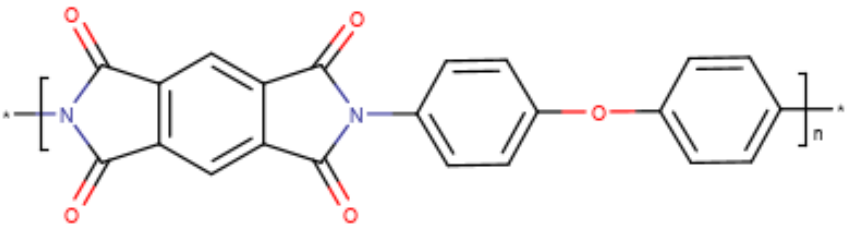

Figure 3.33. Chemical structure of polyimide Kapton.

Kapton tape in particular finds use in many fields of science and industry because of its ability to keep its properties in many areas under severe conditions, like wide thermal spread, corrosive environment or electrical discharges. Extensive tests from the side of the manufacturer provide a lot of important data about the material, and because of its properties and their stability Kapton tape can be found anywhere from a substrate for coating by other materials to insulation of specific systems on spacecraft. An interesting application that Kapton also offers is the possibility of using it in flexible electronics. This can be useful in many fields, for example spintronics, where lots of mechanical bending is expected [150], or biological applications, where any sensors or electrodes need to be highly flexible and have long time of life without breaking or affecting the environment they are inserted into in any way [151].

Thermal

Even though it is highly stable in both low and high temperatures, prolonged exposure to boiling water was shown to reduce the level of Kapton film properties. Because of the manufacturing process, where residual stress is embedded into the film, it will experience a reduction in dimensions upon first exposure to high temperatures. After this first shrinkage a normal progress of thermal expansion is expected. Thermal deterioration of the film is a function of temperature and oxygen concentration, where the deterioration progresses faster with the increase of either of the two factors. The oxidative degradation is more prevalent in high-temperature environments, therefore, to prevent quick decrease in useful life of the film, an alternate atmosphere to air is required [152].

Electrical

Dielectric constant of polyimide Kapton films is usually stated as 3.0 to 3.5 and dielectric strength of 150 V/μm to 300 V/μm under standard testing temperature (23 °C) and relative humidity (50%), dependent on the specific type of the film. The water content in polyimide material can cause changes in electrical properties in atmospheres with different relative humidity, increase in which causes dielectric strength to decrease and dielectric constant to

increase [153]. Temperature changes are known to cause smaller changes in electrical properties, though not completely insignificant [154]. Frequency, on the other hand, has little to no effect on dielectric constant of the material, even though increase in frequency causes dissipation factor to grow slightly [155]. Kapton material is resistive to corona discharges as well, but when exposed to high levels for a long time, its dielectric properties will eventually deteriorate. As material useful life under corona discharge is a function of many properties, application in areas with corona discharges present needs to be judged on a case by case basis. Original testing by the manufacturing company has shown, however, that polyimide Kapton is capable of withstanding at least some levels of corona exposure without failing [156], [157].

Chemical

There are no known organic solvents for polyimide Kapton, though it is possible to degrade the material by using sodium hydroxide solution. Polyimide Kapton also has a great radiation resistance, which is the reason for its frequent use in outer space applications, or other high radiation locations. Use in devices like accelerators or nuclear reactors is conditioned by resistance to not only radiation, but also aggressive chemicals, including sodium hydroxide, and water vapors, both of which are known to disrupt the material integrity of Kapton. This must be taken into consideration when using the material, as well as the reduction of properties when exposed to high temperature and ultraviolet radiation and oxygen at the same time [158], [159]. The study of chemical conditions of the surface was made by XPS before Bi-Fe-O deposition (Fig.3.34)

The use of polymeric materials to modify the properties of bismuth ferrite and create hybrid materials based on it allows one to combine the mechanical superiority of polymeric materials (flexibility) and the electromagnetic properties of multiferroic. Such polymers as polyaniline (an example of a conductive semiconductor) or polyvinylidene fluoride (a piezopolymer) began to be widespread at modern technologies. The use of strong mechanical stresses, as well as the introduction of dopants (which is a way of creating mechanical stresses at the level of the crystalline lattice), can destroy the spatially modulated structure.

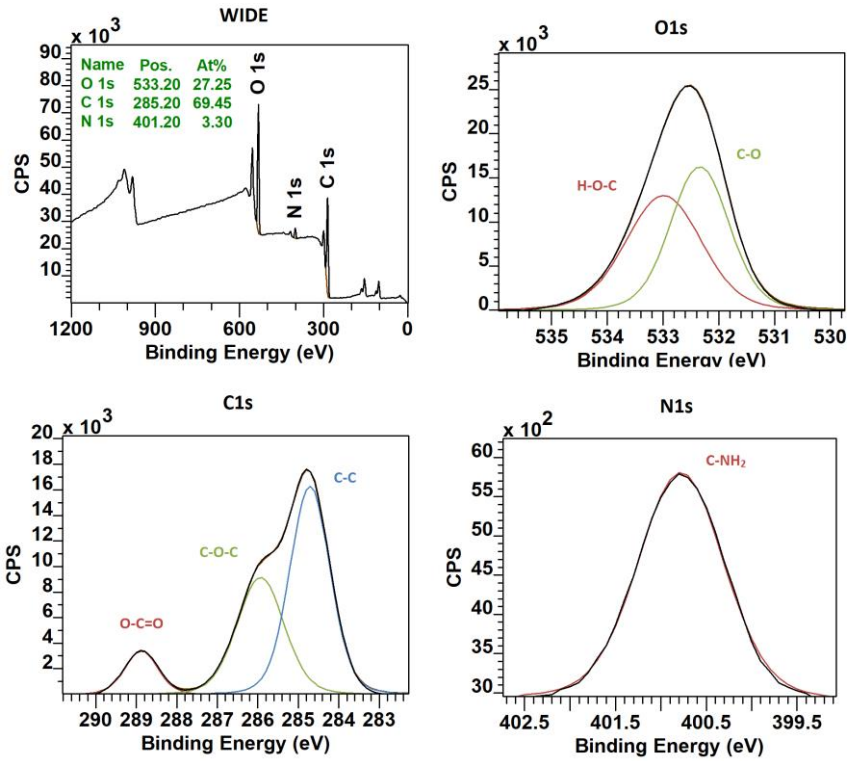

Figure 3.34. XPS spectra of the Kapton substrate.

3.4.1. Synthesis procedure

Kapton (poly (4,4'-oxydiphenylene-pyromellitimide)) was used as substrates for the growth of an amorphous film in the Bi-Fe-O system. It is stable over a wide temperature range from −273 up to +400 °C.

The films of Bi-Fe-O composition were prepared at ALDCERAM® ML-200 device. The source for bismuth component was $Bi(mmp)_3$ (Tris(1-methoxy-2-methyl-2-propoxy) bismuth, Sigma-Aldrich). Ferrocene was the source of iron ($Fe(C_5H_5)_2$, Sigma-Aldrich). In the time interval between the start of the pre-cores, ozone (O_3) was supplied to the chamber for 5 seconds. The purge was carried out using N_2 with a purity of 5.0, the purge time was 15 sec. The evaporation temperature of $Bi(mmp)_3$ was approximately 415 K. The optimal temperature for evaporation of the ferrocene precursor was 360 K. The chamber was heated uniformly 500 K. The gas at the outlet was kept at a constant temperature of 420 K. The pulses ratio between the times of iron and bismuth precursors injection was $N_{Fe}/N_{Bi} \approx 5/3$ (2 sec/1.2 sec). In the second experiment, the ratio between the precursor action times was $N_{Fe}/N_{Bi} = 1/1$ (2 sec/2 sec). All other parameters of both experiments were similar, including the number of cycles in the first and second experiments was 480. These ratios were chosen based on matching of ionic radii of iron and bismuth, $R_{Fe}^{+} = 0.087$ nm and $R_{Bi}^{+} = 0.120$ nm, where the growth rate of the bismuth oxide layer will be greater. Thus, the difference in two experiments from the regular ratio of the formation of a common oxide based on iron and bismuth in the system Bi-Fe-O ~ 0.32 nm. That allows determining the pattern of self-

organization of the oxide layer with predominantly bismuth phase (segregation of metallic bismuth).

3.4.2. Characterizations

An analysis of the topography of the films contributes to the development of a theoretical base explaining the principles of the film preparation by the ALD method and modeling of hybrid materials. This will improve the reproducibility of the required structures and physical properties of the films. AFM images (Figure 3.35) show the presence of nanoscale features on the surface of the Kapton film. Different topography is mainly caused by organization of bismuth on the surface.

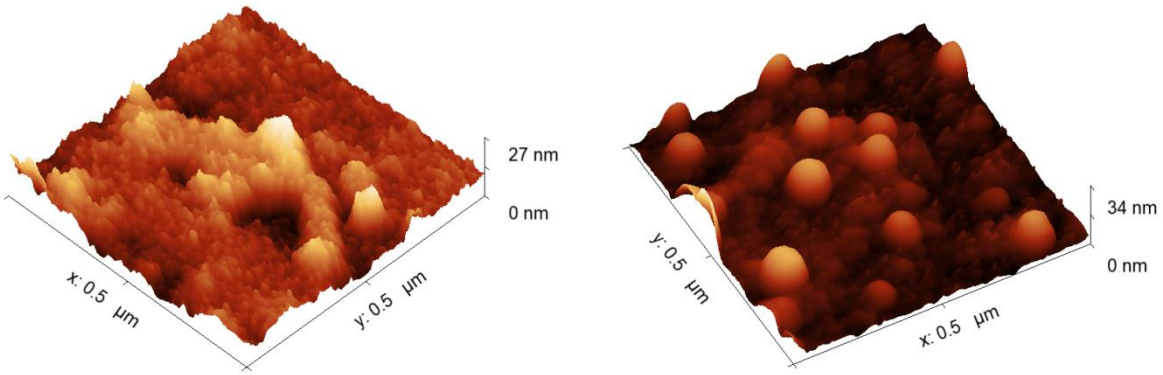

1st experiment 2nd experiment

Figure 3.35. AFM mages of Bi-Fe-O film on the surface of Kapton.

XPS allows us to suggest that in the second case, bismuth is less oxidized and self-organizing, agglomerating into metallic inclusions (Figure 3.36). The presence of more dangling oxygen bonds is greater in the second sample, which means larger amorphousness. This effect creates an excess of oxygen. A consequence of the excess oxygen in the second experiment is the broadening of the peak of iron. Also in the first case, the Fe3O4 and Bi2O3 phases are also formed on the surface of the sample. This is a more favorable combination for the subsequent formation of the bismuth ferrite phase, taking into account the evaporation of bismuth during heating and a decrease in oxygen concentration during annealing in vacuum.

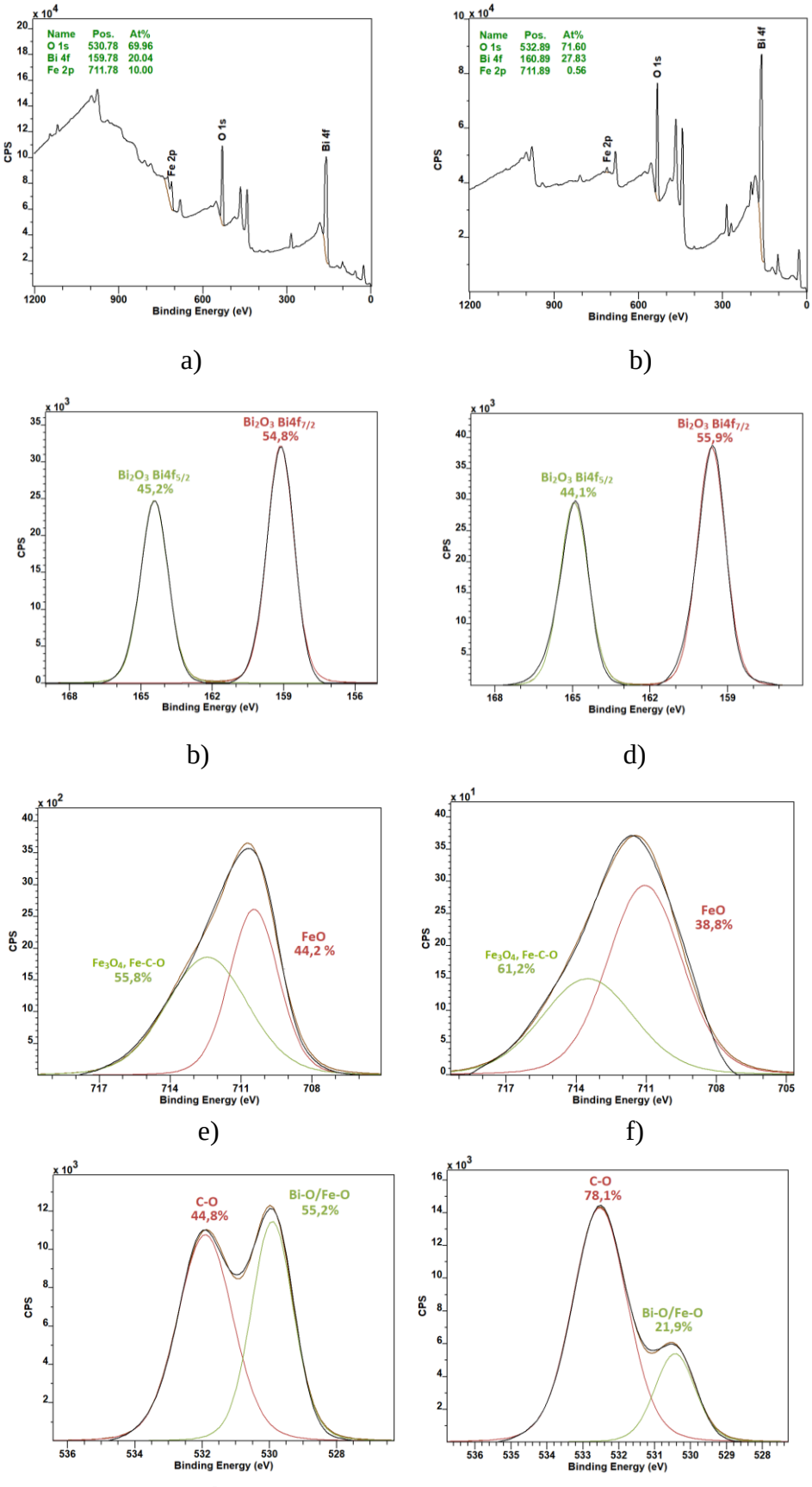

Figure 3.36. XPS of Bi-Fe-O film on the surface of Kapton: (a, c, e, h) 1st experiment and (b, d, f, i) 2nd experiment

Bismuth oxide exists in several polymorphes. They are α-Bi2O3 (monoclinic), β-Bi2O3 (tetragonal), γ-Bi2O3 (BCC), δ-Bi2O3 (Cubic), ε-Bi2O3 (triclinic). α-Bi2O3 dominated in the first sample. Width and intensity of Raman peaks (Fig.3.37) correspond to oxidation form of bismuth. It was also possible to observe the photoluminescence which is a consequence of partial self-organization as a result of laser irradiation and the presence of oxygen vacancies. As expected, it was higher in the first sample, but to compare the peaks, photoluminescence contribution was subtracted as a background.

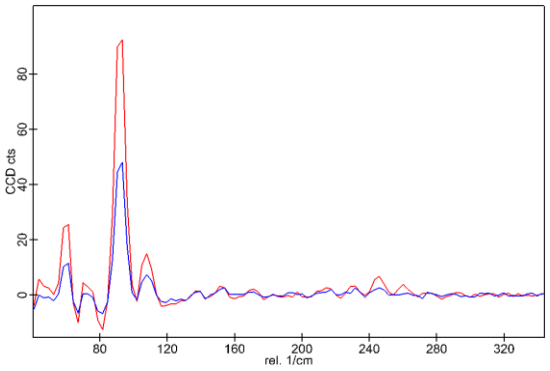

Figure 3.37. Raman of Bi-Fe-O film on the surface of Kapton: (red) 1st experiment and (blue) 2nd experiment.

The contribution to the film morphology is made by both the chemical composition of the substrate and its structure [160]–[163]. Kapton was chosen because of the possibility of its use after treatment in the field of terahertz radiation as an absorbent [164]. It is known that Kapton, like most polymers, can interact with atomic and ionized oxygen. The authors of [165] used silica films as a protective Kapton film that protects from degradation. In our case, the property of interaction with oxygen is a decisive factor in the formation of the film-substrate interface. The use of Kapton allows the study of mechanical deformations and film tension due to the flexibility of the substrate. Kapton has suitable chemical, mechanical, electrical, and temperature properties for use as active material substrates[166].
A higher content of iron and Fe-O bonds, as can be seen from CPS, is the result of a greater magnetization of the appearance of hysteresis at room temperature (Fig.3.38).

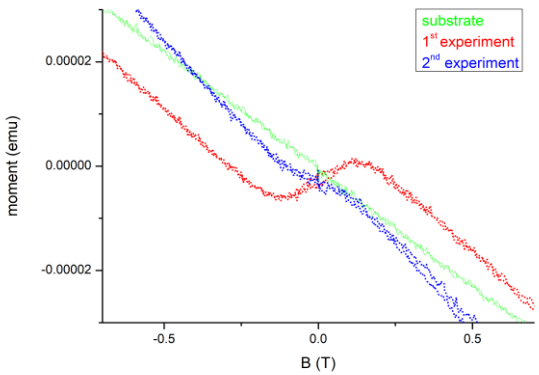

Figure 3.38. VSM of the Kapton substrate (green),
Bi-Fe-O/Kapton at first experiment (red), Bi-Fe-O/Kapton at second experiment (blue).

3.5. Pulsed Laser Deposition $BiFeO_3$ on Si-based substrates

Silicon technology is one of the most developed in the field of obtaining structures for electronics. The market offers a wide selection of monocrystalline silicon of different sizes, structures, and doping levels. Silicon oxidation and surface oxide stability should be taken into consideration. Due to the oxygen-containing atmosphere, the silicon surface is oxidized, forming a layer of about 1 nm. This layer begins to form when preparing the silicon substrate to be inserted into the deposition unit. This complicates the preparation of bismuth ferrite directly on the silicon surface. The deposition on silicon substrates was carried out after the deposition of a metal layer, due to the fact that silicon demonstrates chemical activity towards the growing perovskite structure and can be embedded in it, violating the structure and forming a wide transition zone. The growth of bismuth ferrite on substrates of single-crystal silicon is carried out using buffer layers. This prevents the possibility of chemical interaction and diffusion of silicon with the growing layer.

3.5.1. Preparation of BFO/Pt/SiO_2/Si

For deposition of the film by PLD method, the metallized silicon substrates were used. The wafers were purchased from MiroChemicals GmbH, 4 inch, thickness 525±25 μm, (100), 1-side polished, p-type (boron), 1-10 Ohm·cm. Platinum layer of 20 nm was deposited by magnetron sputtering on the substrates. PLD parameters: Spot size: 1.01x2.33 mm^2; Mask: 5.5x18 mm^2; Energy 22,7 mJ; Fluency: 1.08 J/mm^2; O_2 pressure: 0,1 mBar; Scanning diameter: 6,06x4,66 mm2; Pulses: 50 000; Scan speed: 0,7 mm/s; Temperature control is essential to provide bonding of the film and substrate and control films stoichiometry. Following temperatures was chosen substrate temperature 250 ^oC, Ramp 25 ^oC /min; Annealing 500 ^oC for 5 min at O_2 100 mBar

3.5.2. Characterizations

X-ray diffraction analysis shows the polycrystalline phase of bismuth ferrite with a predominant structure R3c (Fig.3.39a). The peak at 28° shows the bismuth oxide phase in the structure, presumably which was formed due to the predominance of bismuth over iron in the phase.

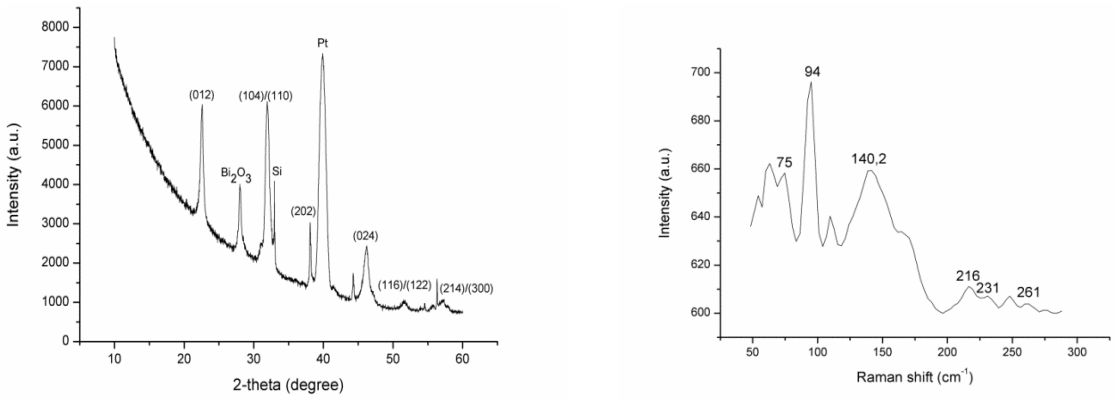

a) b)

Figure 3.39. Structural study of BFO/Pt/SiO_2/Si a) XRD spectra; b) Raman spectra.

Several Raman active modes in the shown spectral window are observed (Fig. 3.39b). The 140.2 cm^{-1} and 216 cm^{-1} are of A1 symmetry, and those at 75 cm^{-1}, 261 cm^{-1} belong to E symmetry and confirmed the rhombohedral structure. 231 indicates distorted rhombohedral-like (R-like) phase formed in the highly strained BFO thin film. The first principle calculation suggests that Bi atoms contribute low frequency modes below 167 cm^{-1}, Fe atoms mainly participate in the modes between 152 and 262 cm^{-1}, while for higher frequency modes above 262 cm^{-1}, modes from oxygen atoms dominate. The Raman band located at 94 cm^{-1} is assigned to lattice vibrations of β-Bi_2O_3 crystalline phase.

Piezoresponse force microscopy and AC-Magnetic force microscopy (Distance sample-probe for MFM 100 nm) was performed at room temperature (Fig. 3.40, 3.41).

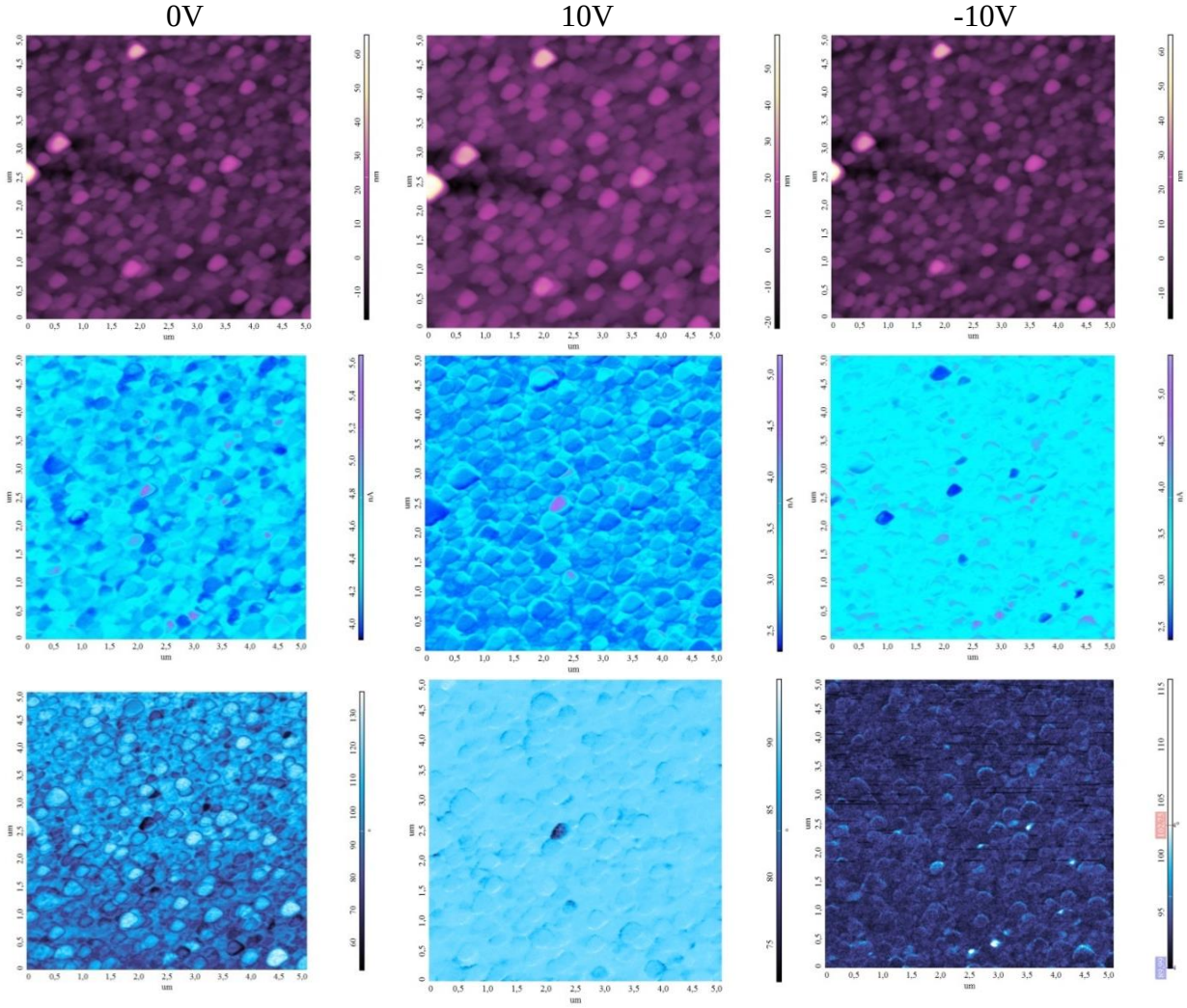

Figure 3.40. PFM of BFO/Pt/SiO_2/Si at 0, 10 and -10 V.

PFM analysis of the obtained films gives information on the polarization of domains and also their phase contrast depending on the voltage applied to the probe (0V, 10V, -10V). As can be seen from the figures, the domains are about 300-500 nm in size. Depending on the direction

of the applied voltage, the polarization and phase of some of the domains changes. This will allow creating a structure with films of bismuth ferrite with controlled electric polarization. When a voltage polarity is applied, the structure undergoes some lattice distortions.

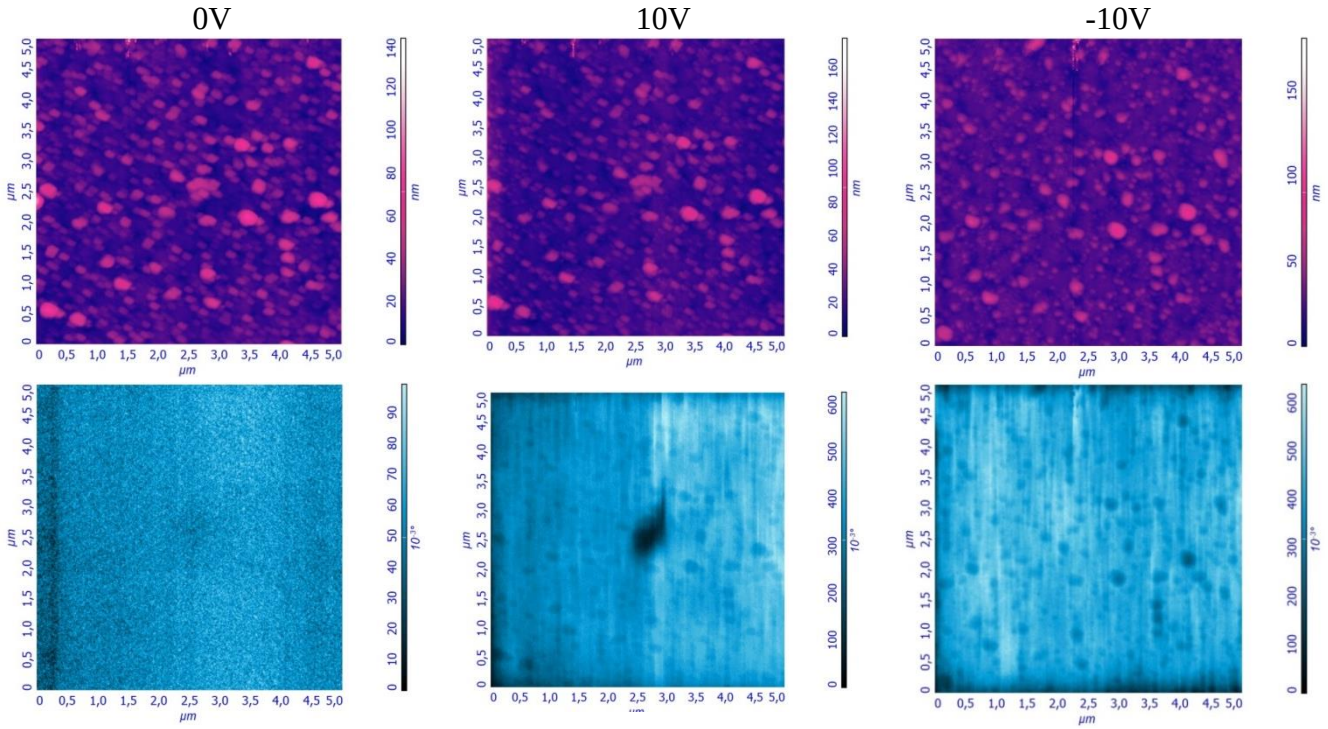

Figure 3.41. MFM of BFO/Pt/SiO_2/Si at 0, 10 and -10 V.

MFM measurements with a voltage supply (10V, -10V) of the obtained films give us information on the relationship of the electrical and magnetic subsystems in a bismuth ferrite film. As can be seen from the figures, when the polarity of the voltage changes, the magnetization of certain domains changes. Thus, the magnetic field can control the electrical properties of the resulting film.

Ar ion etching was applied four times with following parameters: 10keV Ar1000+, Raster size 3x3 mm, pre-etch and post-etch times 5 sec. Cluster beam etching is less destructive and, according to the carbon level, only the surface layers were etched (Fig. 3.42 and 4.43). Changes in the composition of iron and bismuth are associated with surface modification due to etching.

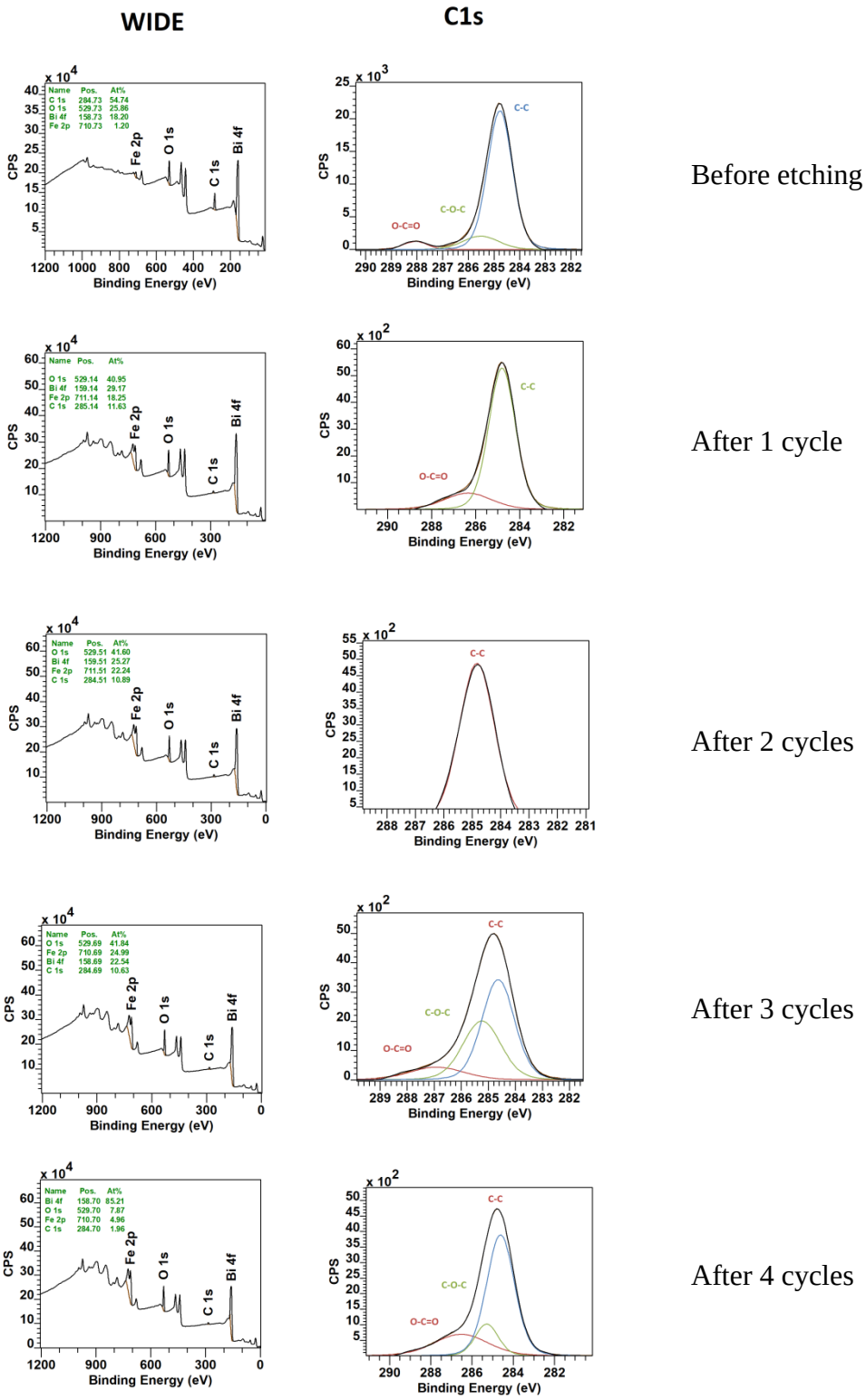

Figure 3.42. XPS wide and element (carbon) spectra of BFO/Pt/SiO_2/Si during depth profiling.

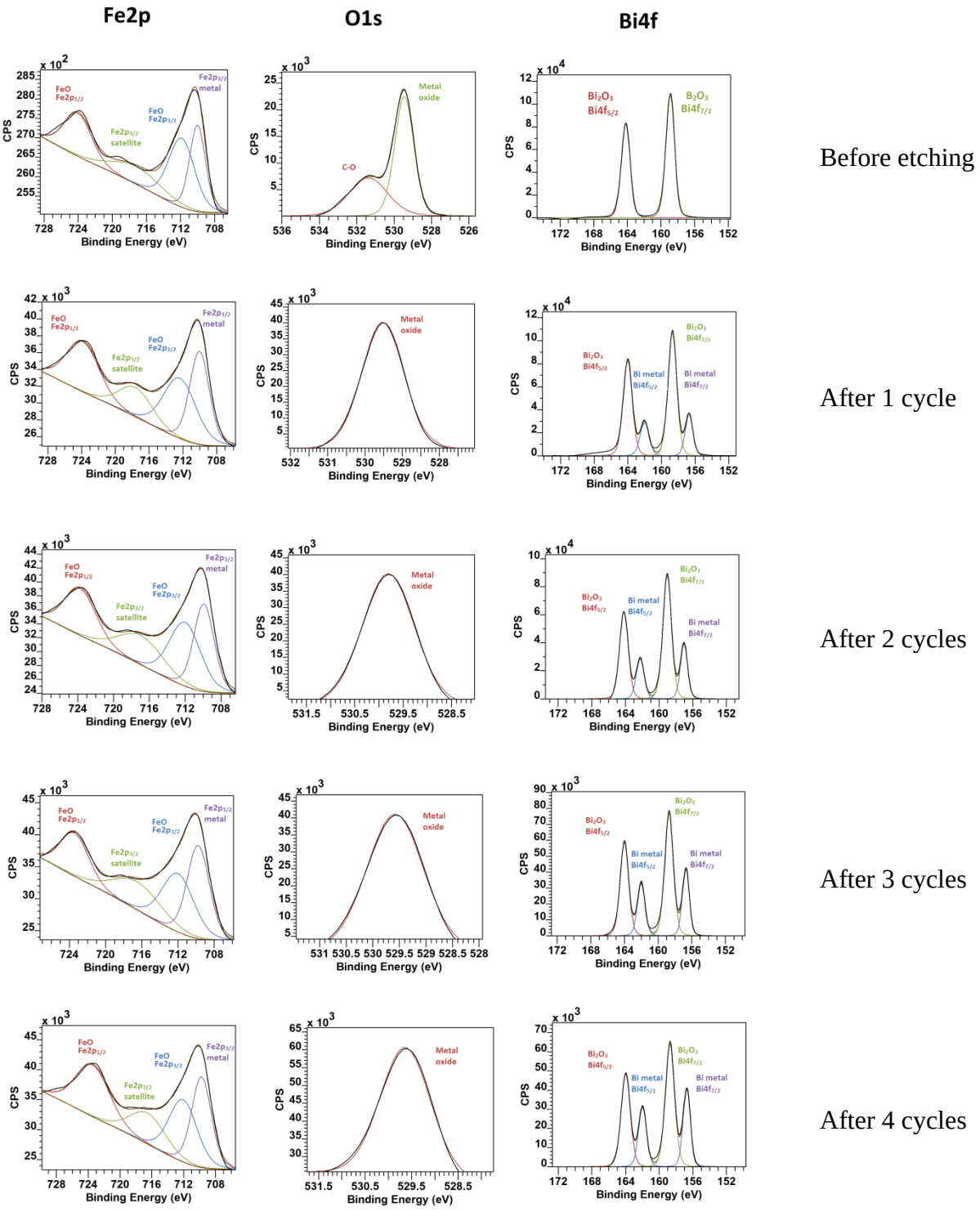

Figure 3.43. XPS element (iron, oxygen and bismuth) spectra of $BFO/Pt/SiO_2/Si$ during depth profiling.

Plasma modification of the surface makes it possible to create the desired properties in the surface region of the sample, as can be seen from the figures for changes in the Fe^{+3}/Fe^{+2}

ratio, it indicates the formation of oxygen vacancies, which allows changing of the electrical, magnetic, and optical properties of the obtained bismuth ferrite films. The predominance or excess in the phase of metallic bismuth is associated with this same feature. The longer the surface is etched, the more metallic bismuth is in the phase. Thus, by controlling the composition of the resulting target, it is possible to control the properties of the resulting films.

Measurement of the magnetization at room temperature showed results requiring additional studies (Fig.3.44). The substrate has a paramagnetic character with a small magnetization, probably due to the properties of the silicon substrate. Prior to etching, the film has magnetization as well as magnetic capacitance.

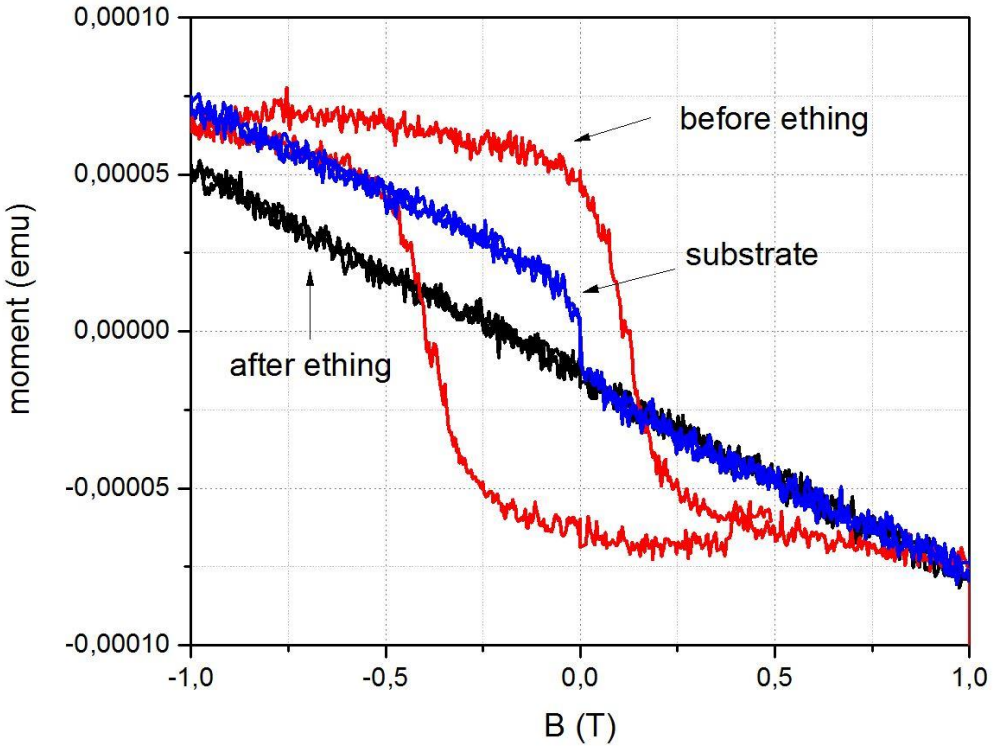

Figure 3.44. VSM of BFO/Pt/SiO_2/Si: pure /Pt/SiO_2/Si (blue); BFO/Pt/SiO_2/Si before etching (red); BFO/Pt/SiO_2/Si after etching (black).

The magnetic loop is asymmetric in nature, probably due to a defective structure or magnetization anisotropy. The most interesting thing is when the surface is etched, it completely transforms into a paramagnet with a shift to the negative magnetization region at low fields. These studies are fundamental and require the study of topological features occurring in the film when creating local changes in it.

3.5.3. Target degradation

Ceramic bismuth ferrite targets were prepared for (PLD) using the Spark Plasma Sintering (SPS) method based on synthesized powder. Analytically pure bismuth $Bi(NO_3)_3 \cdot 5H_2O$ and iron ($Fe(NO_3)_3 \cdot 9H_2O$ nitrates were taken according to stoichiometric ratio. Glycine played the role of fossil fuels, which provided a platform for redox reactions between the reactants during combustion. Metal nitrates are hygroscopic, and they tend to form a suspension mixture when mixed with glycine. The mixture was dehydrated by heating to 315°C. The dried mixture was then heated on a hot stove to initiate the combustion process. Since metal nitrates also play the role of oxidizing agents, the combustion process can occur efficiently using oxygen contained in the reagents themselves. As a result of the combustion process, voluminous ash was formed, and dense yellowish vapor was released. Then the product was carefully crushed in a mortar. Then heat treated at temperatures of 600 °C for an hour.

PLD is a process of rapid melting and evaporation of a target material as a result of exposure to high-energy laser radiation, followed by transfer of the sprayed material from the target to the substrate in vacuum and its deposition. The mechanism includes the ablation of the target material with laser irradiation, the development of a plasma torch containing high energy ions and electrons, as well as the crystal growth of the coating itself on the substrate. The PLD process as a whole can be divided into four stages:

1. interaction of laser radiation with the target - ablation of the target material and the creation of plasma;

2. plasma dynamics - its expansion;

3. applying the material to the substrate;

4. film growth on the surface of the substrate.

Each of these steps is critical to the physicomechanical and chemical parameters of the coating. The removal of atoms from the bulk of the material is carried out by evaporation of the mass of the substance to the surface. The initial emission of electrons and coating ions occurs, the evaporation process by its nature is most often thermal. The depth of penetration of laser radiation at this moment depends on the wavelength of the laser radiation and the refractive index of the target material, as well as the porosity and morphology of the target.

Due to the complex nature of such a process, it is impossible to calculate (simulate) it in advance. For example, during the evaporation process, the near-surface volume of the target undergoes significant modifications under certain conditions. And this affects the angular, mass, charge, and energy distribution of emitted particles, which, in turn, affects the mechanism and kinetics of the formation of condensate on the substrate. Therefore, studies aimed at establishing the relationship between the processes on the surface of the target and the growing film are relevant.

The stoichiometric composition, structure, and topography of the target used for PLD films of the $BiFeO_3$ multiferroic should be controlled before depositions process. A change in the stoichiometric composition can affects the composition and structure of the resulting films.

Given the fact that the PLD process uses an oxygen medium, the probability of the formation of additional oxygen bonds with the metals of iron and bismuth is highly probable.

The target was pre-polished with diamond powder, ~ 0.25 μmicrons in size. Further cleaning consisted of washing in an ultrasonic bath in C_3H_8O, then in ethanol and in demineralized water. The target was sputtered with a laser beam at the following parameters: Spot size: 2.85x0.82 mm^2, mask: 3x15 mm^2, energy 23,5 mJ, fluency: 1.093 J/mm^2,O_2 pressure: 0,1 mBar, scan speed: 0,7 mm/s, pre-ablation 10Hz, 1000 pulses for first experiment and 100000 for second experiment

To understand the mechanisms of degradation of the target surface during the PLD process, the target was studied using SEM Tescan Lyra 3 with an EDX Oxfords Instruments X-Max 50 detector and determined the qualitative and quantitative characteristics of the sample. SEM and EDX data (Fig. 3.45) show the effect of laser annealing of the target surface at pulses: 10 000 to compare the target surface before the experiment. The appearing surface features at 100 000 were similar.

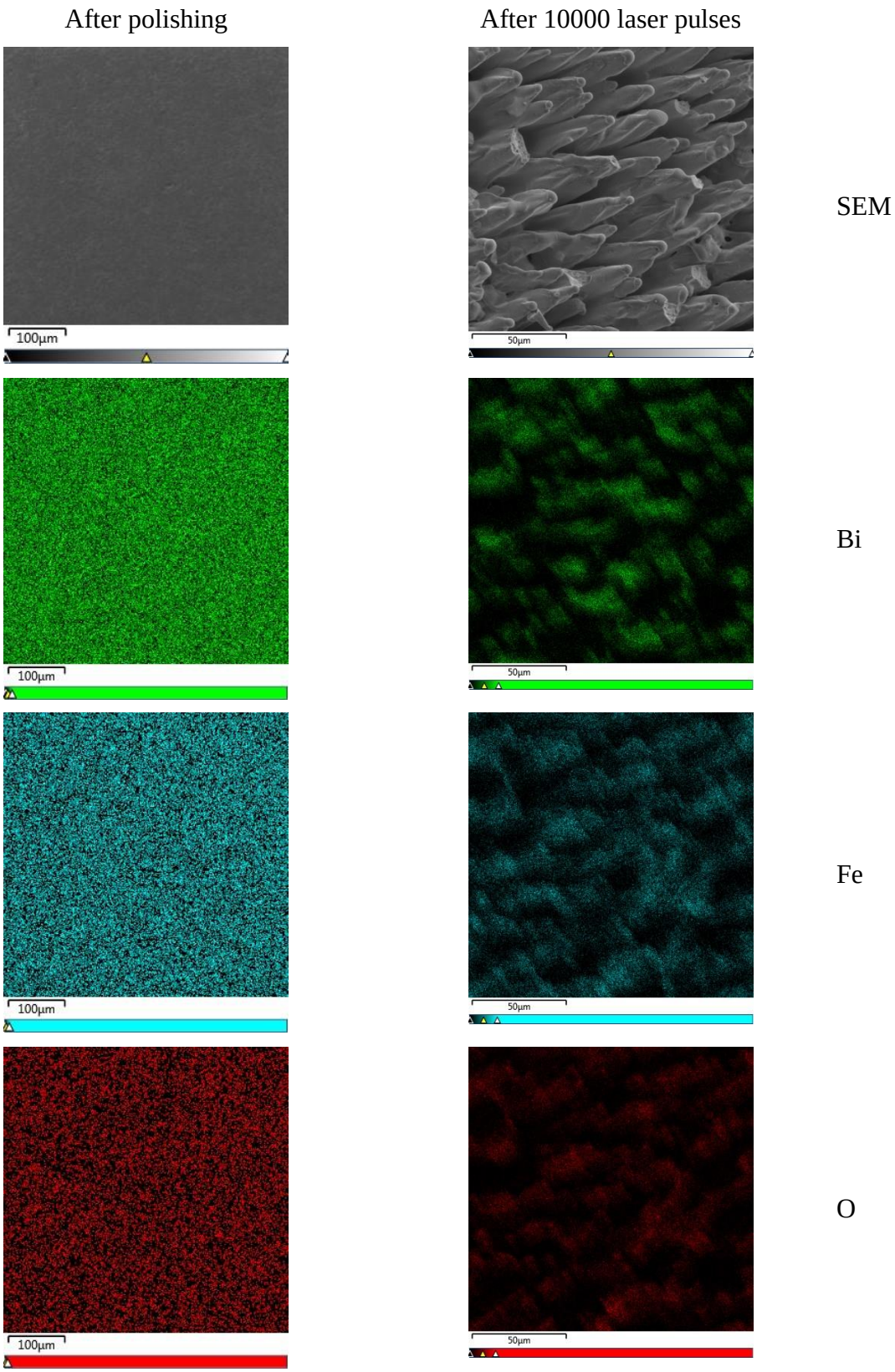

Figure 3.45. SEM-EDX analysis of the $BiFeO_3$ target before the process and after 10 000 laser pulses.

It is seen from SEM-EDX that the surface topography changes significantly, and a quantitative change in the composition of the surface region of the target occurs. Depending on the number of laser pulses during the evaporation process, the amount of bismuth is mainly affected (see table), which is relatively mobile in contrast to iron atoms (Table 1). Figure 3.46 shows how a laser beam acts on the surface of a ceramic target.

Table 1. EDX analysis of the $BiFeO_3$ target composition.

No ablation		**Pulses: 10 000**		**Pulses: 100 000**	
Atomic %		**Atomic %**		**Atomic %**	
O	41.45	O	44.2	O	47.0
Fe	12.35	Fe	23.9	Fe	25.1
Bi	12.30	Bi	6.4	Bi	6.0

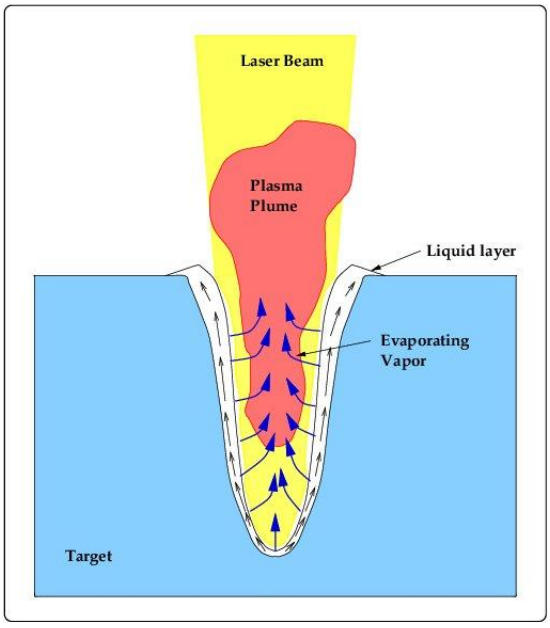

Figure 3.46. Schematic of laser-material interaction [167].

Thus, as can be seen from Figure 3.46, with laser radiation from the target, the beam practically melts the evaporation region and a liquid phase is created, which tends up the sides of the crater. The liquid phase creates elevations and forms a surface topography (Fig. 3.45). Since it is possible to control the amount of oxygen introduced into the chamber in the atmosphere of the evaporated substance, saturation or excess of oxygen vacancies in the resulting $BiFeO_3$ film is possible (the dependence of the oxygen vacancies in the composition of the obtained film on the pressure of the oxygen introduced into the chamber will be studied in further work). A parallel study of the target surface and the resulting film allows us to create the prerequisites for modeling the technological process for producing $BiFeO_3$ multiferroic films with desired properties. Changes in the phase and structural composition of the surface of the bismuth ferrite target were studied by XRD with brightness source Rigaku SmartLab 3kW.

Figure 3.47 shows the comparison of XRD spectra of $BiFeO_3$ target after ablation, the data are systemized in Table 2.

Table 2. Phase composition of target before and after 100 000 pulses.

	Before sputtering	**After 100 000 pulses**
Target phase	**Content (%)**	**Content (%)**
$BiFeO_3$	89.9	34.1
$Bi_2Fe_4O_9$	6.8	49.4
$Bi_{25}FeO_{40}$	3.3	16.5

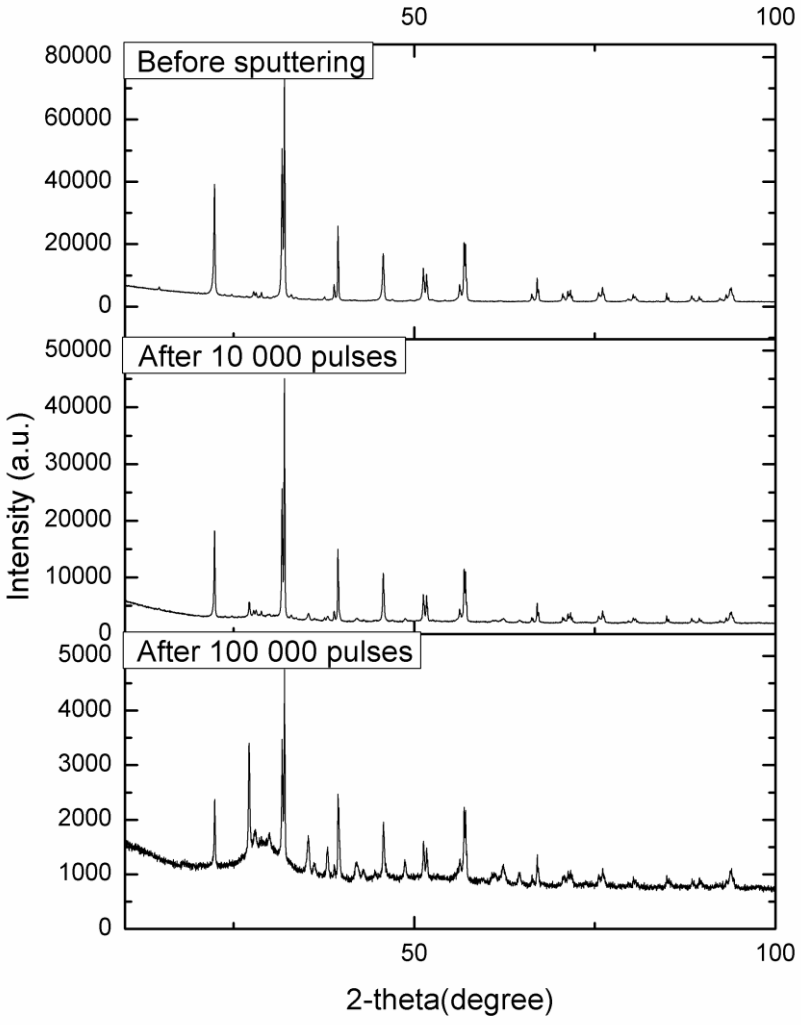

Figure 3.47. XRD of the $BiFeO_3$ target before and after ablation.

From the XRD data, it follows that the ratio of the phase composition of the surface region of the target varies (see table). Due to changes in the morphology of the target surface in the PLD process, due to thermal processes, the number of non-$BiFeO_3$ phases increases several

times. Obviously, this is due to the technological features of this process: oxygen atmosphere, thermal modification of the target surface, evaporation of elements or agglomerates from the target surface, quantitative ratios of elements in the laser-modified target surface, structural changes, etc. As the laser acts on the target, the crystal lattice structure of the near-surface region of the target changes; the selinite phase, $Bi_2Fe_4O_9$, grows to a greater extent (Fig. 3.48).

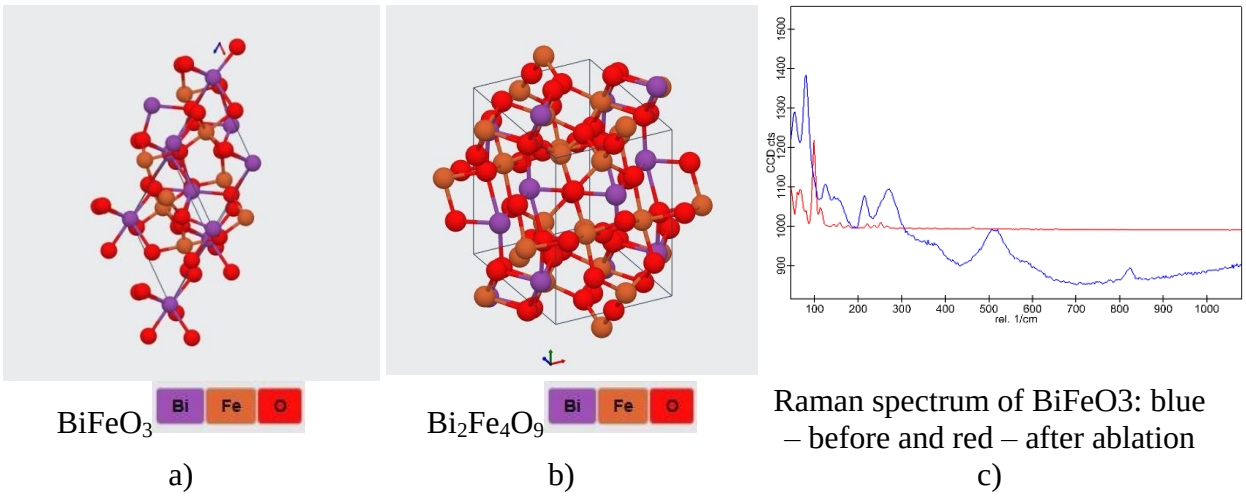

$BiFeO_3$ a)

$Bi_2Fe_4O_9$ b)

Raman spectrum of BiFeO3: blue – before and red – after ablation c)

Figure 3.48. Structure of a) $BiFeO_3$, b) $Bi_2Fe_4O_9$ and c) Raman spectra of target before and after 100 000 abblation pulses.

To study the structural properties of the target, Raman spectroscopy studies were additionally carried out. Raman spectra were excited by polarized radiation (Z (YX) $\bar{}$Z) of a solid-state laser (λ = 532.0 nm), the diameter of the focused beam was 2 μm. Figure 3.48c shows the Raman spectrum of the BiFeO3 target along with the main peaks.

Peaks positions (139 cm-1, 172 cm-1, 219 cm-1, 264 cm-1, 265 cm-1, 364 cm-1, 440 cm-1, 480 cm-1, 525 cm-1, 618 cm-1) from the $BiFeO_3$ target coincides with literature data [168]. Being more sensitive to surface, Raman spectra of sputtered target demonstrate presence of bismuth oxidation on the surface.

4. SUMMARY AND OBJECTIVES OF FUTHER WORK

This study benefits the enhancement of existing sensing technology by using new design based on physical principles of low-dimension multifunctional materials. Further in-depth studies are needed to provide reliable application and spreading of multiferroics in electronics.

Continuation of this work supposes optimization of ALD and PLD technological parameters preparation of bismuth ferrite films. The topic of the most optimal precursors and substrate material (including substrate orientation) to obtain high-quality bismuth ferrite is still in the center of interest. Study of Bi-Fe-O/substrate interface should be done in combination with quantum-chemical calculations of multistage chemical reactions in the ALD system and solid-state reaction at PLD system for obtaining theoretical results on formation of bismuth ferrite films. Several problems should be solved, such as: Piezoelectric domain size should be evaluated in dependence on the physical dimensions of the films using Landau, Lifshitz, and Kittel's (LLK) scaling law.

The further work will be aimed at solving several interrelated tasks that are important steps towards the final goal - the creation of adaptive functional nanostructures that provide the ability to control spin polarization in thin films of multiferroics under mechanical, electrical and magnetic effects. Specifically, it concerns the developing of memristive devices with the ability to control the absolute values of the SET/RESET voltage in a magnetic field and magnetization in the absence of a magnetic field and double-layer ferrite-piezoelectric structure for generation of terahertz signal.

Understanding of the physical processes at the subatomic level as well as mechanisms of interaction between optical, electrical, magnetic and mechanical subsystems could be expanded upon using such materials as superconductor and piezo substrates.

4.1. Combination with superconductor materials

Worthy of note is that the interaction between a ferromagnet and a superconductor gives rise to new phenomena that are absent in individual components. Experiments on these structures were recently performed [169] and they confirmed the relevance of the study of new properties arising in the border region of the structure $BiFeO_3$/superconductor. Superconductivity and ferromagnetism are two types of ordering that usually contradict each other: while traditional singlet superconductors exist due to the formation of Cooper pairs of electrons with opposite spins, the ferromagnetic order implies the same direction of electron spins. Therefore, the coexistence region of these two types of ordering is rather narrow [170] and several studies [171], [172] showed that inhomogeneous (modulated) superconducting phases can exist. For these experiments YBCO is planned to be conducted in collaboration with Dagestan State University. I studied the provided YBCO targets for phase and chemical purity, as well as their reaction to sputtering. XRD confirmed the presence of Pmmm SpaceGroup and orthorombic crystal system even after sputtering by cluster ion source 10keVAr500+ three times during 600 sec, 3mmx3mm area. Changing of chemical compositions after third etching is shown by XPS (Fig. 4.1). The broken oxygen bonds caused

changing of stoichiometry, which will be adjusted by parameters of ablation of this target during deposition.

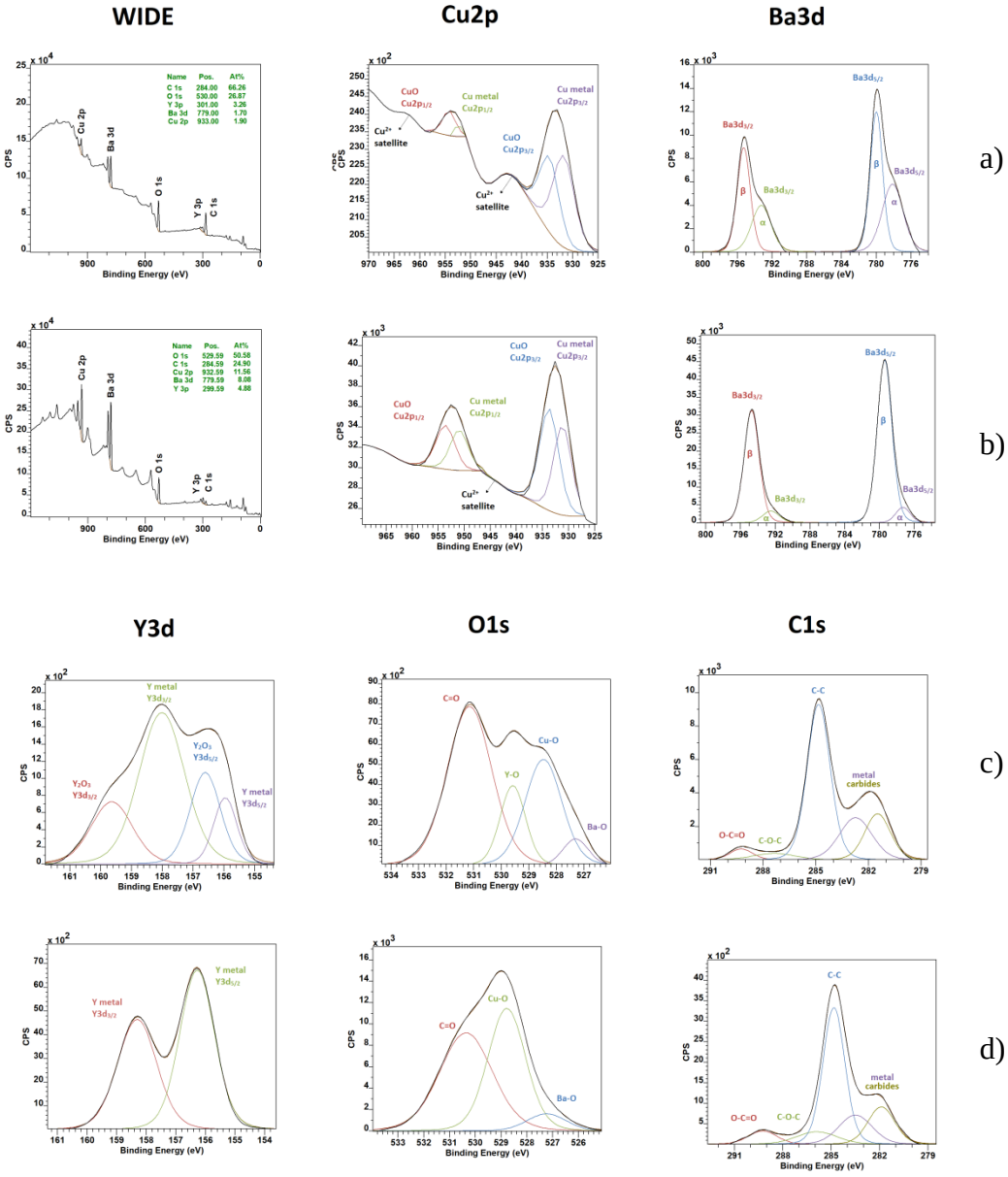

Figure 4.1. XPS spectra of the YBCO polycrystalline target a,c) before and b,d) after sputtering.

4.2. Preliminary results on for AlN/$BiFeO_3$ structures

The research will include further preparation and characterization of functional nanostructures on the basis of TiO_2 nanotubes and piezoelectric AlN. First structure is interesting for architecture of RRAM on the basis of $BiFeO_3$/Nt-TiO_2/Ti with definition of SET/RESET voltage in case of presence and without a magnetic field. Second, architecture for generation

of terahertz signal on the basis of $BiFeO_3$/AlN/substrate with determination of conditions and parameters for THz signal generation (Fig.4.2). Fundamental research of mechanisms underlying the functionality of the structures is an integral part of the work in the future. Appendix 4 contains patent obtained in the field of AlN layers preparation.

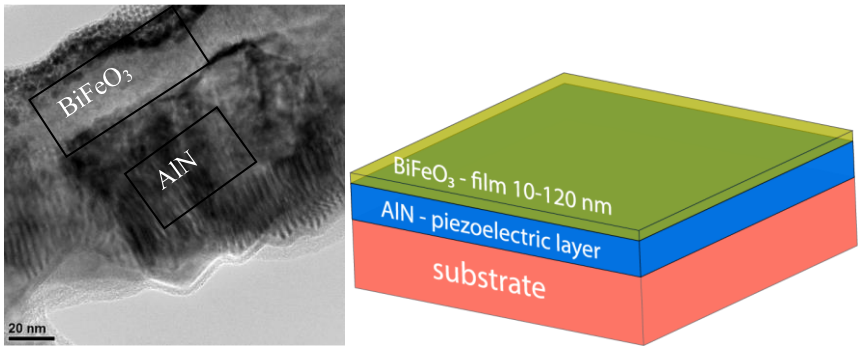

Figure 4.2. Suggested design of structure for generation of terahertz signal.

5. CONTRIBUTION TO APPLIED AND FUNDAMENTAL SCIENCE

The development of a scientific direction focused on the synthesis of multiferroics with given physical properties will make it possible to take a significant step forward in many areas of technology: ordered micro and nanostructures based on active materials, multilayer coatings for special purposes, etc.

The most promising devices are based on magnetic and electrical properties of semiconductor materials, including magnetic recording in magnetoresistive random access memory (MRAM) and RRAM in memristive devices. In these devices, the spin and the charge of electrons are used separately. For example, with magnetic recording, a magnetic field is used to record or read information stored by magnetization. The search for methods to achieve a higher data density during information storage actualizes studies on the manipulation of resistive switching parameters using a magnetic field and magnetization without a field, within the framework of a new paradigm in which spin and charge interact with each other. This, ultimately, will enable performance of fast operations with low energy costs during recording, transmission, processing and reading information. Research in the field of terahertz radiation is one of the promising directions in modern physics. This spectral range, which has not been used for a long time, has attracted the attention of physicists, chemists, biologists, and engineers in recent years. One of the most important areas of research in this range is the acquisition of images, both in reflected light and in radioscopy systems. This is due to the fact that many materials that are opaque in the visible range are partially transparent in the terahertz range. The scientific significance is of the indicated problem lies in contribution to the understanding of the nature and mechanism of resistive switching in MIM (metal-insulator-metal) structures for optimizing cell parameters when developing non-volatile RRAM memory. Achieving a short switching time (less than 10 nanoseconds), in combination with a relatively low operating voltage (less than 5-7 volts), in memristive devices will bring us closer to the synapse simulation in biological systems. To develop sensitive detectors and sources in the terahertz spectral region, it is necessary to understand the nature of the crystal lattice phonons influence on the spin polarization of an individual electron and the propagation of a spin wave in the active nanoscale multiferroics (spin-phonon interaction).

The use of hybrid substrates leads to the appearance of artificial defects. The development of promising materials leads to the miniaturization of electronic devices through the use of the principles of quantum mechanics. Structures oriented to use in the terahertz range allow the study of materials containing hydrogen and van der Waals bonds. This range is interesting for the different types of vibrational spectroscopy in the field of materials science, electronics and medicine. The study of nanoscale structures, in contrast to bulk materials, contributes to a deeper understanding of the fundamental laws and processes responsible for piezoelectric, electro- and magnetic ordering.

6. CONTRIBUTION TO PEDAGOGICAL WORK

The issues and experience obtained during this work were implemented to laboratory course of Nanotechnology subject for master students. Some recommendations are summarized and published (Appendix 5).

References

[1] N. A. Hill, “Why are there so few magnetic ferroelectrics?,” *J. Phys. Chem. B*, 2000.

[2] J. F. Scott and R. Blinc, “Multiferroic magnetoelectric fluorides: Why are there so many magnetic ferroelectrics?,” *Journal of Physics Condensed Matter*. 2011.

[3] L. E. Fuentes-Cobas, J. A. Matutes-Aquino, M. E. Botello-Zubiate, A. González-Vázquez, M. E. Fuentes-Montero, and D. Chateigner, “Advances in Magnetoelectric Materials and Their Application,” *Handb. Magn. Mater.*, 2015.

[4] I. Szafraniak-Wiza, B. Andrzejewski, and B. Hilczerb, “Magnetic properties of bismuth ferrite nanopowder obtained by mechanochemical synthesis,” in *Proceedings of the 8th International Conference on Mechanochemistry and Mechanical Alloying, INCOME 2014*, 2014.

[5] A. F. Popkov, M. D. Davydova, K. A. Zvezdin, S. V. Solov’Yov, and A. K. Zvezdin, “Origin of the giant linear magnetoelectric effect in perovskitelike multiferroic BiFeO3,” *Phys. Rev. B*, 2016.

[6] B. Hilczer, R. Pankiewicz, A. Pietraszko, P. Cieluch, F. Matelski, and B. Andrzejewski, “Synthesis and Properties of Bismuth Ferrite Multiferroic Nanoflowers,” *J. Mater. Sci.*, 2014.

[7] L. O. Chua, “Memristor—The Missing Circuit Element,” *IEEE Trans. Circuit Theory*, vol. 18, no. 5, pp. 507–519, 1971.

[8] J. M. Tour and T. He, “Electronics: The fourth element,” *Nature*, vol. 453, no. 7191. pp. 42–43, 2008.

[9] L. Chua, “Resistance switching memories are memristors,” *Appl. Phys. A Mater. Sci. Process.*, vol. 102, no. 4, pp. 765–783, 2011.

[10] R. Waser and M. Aono, “Nanoionics-based resistive switching memories,” *Nanosci. Technol. A Collect. Rev. from Nat. Journals*, pp. 158–165, 2009.

[11] A. Sawa, “Resistive switching in rapid advances in information technology rely on high-speed and large-capacity nonvolatile memories,” *Mater. Today*, vol. 11, no. 6, pp. 28–36, 2008.

[12] J. J. Yang, M. D. Pickett, X. Li, D. A. A. Ohlberg, D. R. Stewart, and R. S. Williams, “Memristive switching mechanism for metal/oxide/metal nanodevices,” *Nat. Nanotechnol.*, vol. 3, no. 7, pp. 429–433, 2008.

[13] M. Ungureanu *et al.*, “A light-controlled resistive switching memory,” *Adv. Mater.*, vol. 24, no. 18, pp. 2496–2500, 2012.

[14] B. Sun, Y. Liu, W. Zhao, J. Wu, and P. Chen, “Hydrothermal preparation and white-light-controlled resistive switching behavior of BaWO 4 Nanospheres,” *Nano-Micro Lett.*, vol. 7, no. 1, pp. 80–85, 2014.

[15] J. Park, S. Lee, and K. Yong, “Photo-stimulated resistive switching of ZnO nanorods,” *Nanotechnology*, vol. 23, no. 38, 2012.

[16] G. Chen, J. J. Peng, C. Song, F. Zeng, and F. Pan, “Interplay between chemical state, electric properties, and ferromagnetism in Fe-doped ZnO films,” *J. Appl. Phys.*, vol. 113, no. 10, 2013.

[17] T. Gao *et al.*, “Electric-Field Induced Reversible Switching of the Magnetic Easy Axis

in Co/BiFeO3 on SrTiO3," *Nano Lett.*, vol. 17, no. 5, pp. 2825–2832, 2017.

[18] G. Chen, C. Song, C. Chen, S. Gao, F. Zeng, and F. Pan, "Resistive switching and magnetic modulation in cobalt-doped ZnO," *Adv. Mater.*, vol. 24, no. 26, pp. 3515–3520, 2012.

[19] T. Dietl, "A ten-year perspective on dilute magnetic semiconductors and oxides," *Nature Materials*, vol. 9, no. 12. pp. 965–974, 2010.

[20] H. Ohno *et al.*, "Electric-field control of ferromagnetism," *Nature*, vol. 408, no. 6815, pp. 944–946, 2000.

[21] I. Stolichnov *et al.*, "Non-volatile ferroelectric control of ferromagnetism in (Ga,Mn)As," *Nat. Mater.*, vol. 7, no. 6, pp. 464–467, 2008.

[22] D. Chiba, M. Sawicki, Y. Nishitani, Y. Nakatani, F. Matsukura, and H. Ohno, "Magnetization vector manipulation by electric fields," *Nature*, vol. 455, no. 7212, pp. 515–518, 2008.

[23] Y. Yamada *et al.*, "Electrically induced ferromagnetism at room temperature in cobalt-doped titanium dioxide," *Science (80-.).*, vol. 332, no. 6033, pp. 1065–1067, 2011.

[24] X. Cai *et al.*, "Sensitive room-temperature terahertz detection via the photothermoelectric effect in graphene," *Nat. Nanotechnol.*, vol. 9, no. 10, pp. 814–819, 2014.

[25] S. S. Abukari, S. Y. Mensah, N. G. Mensah, K. A. Adu, M. Rabiu, and A. Twum, "High frequency conductivity in carbon nanotubes," *AIP Adv.*, vol. 2, no. 4, 2012.

[26] X. He *et al.*, "Carbon nanotube terahertz detector," *Nano Lett.*, vol. 14, no. 7, pp. 3953–3958, 2014.

[27] A. Kadigrobov, R. I. Shekhter, and M. Jonson, "Novel laser based on magnetic tunneling," *Low Temp. Phys.*, vol. 31, no. 3, pp. 352–357, 2005.

[28] A. Kadigrobov, Z. Ivanov, T. Claeson, R. I. Shekhter, and M. Jonson, "Giant lasing effect in magnetic nanoconductors," *Europhys. Lett.*, vol. 67, no. 6, pp. 948–954, 2004.

[29] S. G. Chigarev *et al.*, "Spin-injection terahertz radiation in magnetic junctions," *Solid State Phenom.*, vol. 190, pp. 153–156, 2012.

[30] Y. V. Gulyaev, E. A. Vilkov, P. E. Zilberman, and A. I. Panas, "sd-Exchange electron spin resonance in a ferromagnetic metal," *JETP Lett.*, vol. 100, no. 3, pp. 174–176, 2014.

[31] "Scientists explain how the giant magnetoelectric effect occurs in bismuth ferrite," 2016. [Online]. Available: https://www.nanowerk.com. [Accessed: 10-Feb-2020].

[32] A. Perejón, E. Gil-González, P. E. Sánchez-Jiménez, A. R. West, and L. A. Pérez-Maqueda, "Electrical properties of bismuth ferrites: Bi2Fe4O9 and Bi25FeO39," *J. Eur. Ceram. Soc.*, 2019.

[33] T. Fujii, M. Takano, R. Katano, Y. Bando, Y. Isozumi, and T. Okuda, "Conversion electron Mössbauer spectroscopy of a single crystalline $B_{i3}Fe_5O_{12}$ film," *J. Magn. Magn. Mater.*, 1990.

[34] R. Qian-Jing and Z. Wei-De, "Tunable morphology of $Bi_2Fe_4O_9$ crystals for photocatalytic oxidation," *J. Phys. Chem. C*, 2009.

[35] Y. Wang *et al.*, "$Bi_2Fe_4O_9$ thin films as novel visible-light-active photoanodes for solar

water splitting," *J. Mater. Chem. A*, 2019.

[36] H. Yang, J. Dai, L. Wang, Y. Lin, F. Wang, and P. Kang, "A novel approach to prepare $Bi_2Fe_4O_9$ flower-like spheres with enhanced photocatalytic performance," *Sci. Rep.*, 2017.

[37] F. E. N. Ramirez, E. E. Espinosa, L. S. Pedroza, and J. A. Souza, "Humidity sensing effect in $Bi_{25}FeO_{39}$ sillenite-like compound," *J. Mater. Sci.*, 2016.

[38] S. S. Flores Morales, J. A. León Flores, J. L. Pérez Mazariego, V. Marquina Fábrega, and R. W. Gómez González, "Synthesis of Bi25FeO39 by molten salts method and its mössbauer spectrum," *Phys. B Condens. Matter*, 2017.

[39] J. Li and W. Chen, "Synthesis and Characterization of Bi-Fe-O Amorphous Nanoparticles for Photocatalysis by Sol-Gel Method," *Integr. Ferroelectr.*, 2019.

[40] K. Suzuki, H. Onodera, M. Sakurai, S. Masuda, A. Matsumoto, and H. Sadamura, "STRUCTURE AND MAGNETIC PROPERTIES OF Bi-Zn-Fe-O AMORPHOUS FILMS.," *IEEE Trans. Magn.*, 1986.

[41] M. Krnel *et al.*, "Speromagnetism and asperomagnetism as the ground states of the Tb-Dy-Ho-Er-Tm 'ideal' high-entropy alloy," *Intermetallics*, 2020.

[42] T. E. Quickel, L. T. Schelhas, R. A. Farrell, N. Petkov, V. H. Le, and S. H. Tolbert, "Mesoporous bismuth ferrite with amplified magnetoelectric coupling and electric field-induced ferrimagnetism," *Nat. Commun.*, 2015.

[43] A. R. Akbashev, G. Chen, and J. E. Spanier, "A facile route for producing single-crystalline epitaxial perovskite oxide thin films," *Nano Lett.*, vol. 14, no. 1, pp. 44–49, 2014.

[44] A. Singh and J. Chen, "Large vertical hysteretic shift and signature of exchange bias in $BiFeO_3/SrRuO_3$ heterostructure," *Ceram. Int.*, 2019.

[45] H. Liu, P. Yang, K. Yao, and J. Wang, "Growth rate induced monoclinic to tetragonal phase transition in epitaxial $BiFeO_3$ (001) thin films," *Appl. Phys. Lett.*, 2011.

[46] W. Dong, Y. Guo, B. Guo, H. Liu, H. Li, and H. Liu, "Photovoltaic properties of BiFeO3 thin film capacitors by using Al-doped zinc oxide as top electrode," *Mater. Lett.*, 2013.

[47] Z. Chen *et al.*, "Polarization tunable and enhanced photovoltaic properties in tetragonal-like $BiFeO_3$ epitaxial films with graphene top electrode," *J. Alloys Compd.*, 2019.

[48] Y. H. Chu *et al.*, "Ferroelectric size effects in multiferroic BiFeO3 thin films," *Appl. Phys. Lett.*, vol. 90, no. 25, 2007.

[49] K. Sone, H. Naganuma, M. Ito, T. Miyazaki, T. Nakajima, and S. Okamura, "100-nm-sized magnetic domain reversal by the magneto-electric effect in self-assembled $BiFeO_3/CoFe_2O_4$ bilayer films," *Sci. Rep.*, vol. 5, 2015.

[50] K. P. Gaikovich, B. A. Gribkov, V. L. Mironov, S. A. Treskov, and A. V. Zhilin, "Image retrieval in scanning probe microscopy taking into account the probe-surface interaction non-locality," in *Physics of Low-Dimensional Structures*, 2002.

[51] C. C. Glover, J. P. Killgore, and R. C. Tung, "Scanning speed phenomenon in contact-resonance atomic force microscopy," *Beilstein J. Nanotechnol.*, 2018.

[52] P. Schmuki, "Self-Organized TiO_2 Nanotube Arrays: Latest Features and

Applications," *Meet. Abstr.*, 2016.

[53] C. Di Valentin *et al.*, "N-doped TiO_2: Theory and experiment," *Chem. Phys.*, 2007.

[54] Z. Liu *et al.*, "Highly ordered TiO_2 nanotube arrays with controllable length for photoelectrocatalytic degradation of phenol," *J. Phys. Chem. C*, 2008.

[55] Y. Zhou *et al.*, "Monolayered Bi2WO6 nanosheets mimicking heterojunction interface with open surfaces for photocatalysis," *Nat. Commun.*, 2015.

[56] H. Asadi-Saghandi, A. Sheikhi, and R. Sotudeh-Gharebagh, "Sequence-based Process Modeling of Fluidized Bed Biomass Gasification[1] H. Asadi-Saghandi, A. Sheikhi, R. Sotudeh-Gharebagh, ACS Sustain. Chem. Eng. 3 (2015) 2640–2651.," *ACS Sustain. Chem. Eng.*, 2015.

[57] S. Sood, S. Kumar, A. Umar, A. Kaur, S. K. Mehta, and S. K. Kansal, "TiO_2 quantum dots for the photocatalytic degradation of indigo carmine dye," *J. Alloys Compd.*, 2015.

[58] X. Chen and S. S. Mao, "Titanium dioxide nanomaterials: Synthesis, properties, modifications and applications," *Chemical Reviews*. 2007.

[59] K. S. Raja, T. Gandhi, and M. Misra, "Effect of water content of ethylene glycol as electrolyte for synthesis of ordered titania nanotubes," *Electrochem. commun.*, 2007.

[60] F. Warken, A. Rauschenbeutel, and T. Bartholomäus, "Fiber pulling profits from precise positioning," *Photonics Spectra*, 2008.

[61] C. D. Lu, L. S. Chang, Y. F. Lu, and F. H. Lu, "The growth of interfacial compounds between titanium dioxide and bismuth oxide," *Ceram. Int.*, 2009.

[62] L. Giorgi *et al.*, "Electrochemical synthesis of self-organized TiO_2 crystalline nanotubes without annealing," *Nanotechnology*, 2018.

[63] Y. L. Du, G. Chen, and M. S. Zhang, "Grain size effects in $Bi_4Ti_3O_{12}$ nanocrystals investigated by Raman spectroscopy," *Solid State Commun.*, 2004.

[64] M. D. C. Rodríguez Aranda, Á. G. Rodríguez-Vázquez, U. Salazar-Kuri, M. E. Mendoza, and H. R. Navarro-Contreras, "Raman effect in multiferroic $Bi_5Fe_xTi_{3-x}O_{15}$ solid solutions: A temperature study," *J. Appl. Phys.*, 2018.

[65] S. H. Baek, S. Choi, T. L. Kim, and H. W. Jang, "Domain engineering in $BiFeO_3$ thin films," *Current Applied Physics*, vol. 17, no. 5. pp. 688–703, 2017.

[66] R. Guo *et al.*, "Non-volatile memory based on the ferroelectric," *Nat. Commun.*, vol. 4, 2013.

[67] J. M. Vila-Fungueiriño *et al.*, "Direct and converse piezoelectric responses at the nanoscale from epitaxial $BiFeO_3$ thin films grown by polymer assisted deposition," *Nanoscale*, vol. 10, no. 43, pp. 20155–20161, 2018.

[68] C. Huang and L. Chen, "Effects of interfaces on the structure and novel physical properties in epitaxial multiferroic $BiFeO_3$ ultrathin films," *Materials*, vol. 7, no. 7. pp. 5403–5426, 2014.

[69] J. J. Steffes, R. A. Ristau, R. Ramesh, and B. D. Huey, "Thickness scaling of ferroelectricity in $BiFeO_3$ by tomographic atomic force microscopy," *Proc. Natl. Acad. Sci. U. S. A.*, vol. 116, no. 7, pp. 2413–2418, 2019.

[70] M. Graf, M. Sepliarsky, R. Machado, and M. G. Stachiotti, "Dielectric and piezoelectric properties of $BiFeO_3$ from molecular dynamics simulations," *Solid State*

Commun., vol. 218, pp. 10–13, 2015.

[71] J. H. Jeon *et al.*, "Selector-free resistive switching memory cell based on $BiFeO_3$ nano-island showing high resistance ratio and nonlinearity factor," *Sci. Rep.*, vol. 6, 2016.

[72] A. Q. Jiang and Y. Zhang, "Next-generation ferroelectric domain-wall memories: principle and architecture," *NPG Asia Materials*, vol. 11, no. 1. 2019.

[73] H. Shima, H. Naganuma, and S. Okamur, "Optical Properties of Multiferroic $BiFeO_3$ Films," in *Materials Science - Advanced Topics*, 2013.

[74] M. Zhu, Z. Du, Q. Liu, B. Chen, S. H. Tsang, and E. H. T. Teo, "Ferroelectric $BiFeO_3$ thin-film optical modulators," *Appl. Phys. Lett.*, vol. 108, no. 23, 2016.

[75] Y. De Liou *et al.*, "Deterministic optical control of room temperature multiferroicity in $BiFeO_3$ thin films," *Nat. Mater.*, vol. 18, no. 6, pp. 580–587, 2019.

[76] R. V. Pisarev, A. S. Moskvin, A. M. Kalashnikova, and T. Rasing, "Charge transfer transitions in multiferroic $BiFeO_3$ and related ferrite insulators," *Phys. Rev. B - Condens. Matter Mater. Phys.*, vol. 79, no. 23, 2009.

[77] J. Ma *et al.*, "Giant energy density and high efficiency achieved in bismuth ferrite-based film capacitors via domain engineering," *Nat. Commun.*, vol. 9, no. 1, 2018.

[78] Z. Qiao *et al.*, "Quantum anomalous Hall effect in graphene proximity coupled to an antiferromagnetic insulator," *Phys. Rev. Lett.*, vol. 112, no. 11, 2014.

[79] H. W. Shin and J. Y. Son, "Multiferroic $BiFeO_3$ thin films and nanodots grown on highly oriented pyrolytic graphite substrates," *J. Cryst. Growth*, vol. 480, pp. 13–17, 2017.

[80] G. Catalan and J. F. Scott, "Physics and applications of bismuth ferrite," *Advanced Materials*, vol. 21, no. 24. pp. 2463–2485, 2009.

[81] N. Liu *et al.*, "Ultratransparent and stretchable graphene electrodes," *Sci. Adv.*, vol. 3, no. 9, 2017.

[82] S. Pang, Y. Hernandez, X. Feng, and K. Müllen, "Graphene as transparent electrode material for organic electronics," *Adv. Mater.*, vol. 23, no. 25, pp. 2779–2795, 2011.

[83] E. P. Sharel, Y. R. Kim, D. Perry, C. L. Bentley, and P. R. Unwin, "Nanoscale Electrocatalysis of Hydrazine Electro-Oxidation at Blistered Graphite Electrodes," *ACS Appl. Mater. Interfaces*, vol. 8, no. 44, pp. 30458–30466, 2016.

[84] B. Lesiak *et al.*, "Csp2/sp3 hybridisations in carbon nanomaterials – XPS and (X)AES study," *Appl. Surf. Sci.*, vol. 452, pp. 223–231, 2018.

[85] A. S. Cavanagh, C. A. Wilson, A. W. Weimer, and S. M. George, "Atomic layer deposition on quantities of multiwalled carbon nanotubes," in *Materials Research Society Symposium Proceedings*, 2008, vol. 1054, pp. 81–92.

[86] Y. Xuan *et al.*, "Atomic-layer-deposited nanostructures for graphene-based nanoelectronics," *Appl. Phys. Lett.*, vol. 92, no. 1, 2008.

[87] M. J. Young, C. B. Musgrave, and S. M. George, "Growth and Characterization of Al_2O_3 Atomic Layer Deposition Films on sp2-Graphitic Carbon Substrates Using NO_2/Trimethylaluminum Pretreatment," *ACS Appl. Mater. Interfaces*, vol. 7, no. 22, pp. 12030–12037, 2015.

[88] X. Wang *et al.*, "Low-temperature fabrication of $Bi_{25}FeO_{40}$/rGO nanocomposites with

efficient photocatalytic performance under visible light irradiation," *RSC Adv.*, vol. 7, no. 17, pp. 10064–10069, 2017.

[89] A. Knápek, D. Sobola, P. Tománek, Z. Pokorná, and M. Urbánek, "Field emission from the surface of highly ordered pyrolytic graphite," *Appl. Surf. Sci.*, vol. 395, pp. 157–161, 2017.

[90] M. J. Webb, P. Palmgren, P. Pal, O. Karis, and H. Grennberg, "A simple method to produce almost perfect graphene on highly oriented pyrolytic graphite," *Carbon N. Y.*, vol. 49, no. 10, pp. 3242–3249, 2011.

[91] V. W. Brar *et al.*, "Second-order harmonic and combination modes in graphite, single-wall carbon nanotube bundles, and isolated single-wall carbon nanotubes," *Phys. Rev. B - Condens. Matter Mater. Phys.*, vol. 66, no. 15, pp. 1–10, 2002.

[92] T. Shimada *et al.*, "Origin of the 2450 cm-1 Raman bands in HOPG, single-wall and double-wall carbon nanotubes," *Carbon N. Y.*, vol. 43, no. 5, pp. 1049–1054, 2005.

[93] R. Kostić, M. Mirić, T. Radić, M. Radović, R. Gajić, and Z. V. Popović, "Optical characterization of graphene and highly oriented pyrolytic graphite," in *Acta Physica Polonica A*, 2009, vol. 116, no. 4, pp. 718–721.

[94] D. Lohse and X. Zhang, "Surface nanobubbles and nanodroplets," *Rev. Mod. Phys.*, vol. 87, no. 3, 2015.

[95] H. An, B. H. Tan, J. G. S. Moo, S. Liu, M. Pumera, and C. D. Ohl, "Graphene Nanobubbles Produced by Water Splitting," *Nano Lett.*, vol. 17, no. 5, pp. 2833–2838, 2017.

[96] Z. Y. Xia *et al.*, "The exfoliation of graphene in liquids by electrochemical, chemical, and sonication-assisted techniques: A nanoscale study," *Adv. Funct. Mater.*, vol. 23, no. 37, pp. 4684–4693, 2013.

[97] H. T. Fan, S. S. Pan, X. M. Teng, C. Ye, and G. H. Li, "Structure and thermal stability of δ-Bi2O3 thin films deposited by reactive sputtering," *J. Phys. D. Appl. Phys.*, vol. 39, no. 9, pp. 1939–1943, 2006.

[98] L. Liu, Z. Zhou, H. Tian, and J. Li, "Effect of bismuth oxide on the microstructure and electrical conductivity of yttria stabilized zirconia," *Sensors (Switzerland)*, vol. 16, no. 3, pp. 2–10, 2016.

[99] X. Y. Pang, Z. Q. Liu, S. Q. Wang, and J. K. Shang, "First-principles Investigation of Bi Segregation at the Solder Interface of Cu/Cu3Sn(010)," *J. Mater. Sci. Technol.*, vol. 26, no. 12, pp. 1057–1062, 2010.

[100] C. W. Yang, Y. H. Lu, and I. S. Hwang, "Imaging surface nanobubbles at graphite-water interfaces with different atomic force microscopy modes," *J. Phys. Condens. Matter*, vol. 25, no. 18, 2013.

[101] H. Teshima, T. Nishiyama, and K. Takahashi, "Nanoscale pinning effect evaluated from deformed nanobubbles," *J. Chem. Phys.*, vol. 146, no. 1, 2017.

[102] R. Backreedy, J. M. Jones, M. Pourkashanian, and A. Williams, "A study of the reaction of oxygen with graphite: Model chemistry," *Faraday Discuss.*, vol. 119, no. 1, pp. 385–394, 2002.

[103] D. Chen, F. Niu, L. Qin, S. Wang, N. Zhang, and Y. Huang, "Defective BiFeO3 with surface oxygen vacancies: Facile synthesis and mechanism insight into photocatalytic performance," *Sol. Energy Mater. Sol. Cells*, vol. 171, pp. 24–32, 2017.

[104] D. Briggs, “Handbook of X-ray Photoelectron Spectroscopy C. D. Wanger, W. M. Riggs, L. E. Davis, J. F. Moulder and G. E.Muilenberg Perkin-Elmer Corp., Physical Electronics Division, Eden Prairie, Minnesota, USA, 1979. 190 pp. $195,” in *Surface and Interface Analysis*, vol. 3, no. 4, 1981, pp. v–v.

[105] A. Mukherjee, S. Chakrabarty, N. Kumari, W. N. Su, and S. Basu, “Visible-Light-Mediated Electrocatalytic Activity in Reduced Graphene Oxide-Supported Bismuth Ferrite,” *ACS Omega*, vol. 3, no. 6, pp. 5946–5957, 2018.

[106] R. Das, S. Sharma, and K. Mandal, “Aliovalent Ba2+ doping: A way to reduce oxygen vacancy in multiferroic BiFeO3,” *J. Magn. Magn. Mater.*, vol. 401, pp. 129–137, 2016.

[107] D. Barreca, F. Morazzoni, G. A. Rizzi, R. Scotti, and E. Tondello, “Molecular oxygen interaction witha spectroscopic and Bi_2O_3: Spectromagnetic investigation,” *Phys. Chem. Chem. Phys.*, vol. 3, no. 9, pp. 1743–1749, 2001.

[108] T. Ohgi, H. Y. Sheng, Z. C. Dong, H. Nejoh, and D. Fujita, “Charging effects in gold nanoclusters grown on octanedithiol layers,” *Appl. Phys. Lett.*, vol. 79, no. 15, pp. 2453–2455, 2001.

[109] S. Pei and H. M. Cheng, “The reduction of graphene oxide,” *Carbon N. Y.*, vol. 50, no. 9, pp. 3210–3228, 2012.

[110] L. Stobinski *et al.*, “Graphene oxide and reduced graphene oxide studied by the XRD, TEM and electron spectroscopy methods,” *J. Electron Spectros. Relat. Phenomena*, vol. 195, pp. 145–154, 2014.

[111] B. Gupta, N. Kumar, K. Panda, V. Kanan, S. Joshi, and I. Visoly-Fisher, “Role of oxygen functional groups in reduced graphene oxide for lubrication,” *Sci. Rep.*, vol. 7, 2017.

[112] W. Gao, “The chemistry of graphene oxide,” *Graphene Oxide Reduct. Recipes, Spectrosc. Appl.*, pp. 61–95, 2015.

[113] Y. Sun, X. Hu, W. Luo, and Y. Huang, “Self-assembled hierarchical MoO2/graphene nanoarchitectures and their application as a high-performance anode material for lithium-ion batteries,” *ACS Nano*, vol. 5, no. 9, pp. 7100–7107, 2011.

[114] P. Kaspar *et al.*, “Characterization of Fe_2O_3 thin film on highly oriented pyrolytic graphite by AFM, Ellipsometry and XPS,” *Appl. Surf. Sci.*, vol. 493, pp. 673–678, 2019.

[115] S. A. Theofanidis, V. V. Galvita, C. Konstantopoulos, H. Poelman, and G. B. Marin, “Fe-based nano-materials in catalysis,” *Materials*, vol. 11, no. 5. 2018.

[116] S. Han and C. Sung Kim, “Weak ferromagnetic behavior of $BiFeO_3$ at low temperature,” in *Journal of Applied Physics*, 2013, vol. 113, no. 17.

[117] N. Zhang, D. Chen, F. Niu, S. Wang, L. Qin, and Y. Huang, “Enhanced visible light photocatalytic activity of Gd-doped BiFeO3 nanoparticles and mechanism insight,” *Sci. Rep.*, vol. 6, 2016.

[118] H. Guan, X. Zhang, and Y. Xie, “Soft-chemical synthetic nonstoichiometric $Bi_2O_{2.33}$ nanoflower: A new room-temperature ferromagnetic semiconductor,” *J. Phys. Chem. C*, vol. 118, no. 46, pp. 27170–27174, 2014.

[119] C. Gómez-Polo, S. Larumbe, and J. M. Pastor, “Room temperature ferromagnetism in non-magnetic doped TiO_2 nanoparticles,” in *Journal of Applied Physics*, 2013, vol. 113, no. 17.

[120] S. Chen *et al.*, "Oxygen vacancy associated single-electron transfer for photofixation of CO_2 to long-chain chemicals," *Nat. Commun.*, vol. 10, no. 1, 2019.

[121] Y. Luo *et al.*, "Controlled synthesis of hierarchical graphene-wrapped TiO $_2$@Co_3O_4 coaxial nanobelt arrays for high-performance lithium storage," *J. Mater. Chem. A*, vol. 1, no. 2, pp. 273–281, 2013.

[122] P. Kumar and M. Kar, "Effect of structural transition on magnetic and dielectric properties of la and Mn co-substituted $BiFeO_3$ ceramics," *Mater. Chem. Phys.*, 2014.

[123] P. Chen *et al.*, "Enhanced Magnetic Anisotropy and Orbital Symmetry Breaking in Manganite Heterostructures," *Adv. Funct. Mater.*, 2020.

[124] Y. F. Wu *et al.*, "Magnetic proximity effect in graphene coupled to a $BiFeO_3$ nanoplate," *Phys. Rev. B*, 2017.

[125] S. Lai *et al.*, "Submicron bubbles/voids formation in the subsurface region of soda-lime glass by single pulse fs laser-induced spallation," *Appl. Surf. Sci.*, 2020.

[126] J. Wang *et al.*, "Epitaxial $BiFeO_3$ multiferroic thin film heterostructures," *Science (80).*, vol. 299, no. 5613, pp. 1719–1722, 2003.

[127] M. K. Singh, H. M. Jang, S. Ryu, and M. H. Jo, "Polarized Raman scattering of multiferroic $BiFeO_3$ epitaxial films with rhombohedral R3c symmetry," *Appl. Phys. Lett.*, vol. 88, no. 4, pp. 1–3, 2006.

[128] C. Wang *et al.*, "Leakage current of multiferroic $(Bi_{0.6}Tb_{0.3}La_{0.1})FeO_3$ thin films grown at various oxygen pressures by pulsed laser deposition and annealing effect," *J. Appl. Phys.*, vol. 99, no. 5, p. 054104, 2006.

[129] A. A. Porporati, K. Tsuji, M. Valant, A. K. Axelsson, and G. Pezzotti, "Raman tensor elements for multiferroic $BiFeO_3$ with rhombohedral R3c symmetry," *J. Raman Spectrosc.*, 2010.

[130] P. Hermet, M. Goffinet, J. Kreisel, and P. Ghosez, "Raman and infrared spectra of multiferroic bismuth ferrite from first principles," *Phys. Rev. B - Condens. Matter Mater. Phys.*, 2007.

[131] B. Chaitongrat and S. Chaisitsak, "Fabrication of SWNTs/α-Fe_2O_3 as room-temperature LPG sensor," in *2015 IEEE SENSORS - Proceedings*, 2015.

[132] Y. Li, T. Sritharan, S. Zhang, X. He, Y. Liu, and T. Chen, "Multiferroic properties of sputtered BiFe O3 thin films," *Appl. Phys. Lett.*, 2008.

[133] Y. Huang *et al.*, "Different approaches for preparing a novel thiol-functionalized graphene oxide/Fe-Mn and its application for aqueous methylmercury removal," *Chem. Eng. J.*, 2017.

[134] Y. Hu, D. Li, F. Sun, Y. Weng, S. You, and Y. Shao, "Temperature-induced phase changes in bismuth oxides and efficient photodegradation of phenol and p-chlorophenol," *J. Hazard. Mater.*, 2016.

[135] W. Lin, X. Yu, Y. Zhu, and Y. Zhang, "Graphene oxide/BiOCl nanocomposite films as efficient visible light photocatalysts," *Front. Chem.*, 2018.

[136] Q. Zhang *et al.*, "A facile approach to build $Bi_2O_2CO_3$/PCN nanohybrid photocatalysts for gaseous acetaldehyde efficient removal," *Catal. Today*, 2018.

[137] S. Jaiswar and K. D. Mandal, "Evidence of Enhanced Oxygen Vacancy Defects Inducing Ferromagnetism in Multiferroic $CaMn_7O_{12}$ Manganite with Sintering Time,"

J. Phys. Chem. C, 2017.

[138] K. K. Shukla *et al.*, "Magnetic and optical properties of Fe doped crednerite $CuMnO_2$," *RSC Adv.*, 2015.

[139] C. Luo *et al.*, "Azo Compounds Derived from Electrochemical Reduction of Nitro Compounds for High Performance Li-Ion Batteries," *Adv. Mater.*, 2018.

[140] M. Omran, T. Fabritius, A. M. Elmahdy, N. A. Abdel-Khalek, M. El-Aref, and A. E. H. Elmanawi, "XPS and FTIR spectroscopic study on microwave treated high phosphorus iron ore," *Appl. Surf. Sci.*, 2015.

[141] G. Abadias *et al.*, "Review Article: Stress in thin films and coatings: Current status, challenges, and prospects," *J. Vac. Sci. Technol. A Vacuum, Surfaces, Film.*, 2018.

[142] T. Jin, Q. Han, Y. Wang, and L. Jiao, "1D Nanomaterials: Design, Synthesis, and Applications in Sodium–Ion Batteries," *Small*. 2018.

[143] C. Teichert and I. Beinik, "Conductive atomic-force microscopy investigation of nanostructures in microelectronics," *Nanosci. Technol.*, 2011.

[144] U. Hartmann, *Magnetic force microscopy*. 1999.

[145] J. Zhong and J. Yan, "Seeing is believing: Atomic force microscopy imaging for nanomaterial research," *RSC Advances*. 2016.

[146] S. Liu and Y. Wang, "Application of AFM in microbiology: A review," *Scanning*. 2010.

[147] A. S. Cuharuc, G. Zhang, and P. R. Unwin, "Electrochemistry of ferrocene derivatives on highly oriented pyrolytic graphite (HOPG): Quantification and impacts of surface adsorption," *Phys. Chem. Chem. Phys.*, vol. 18, no. 6, pp. 4966–4977, 2016.

[148] S. Ma, T. Gao, X. Chen, C. Xiao, T. Lu, and X. Jiang, "Formation and behaviors of helium bubbles in Li_4SiO_4: A molecular dynamics simulation," *Comput. Mater. Sci.*, vol. 169, 2019.

[149] Dupont, "DuPont ™ Kapton ®," *http://www.dupont.com/content/dam/dupont/products-and-services/membranes-and-films/polyimde-films/documents/DEC-Kapton-summary-of-properties.pdf*, 2012.

[150] A. Bedoya-Pinto, M. Donolato, M. Gobbi, L. E. Hueso, and P. Vavassori, "Flexible spintronic devices on Kapton," *Appl. Phys. Lett.*, 2014.

[151] E. Lindner *et al.*, "Flexible (Kapton-based) microsensor arrays of high stability for cardiovascular applications," *J. Chem. Soc. Faraday Trans.*, 1993.

[152] J. Tuttle, M. Dipirro, E. Canavan, and T. Hait, "Thermal properties of double-aluminized kapton at low temperatures," in *AIP Conference Proceedings*, 2008.

[153] T. Tchangai, Y. Segui, and K. Doukkali, "Water sorption in polyamide–imide films and its effect on dielectric loss," *J. Appl. Polym. Sci.*, 1989.

[154] B. L. Sharma and P. K. C. Pillai, "Electrical conduction in Kapton polyimide film at high electrical fields," *Polymer (Guildf).*, 1982.

[155] J. O. Simpson and A. K. St.Clair, "Fundamental insight on developing low dielectric constant polyimides," *Thin Solid Films*, 1997.

[156] J. K. Quamara, P. K. C. Pillai, and B. L. Sharma, "Surface potential decay characteristics and TSDC studies in corona charged kapton polyimide film," *Acta*

Polym., 1983.

[157] W. Bu, J. Yin, F. Tian, G. Li, and Q. Lei, "Effect of corona ageing on the structure changes of polyimide and polyimide/Al_2O_3 nanocomposite films," *J. Electrostat.*, 2011.

[158] K. K. De Groh and B. A. Banks, "Atomic-oxygen undercutting of long duration exposu facility aluminized-kapton multilayer insulation," *J. Spacecr. Rockets*, 1994.

[159] J. DEVER, E. BRUCKNER, and E. RODRIGUEZ, "Synergistic effects of ultraviolet radiation, thermal cycling and atomic oxygen on altered and coated Kapton surfaces," 1992.

[160] N. Papež *et al.*, "Surface morphology after reactive ion etching of silicon and gallium arsenide based solar cells," *J. Phys. Conf. Ser.*, vol. 1124, no. 4, p. 041015, Dec. 2018.

[161] Ş. Ţălu, P. Nikola, D. Sobola, A. Achour, and S. Solaymani, "Micromorphology investigation of GaAs solar cells: case study on statistical surface roughness parameters," *J. Mater. Sci. Mater. Electron.*, vol. 28, no. 20, pp. 15370–15379, 2017.

[162] R. Shikhgasan, Ţ. Ştefan, S. Dinara, S. Sebastian, and R. Guseyn, "Epitaxy of silicon carbide on silicon: Micromorphological analysis of growth surface evolution," *Superlattices Microstruct.*, vol. 86, pp. 395–402, 2015.

[163] N. Papež *et al.*, "Degradation analysis of GaAs solar cells at thermal stress," *Appl. Surf. Sci.*, vol. 461, pp. 212–220, 2018.

[164] S. Venkatachalam, D. Bertin, G. Ducournau, J. F. Lampin, and D. Hourlier, "Kapton-derived carbon as efficient terahertz absorbers," *Carbon N. Y.*, vol. 100, pp. 158–164, 2016.

[165] Y. Xie, Y. Gao, X. Qin, H. Liu, and J. Yin, "Preparation and properties of atomic oxygen protective films deposited on Kapton by solvothermal and sol-gel methods," *Surf. Coatings Technol.*, vol. 206, no. 21, pp. 4384–4388, 2012.

[166] M. A. Signore *et al.*, "Growth assessment of (002)-oriented AlN thin films on Ti bottom electrode deposited on silicon and kapton substrates," *Mater. Des.*, vol. 119, pp. 151–158, 2017.

[167] P. S. M. and J. M. H Ki, "Modelling of high-density laser–material interaction using fast level set method," *J. Phys. D. Appl. Phys.*, vol. 34, pp. 364–372, 2001.

[168] R. Sobiestianskas, A. Hardy, J. Banys, J. D'haen, and B. van, "Microwave dielectric properties of $BiFeO_3$ thin film prepared by aqueous chemical solution deposition method," *Process. Appl. Ceram.*, 2009.

[169] J. X. Zhu, X. D. Wen, J. T. Haraldsen, M. He, C. Panagopoulos, and E. E. M. Chia, "Induced ferromagnetism at BiFeO3/YBa2Cu 3O7 interfaces," *Sci. Rep.*, 2014.

[170] A. F. Volkov, Y. V. Fominov, and K. B. Efetov, "Long-range odd triplet superconductivity in superconductor-ferromagnet structures with Néel walls," *Phys. Rev. B - Condens. Matter Mater. Phys.*, 2005.

[171] D. Ivanov and Y. Fominov, "Minigap in superconductor-ferromagnet junctions with inhomogeneous magnetization," *Phys. Rev. B-Condens.Matter Mater. Phys.*, 2006.

[172] I. S. Beloborodov, Y. V. Fominov, A. V. Lopatin, and V. M. Vinokur, "Insulating state of granular superconductors in a strong-coupling regime," *Phys. Rev. B - Condens. Matter Mater. Phys.*, 2006.

Appendix 1
WOS: 000419168300010

Received: 25 June 2017 | Revised: 14 August 2017 | Accepted: 30 August 2017

DOI: 10.1002/jemt.22945

RESEARCH ARTICLE

WILEY MICROSCOPY RESEARCH & TECHNIQUE

Influence of scanning rate on quality of AFM image: Study of surface statistical metrics

Dinara Sobola[1] | Ştefan Ţălu[2] | Shahram Solaymani[3] | Lubomír Grmela[1]

[1]Faculty of Electrical Engineering and Communication, Physics Department, Brno University of Technology, Technická 8, Brno 616 00, Czech Republic

[2]Faculty of Mechanical Engineering, Department of AET, Discipline of Descriptive Geometry and Engineering Graphics, Technical University of Cluj-Napoca, 103-105 B-dul Muncii St, Cluj-Napoca, Cluj 400641, Romania

[3]Department of Physics, Science and Research Branch, Islamic Azad University, Tehran, Iran

Correspondence
Sobola Dinara, PhD, Brno University of Technology, Faculty of Electrical Engineering and Communication, Physics Department, Technická 8, 616 00 Brno, Czech Republic.
Email: sobola@vutb.cz

Funding information
Ministry of Education, Youth and Sports of the Czech Republic under the project CEITEC 2020 (LQ1601); Grant Agency of the Czech Republic under no. GACR 15-05259S; National Sustainability Program, Grant/Award Number: LO1401

Review Editor: Prof. Jose Luis Toca-Herrera

Abstract

The purpose of this work is to study the dependence of AFM-data reliability on scanning rate. The three-dimensional (3D) surface topography of the samples with different micro-motifs is investigated. The analysis of surface metrics for estimation of artifacts from inappropriate scanning rate is presented. Fractal analysis was done by cube counting method and evaluation of statistical metrics was carrying out on the basis of AFM-data. Combination of quantitate parameters is also presented in graphs for every measurement. The results indicate that the sensitivity to scanning rate growths with fractal dimension of the sample. This approach allows describing the distortion of the images against scanning rate and could be applied for dependences on the other measurement parameters. The article explains the relevance and comparison of fractal and statistical surface parameters for characterization of data distortion caused by inappropriate choice of scanning rate.

KEYWORDS

atomic force microscopy, fractal analysis, scanning rate, surface micro-morphology

1 | INTRODUCTION

One of the challenges of nanometrics is precise estimation of geometric sizes. Surface condition affects mechanical, electrical, chemical properties of the elements. So, performing of surface precise inspection is an important task at a number of engineering fields (Ţălu, 2015).

There are a lot of methods and microscopy techniques for study of the surface topography. Every method possesses its own set of artifacts which should be taken into account for data evaluation. The artifacts of measurements and mistakes originate from different factors: wrong sample preparation, external and internal noises, wrong choice of measurement parameters, and so forth. One of the solutions for the right results interpretation is careful data processing, using of filters, fitting techniques, and so forth. (Ramazanov, Ţălu, Sobola, Stach, & Ramazanov, 2015; Stach et al., 2015; Ţălu et al., 2014).

Atomic force microscope (AFM) is a modern solution which provides additional benefits to the geometrical data with real values of surface features in *Z*-coordinate and it is one of the essential instruments for nanotechnology. It provides true information about geometrical sizes of the surface features (Berezina, Il'icheva, Podzorova, & Ţălu, 2015; Elenkova et al., 2015; Méndez, Reyes, Trejo, Stępień, & Ţălu, 2015; Naseri et al., 2017; Stach et al., 2017). AFM supposes study of the surface with nanoscale resolution.

Artifact-free AFM images of surface are important for all fields of material research both organic and inorganic nature. Innovations in surface science define the enhancements of micro-electronics and photonics devices. But precise control of surface properties and topography is also one of the great challenges, because the development of scanning microscopes depends on state of art of modern electronics. One of the problems of such fields as photonics, nano-

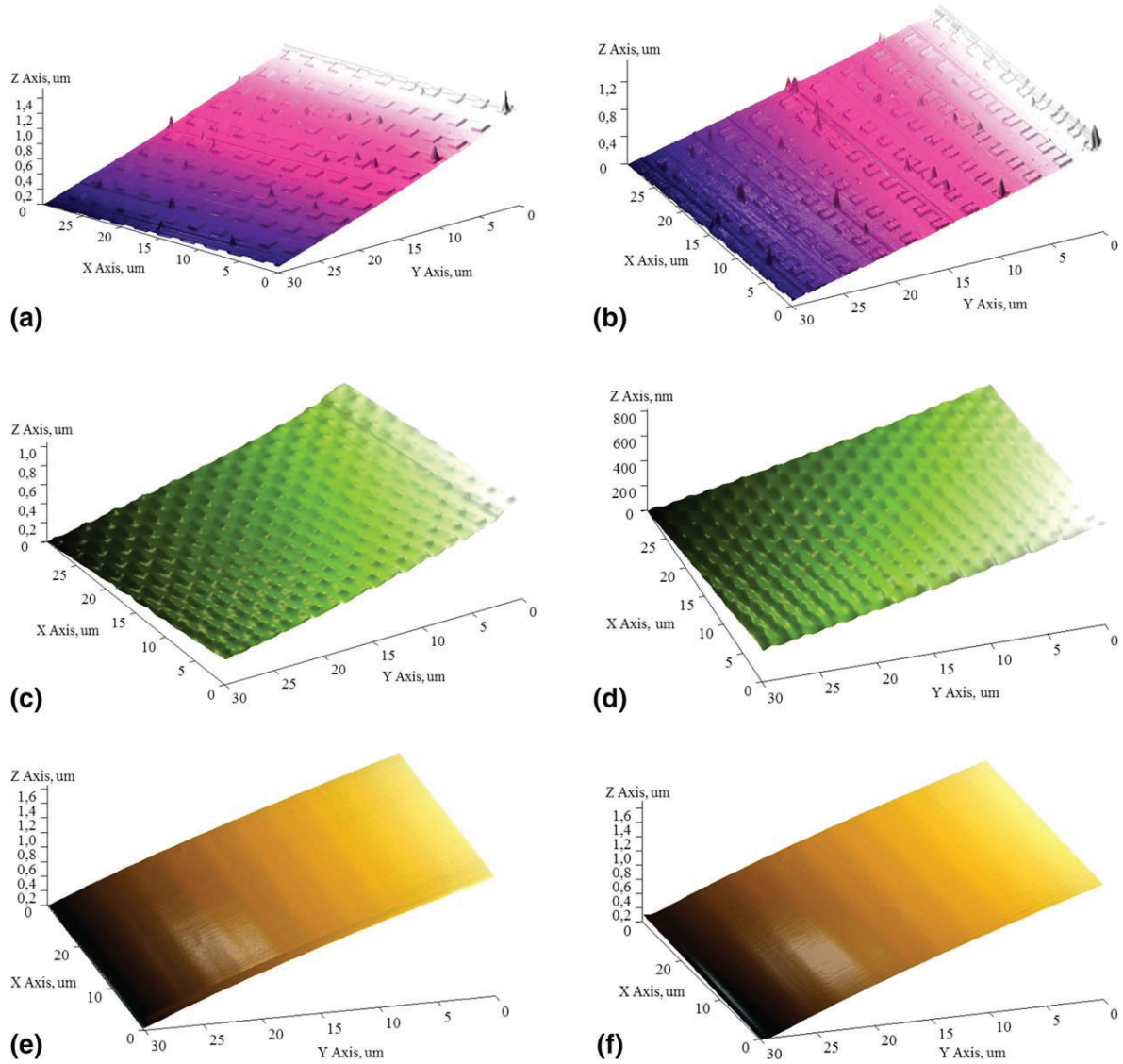

FIGURE 1 The representative 3D topographic AFM images, for scanning square area of 30 × 30 μm^2, of the Samples 1, 2, and 3. (a) Sample 1, 61 μm per sec. (b) Sample 1, 314 μm per sec. (c) Sample 2, 61 μm per sec. (d) Sample 2, 314 μm per sec. (e) Sample 3, 61 μm per. (f) Sample 3, 314 μm per sec[Color figure can be viewed at wileyonlinelibrary.com]

magnetism, nanoelectronics is a problem of surface quality control. Reliable data of AFM contributes both preparation of new structures for electronics (Šik et al., 2016) and characterization of existing optoelectronic devises to improve their efficiency (Dallaeva, Tomanek, Skarvada, & Grmela, 2015; Skarvada et al., 2016).

AFM data contributes progress in chemistry of surface and analytical chemistry. AFM provides possibility to investigate surface chemistry, interfacial interactions between the chemical groups (Jradi, Schmitt, & Bistac, 2012).

AFM imaging of biological samples in different atmosphere conditions or solutions can be carry out with simple sample preparation steps. Using of different AFM modes help to study mechanical properties of biological samples, as architecture of complicated structures and elastic properties of the tissues. (Yeow, Taborb, & Garnier, 2017). AFM gave to biotechnology another insight to properties and structure of materials and explained their properties (Dallaeva, Tomanek, Prokopyeva, et al., 2015).

Sample–tip interaction varies in dependence on the demanded scanning mode. Distance between sample and tip defines is also essential. AFM can work in contact, semi-contact, and non-contact modes. These types of microscopy are correlated with additional measurement of AFM techniques (measurement of resistance in contact mode, phase contrast of materials in semi-contact mode, magnetic force microcopy in non-contact mode, etc.). AFM could be adapted for measurements of various surface properties and characteristics. It explains notability of AFM in many fields of materials research. Besides imaging of topography, it allows investigation of physical (mechanical, electrical) and chemical (surface defects) properties, nanoobjects preparation and manipulation. It is

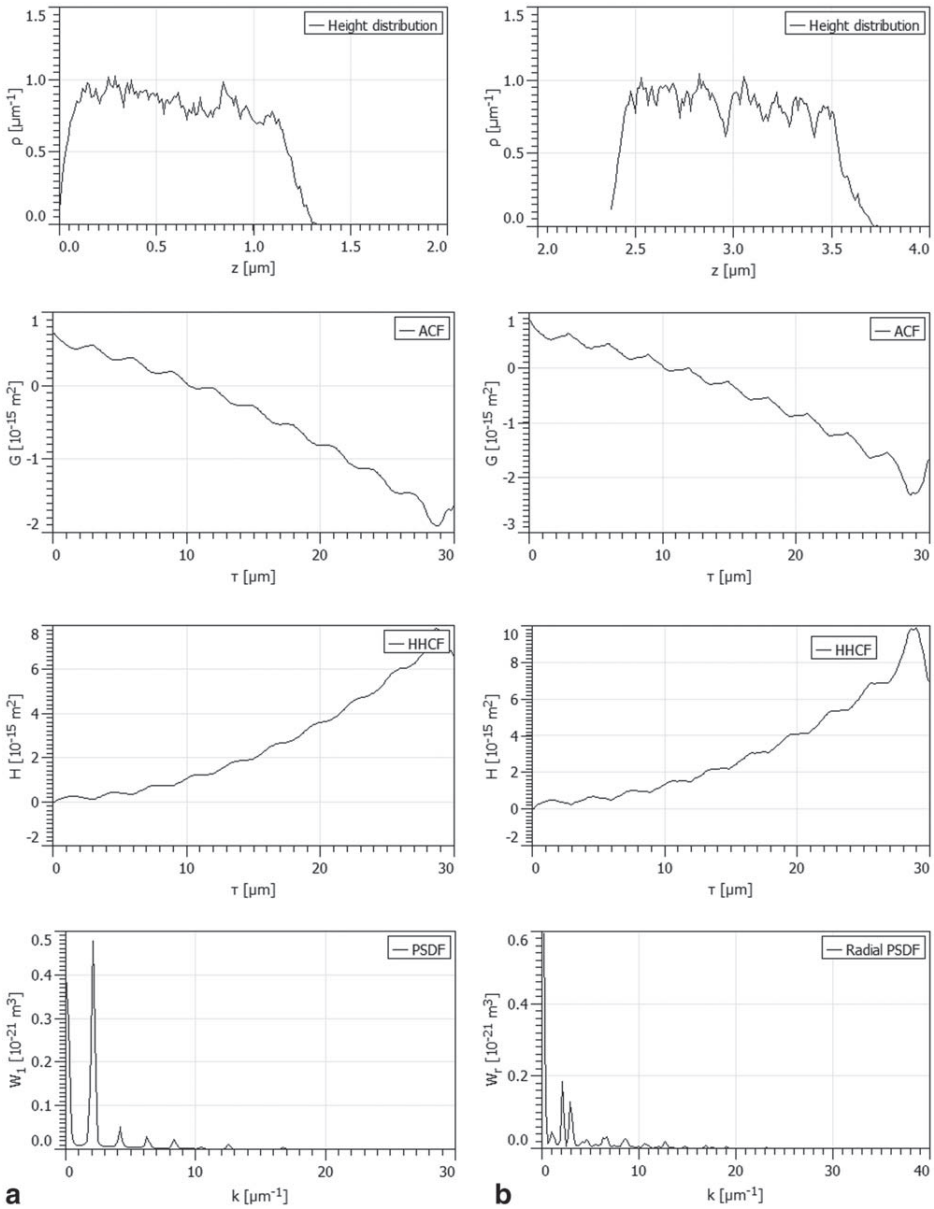

FIGURE 2 Sample 1 (a) 61 μm per sec; (b) 314 μm per sec; (a1) Height distribution; (a2) in horizontal direction; (a3) in horizontal direction; (a4) radial PSDF; (b1) Height distribution; (b2) in horizontal direction; (b3) in horizontal direction; (b4) radial PSDF

possible to study processes of chemical adsorption, self-assembly, changing of domain structures. Probe-surface interactions depend on the material of probe and sample, distance between them, ambient of measurements, and so forth. Various combinations of these parameters provide a large number of measurements modes.

AFM spectroscopies provide data (dependences) from the chosen surface points, which are based on tip-sample distance. The AFM spectroscopies are precise and sensitive. AFM force spectroscopy detects pico newton forces (Yeow et al., 2017). The number of AFM spectroscopy techniques is continuously developing. AFM-based dielectric spectroscopy was reported at (Miccio, Kummali, Schwartz, Alegría, & Colmenero 2014) for measurement of the dielectric relaxation of materials at the nanoscale. Atomic Force Acoustic Microscopy and Force Spectroscopy, was successfully used for mapping of the distribution pattern in biomaterials (Knotek, Chanova, & Rypacek, 2013).

Using of advanced probes for measurements, sub-nanometer resolution improves characterizing of nanoelectronics devices and structures (Hantschel et al., 2016). The electrical characteristics could be measured at the pico level using conductive cantilevers (Benlia & Yalın, 2017). Conductive methods of AFM are of interest for both sensors and electronic application and analyzing materials for biotechnology and medical products (Benlia & Yalın, 2017). Spatial maps of surface potential could be investigated by Kelvin Probe Force Microscopy. It also allows studying of workfunction variations, contrast p and n

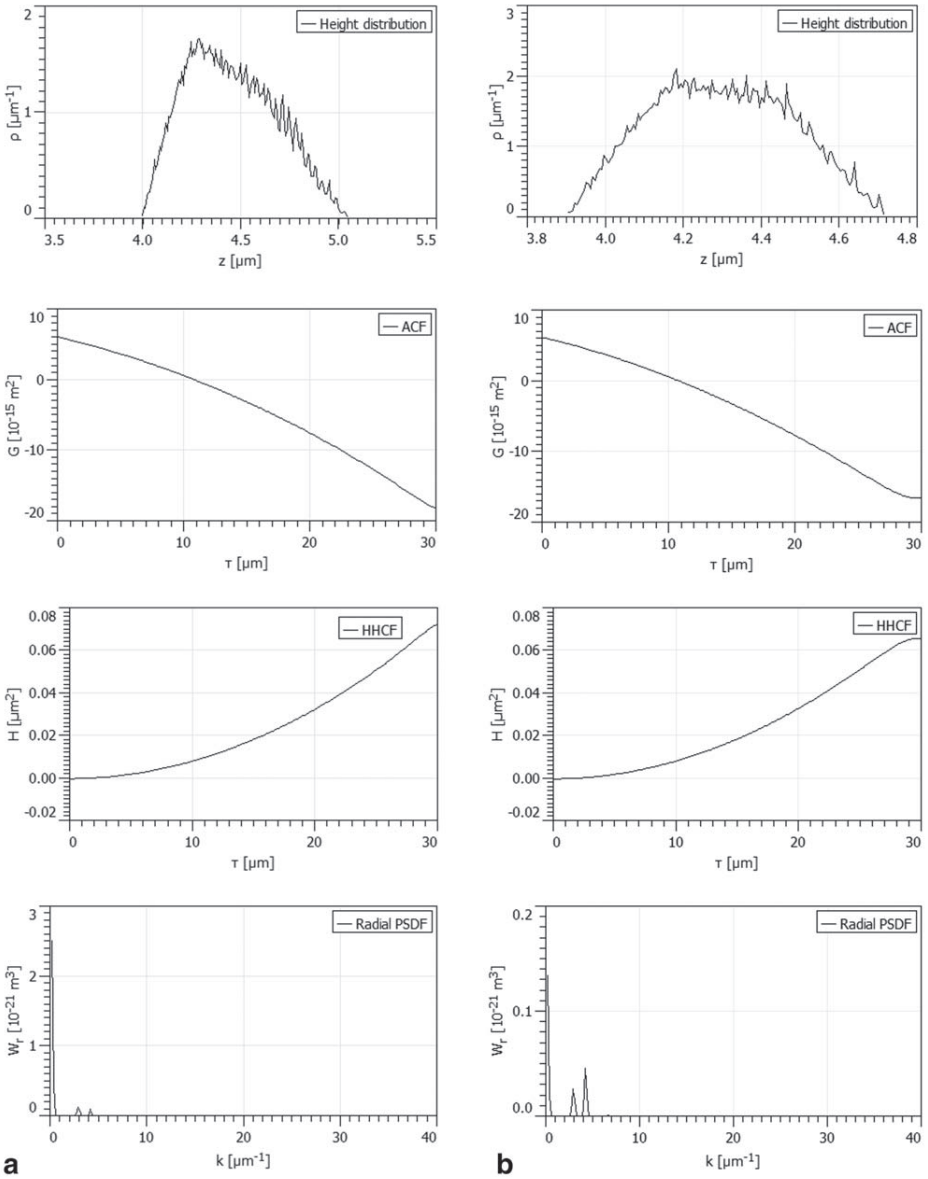

FIGURE 3 Sample 1 (a) 61 μm per sec; (b) 314 μm per sec; (a1) Height distribution; (a2) in horizontal direction; (a3) in horizontal direction; (a4) radial PSDF; (b1) Height distribution; (b2) in horizontal direction; (b3) in horizontal direction; (b4) radial PSDF

regions, perform surface potential-gate bias spectroscopy, resolve time dependent phenomenon like photovoltage in response to illumination, both the injection and extraction of carriers (Moscatello et al., 2017). This technique characterizes electronically different regions of surface (Ryu et al., 2015). Imaging of magnetic properties with high spatial resolution provides magnetic force microscopy (Koblischka, Hartmann, & Sulzbach, 2003). Electrical AFM methods (KFPM, spreading resistence) have high potential for nanometer-scale device characterization (Hantschel et al., 2016).

AFM provides insight to dimensional metrology of many different scientific fields. Modern scientific literature provides information about common AFM artifacts, such as corrupted edges of surface features, various noise, vibrations, tip-sample convolutions, and so forth. (Gołek, Mazur, Ryszka, & Zuber, 2014; Shen, Zhang, Zhang, & Gan, 2017). Every type of artifact has its own explanation and method to its elimination. So, the artifacts in AFM images could originate from tip geometry and impact surface topographical characteristics. Tip sharpness is essential for imaging of surfaces with low roughness at sufficient resolution (Canet-Ferrer, Coronado, Forment-Aliaga, & Pinilla-Cienfuegos, 2014). The properties of scanning probe contribute the scanning rate and represent of technological challenges which should be overcome (Slattery, Blanch, Quinton & Gibson, 2013). In spite that blind tip reconstruction algorithm for evaluation of tip geometry and reconstruction of AFM images was suggested in 90s (Villarrubia, 1997), the problem of AFM data processing is still not completely solved. The reason is

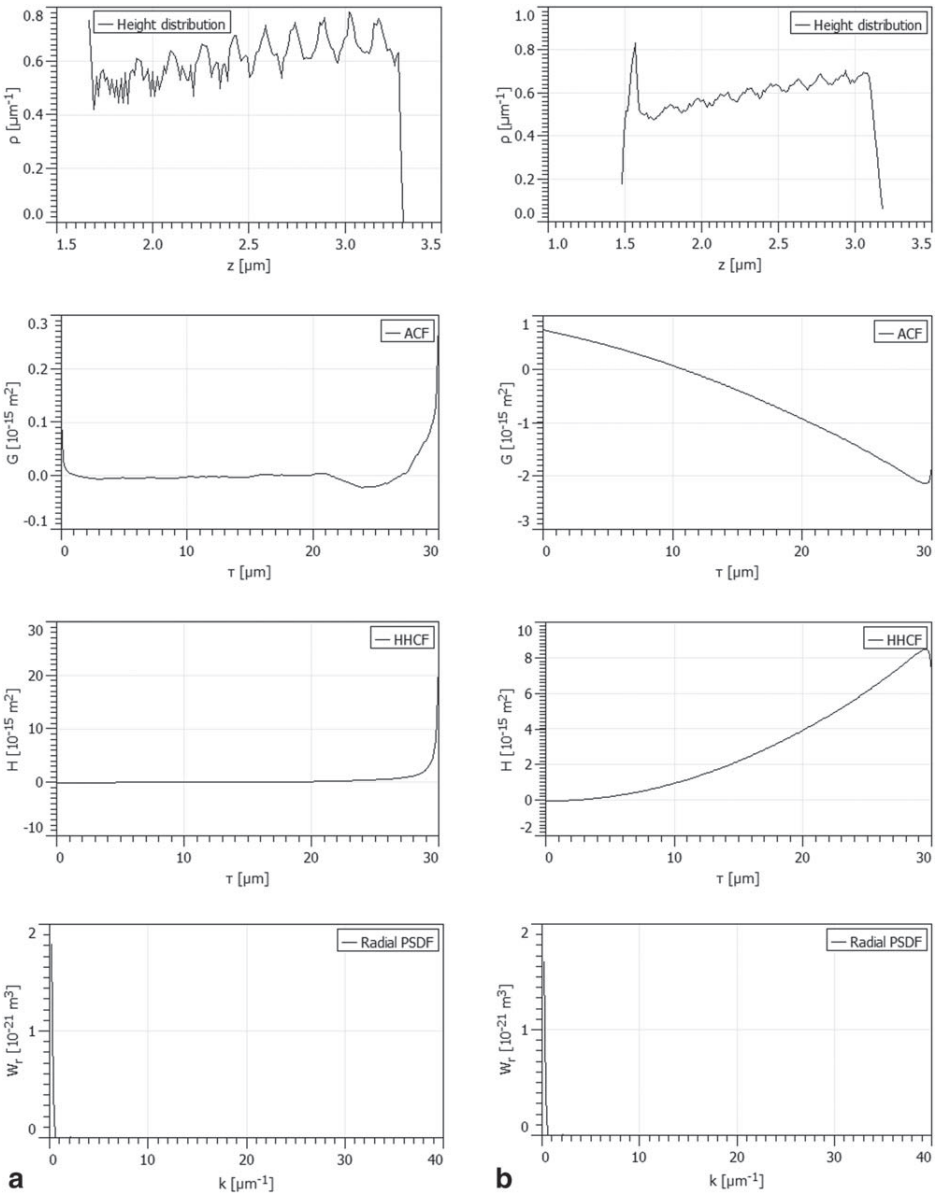

FIGURE 4 Sample 1 (a) 61 μm per sec; (b) 314 μm per sec; (a1) Height distribution; (a2) in horizontal direction; (a3) in horizontal direction; (a4) radial PSDF; (b1) Height distribution; (b2) in horizontal direction; (b3) in horizontal direction; (b4) radial PSDF

numerous factors that influence the measurement. The importance of tip geometry also should not be ignored for estimation of nanoscale images (Rodriguez, Lacaze, & Jupille, 2012).

It was noted at the earlier report (Poljacek, Risovic, Furic, & Gojo, 2008) that the different topography surfaces can have similar statistical parameters because these parameters do not characterize the complexity of topography. Statistical parameters in combination with fractal analysis have been widely used in studies of both regular and irregular surface features (Arman et al., 2015; Dallaeva et al., 2014; Méndez et al, 2017; Reyes-Vidal et al., 2015; Ţălu et al., 2016; Ţălu, Stach, Raoufi, & Hosseinpanahi, 2015; Yadav, Dwivedi, Mittal, Kumar, & Pandey, 2012).

Besides considering all mentioned problems it is necessary to take into account geometrical properties of surface features. The study of sample shape contribution can enhance the reliability of data with increasing of rate of the samples investigation. Mean value, variance of heights cannot give a complete estimation of surface (Goerke & Willner, 2008). Conversely, 3D statistical and fractal parameters of surface topography are more informative then 2D image of the surface appearance.

Recently was reported (Ţălu, Stępień, & Caglayan, 2015) about wavelet analysis to characterize the 3D surface morphology. Wavelet analysis also provides information about irregularity of topography (Stępień, 2014). This calculation is based on waveform functions for analyzing of surface features. Results of mathematical processing of AFM data, such as wavelet spectra, fractal dimension, or statistical parameters are the instruments for qualitative description of topography.

TABLE 1 The basic properties of the height values distribution (including its variance, skewness and kurtosis) of the surface samples, for scanning square areas of 30 μm × 30 μm

The basic properties of the height values distribution of the surface samples	Sample 1–30 × 30 61 μm per sec	Sample 1–30 × 30 314 μm per sec	Sample 2–30 × 30 61 μm per sec	Sample 2–30 × 30 314 μm per sec	Sample 3–30 × 30 61 μm per sec	Sample 3–30 × 30 314 μm per sec
Ra (Sa) (nm)	0.294	0.293	0.191	149.7	0.401	0.414
Rms (Sq) (nm)	0.340	0.340	0.228	178.4	0.464	0.479
Skew (Ssk) (-)	0.112	0.107	0.281	0.0756	−0.114	−0.113
Kurtosis (Sku) (-)	−1.14	−1.12	−0.75	−0.811	−1.16	−1.18
Inclination θ (°)	2.3	2.4	1.6	1.2	3.1	3.0
Inclination φ (°)	86.3	86.5	71.1	65.3	84.4	92.9

The purpose of this study is investigation of parameters (Appendix) which could be applied for estimation of optimal measurement conditions. To reach the aim, we carry out imaging of the surfaces at two different frequencies of scanning. The actuality of this study is caused by the fact the physics of surface and estimation of surface condition (including geometrical appearance, etc.) is one of the main problems of modern nano-electronics.

2 | MATERIALS AND METHODS

2.1 | Materials

The measurements were carrying out on former calibration grades. They are damaged by time and manipulation during measurements. Nevertheless, there is a periodic structure on the surface. Such periodical structures are also useful for study of the tip-surface geometrical contact (Dremov, Fedoseev, Fedorov, & Grebenko, 2015). Sample 1 has cubic structures on the surface, Sample 2 represents some peaks with sharp ends, and Sample 3 has parallel lines on the surface.

2.2 | AFM analysis

The measurements were done by AFM Ntegra Prima (NT-MDT, Moscow, Russia). HA-NC "fresh" probes were used of the same producer. The measurements were performed on scanning areas of 30 × 30 μm^2. Similar image size and resolution were for every measurement. The measurements were done at two different scan rates. To assure the same conditions of measurements, the experiment was carry out without any changes in microscopy setup, at the same ambient conditions. The microscope was turned on for an hour to have stabilized laser signal. We avoid any filtering. Scanning was done with closed loop scanner in semi-contact mode with generator amplitude 0.6 V, setpoint about 12 V and feedback gain is 0.5.

To estimate only influence of the scanning rate, the measurements were carried out at the same conditions at the same material from the same producers: the only difference in samples is the shape of surface features. Working frequency of probes corresponds to the data of producer (138 kHz), tip curvature radius is about 10 nm, 320MHz DSP was used at measurements.

P-I parameters were chosen before beginning of scanning after approach of the tip to the sample surface and were similar for every measurement: maximum signal from photo detector and feedback gains when at the same time no feedback oscillations occur. Using of similar parameters was possible because of similar cantilevers and the same material of the scanning samples.

Tip shape is one of the factors that define resolution of AFM imaging. Nevertheless, tip convolution loss relevance for large scale images. We did not consider the influence of the tip size on the geometry of the topography because scan area is 3E4 times tip radius, pixel size 100 times the tip radius.

3 | RESULTS

Chosen scanning rates are 61 μm per sec and 314 μm per sec. The representative 3D topographic AFM images, for scanning square area of 30 × 30 μm^2, of the Samples 1, 2, and 3 are shown in Figure 1. The

TABLE 2 The fractal dimensions (D) with coefficients of correlation (R^2) determined by the cube counting method, based on the linear interpolation type, of the samples

Parameters	Sample 1–30 × 30 61 μm per sec	Sample 1–30 × 30 314 μm per sec	Sample 2–30 × 30 61 μm per sec	Sample 2–30 × 30 314 μm per sec	Sample 3–30 × 30 61 μm per sec	Sample 3–30 × 30 314 μm per sec
D	2.07	2.10	2.04	2.03	2.06	2.02
R^2	0.991	0.992	0.991	0.991	0.991	0.991

result of surface texture analysis is presented at Figures 2–4. Analyzing the roughness is presented in the Tables 1 and 2.

The basic properties of the height values distribution of the surface samples (including its variance, skewness, and kurtosis) are shown in Table 1, for scanning square areas of 30 μm × 30 μm.

The statistical properties of the individual points can be characterized with the height distribution (which belong to the first-order statistical quantities), and are computed. These can be computed as noncumulative (i.e., densities).

The sensibility of statistical parameters to image distortion is observed (Table 1). The morphology of three samples is characterized by statistical parameters (Klapetek, Nečas, & Anderson, 2017). The highest values of: Sa, Sq, | Ssk |, and | Sku | were obtained in the Samples 3 than the Samples 1 and 2.

In Figure 2 are shown the height distribution functions for samples (Figure 1) (where *p* is the corresponding quantity). The graph of height distribution function differs with scanning rate for every sample and becomes broader at high scanning rate. It could be caused by changes in sizes of scanning surface features or/and appearance new elements on the surface (artifacts).

Fractal dimensions were used for quantitative description the surface. These values (*D*) contain information about complexity of the samples surface. The lager values of *D*, the higher the surface roughness. The fractal dimension *D* of 3D surfaces, as a measure of global scaling property. Fractal dimension is lower for the Sample 2 and it changes just by 0.01. For the samples with higher *Df*, the difference in dependence with scanning rate is 0.03 and 0.04.

The mutual relationship of two points on the surface can be characterized using the second-order statistical quantities; these functions are namely the autocorrelation function (*G*), the height-height correlation function (*H*), and the radial power spectral density function (radial PSDF).

ACF has higher values for the images of Samples 1 and 3 obtained in higher scanning rate. This function characterizes the correlation of the similar surface features; it remains almost unchanged for the Sample 2. HHCF graphs characterize lateral distribution of surface features —the distance of features high correlation. It growths for the Samples 1 and 3 with scanning rate and remains the same for the Sample 2 with the lowest *D*.

For the Sample 1 with the highest *D*, the PSDF is characterized by additional peaks at high scanning rate which are associated with local highs of texture.

4 | DISCUSSION

Very fast or too slow scanning rates provide non-reliable data. The estimation of chosen scanning rate could be carry out by processing and evaluation of surface parameters. Preliminary information about nature of sample surface can be helpful for choice of correct scanning rate.

In this study, we used samples with different texture of the surface. Increasing of scanning rate for the Sample 2 with lower RMS and lower fractal dimension did not make any drastic changes in surface appearance (Figure 1c,d). Scanning of the topography with high fractal dimension at high speed caused distortion of image features (Figure 1a, b,e,f).

RMS statistics shows changing of surface roughness (Table 1). But this is not sufficient for estimation of changes in imaging of texture. Influence of measurement parameters on the spectral content of the scanned image is also studied by ACF, HHCF, PSDF functions.

Knowing of fractal dimension allows estimation of noise at the image. There is a relationship between fractal dimension and scanning rate. Surface analysis attributes to product quality improvement (Ţălu, 2015). Comparison of the surface geometrical parameters with data of etalon samples could be a solution for automatic tool calibration.

Some image artifacts which impact the calculation and caused errors in studied surface metrics: distortion of image features due to different type of noise (acoustic, electronic, environmental); bad definition of edges: changing of the scanning rate make different contribution to the result data in dependence on surface structure; fake features: appearance of the elements which do not associate with real image topography. The wrong choice of the scanning rate influences both useful data imaging and adds artifacts.

5 | CONCLUSION

The aim of our work is to show how to enhance the characterization of topography on the basis of data processing. Besides standard applications, calibration samples could be used for right setup of measurement conditions.

We have measured three the samples with different topography by AFM at different scanning rate. Impact of scanning rate on the surfaces with various geometrical textures is investigated. Statistical and fractal analyses are presented for characterization of surface morphometrics. It helps to compute and estimate the distortion of images due to scanning rate and to take over the control on measurement.

Our results suggest that AFM, the statistical surface roughness parameters and fractal analysis may provide additional insight into the nature of the physical transformations that take place in the interface sample-tip. Thus, statistical surface roughness parameters and fractal analysis could provide useful information for the further development of calibration systems. Analysis of the data shows that rough surface demands lower scanning rates. Measurement of surfaces with lower fractal dimension could be performed with higher rate of scanning. The approach could find an application for not only calibration of microscope by geometrical sizes of features but also it could be used for right choice of scanning parameters, taking into consideration the geometry of the sample.

ACKNOWLEDGMENTS

Research described in the paper was financially supported by the Ministry of Education, Youth and Sports of the Czech Republic under the project CEITEC 2020 (LQ1601), by the Grant Agency of the Czech Republic under no. GACR 15-05259S and by the National Sustainability Program under grant LO1401. For the research, infrastructure of the SIX Center was used.

DISCLOSURE OF INTERESTS

Neither author has a financial or proprietary interest in any material or method mentioned.

CONFLICT OF INTERESTS

The authors declare that they have no competing interests.

ORCID

Dinara Sobola http://orcid.org/0000-0002-0008-5265

REFERENCES

Arman, A., Ţălu, Ş., Luna, C., Ahmadpourian, A., Naseri, M., & Molamohammadi, M. (2015). Micromorphology characterization of copper thin films by AFM and fractal analysis. *Journal of Materials Science: Materials in Electronics*, *26*(12), 9630–9639.

Benlia, B., & Yalın, C. (2017). Theinfluenceofsilverandcopperionsontheantibacterial activityandlocal electrical properties of single sepiolite fiber: A conductive atomic force microscopy (C-AFM) study. *Applied Clay Science*, *146*, 449–456.

Berezina, S., Il'icheva, A. A., Podzorova, L. I., & Ţălu, Ş. (2015). Surface micromorphology of dental composites [CE-TZP] - [AL_2O_3] with Ca^{+2} modifier. *Microscopy Research and Technique*, *78*, 840–846.

Canet-Ferrer, J., Coronado, E., Forment-Aliaga, A., & Pinilla-Cienfuegos, E. (2014). Correction of the tip convolution effects in the imaging of nanostructures studied through scanning force microscopy. *Nanotechnology*, *25*(39), 395703.

Dallaeva, D., Ţălu, Ş., Stach, S., Škarvada, P., Tománek, P., & Grmela, L. (2014). AFM imaging and fractal analysis of surface roughness of AlN epilayers on sapphire substrates. *Applied Surface Science*, *312*, 81–86.

Dallaeva, D., Tomanek, P., Prokopyeva, E., Kaspar, P., Grmela, L., & Skarvada, P. (2015). AFM imaging of natural optical structures. In J. Kovacicinova & T. Vit (Eds.), *Proceedings of SPIE. Vol. 9442. Optics and Measurement Conference 2014* (944209). Liberec, Czech Republic: SPIE. https://doi.org/10.1117/12.2176720

Dallaeva, D., Tomanek, P., Skarvada, P., & Grmela, L. (2015). Realization of microscale detection and localization of low light emitting spots in monocrystalline silicon solar cells. In P. Tomanek, D. Senderakova, & P. Pata (Eds.), *Proceedings of SPIE: Vol. 9450. Photonics, Devices, And Systems* VI (94501O). Prague, Czech Republic: SPIE. https://doi.org/10.1117/12.2069504

Dremov, V., Fedoseev, V., Fedorov, P., & Grebenko, A. (2015). Fast and reliable method of conductive carbon nanotube-probe fabrication for scanning probe microscopy. *Review of Scientific Instruments*, *86*, 053703.

Elenkova, D., Zaharieva, J., Getsova, M., Manolov, I., Milanova, M., Stach, S., & Ţălu, Ş. (2015). Morphology and Optical Properties of SiO_2-Based Composite Thin Films with Immobilized Terbium(III) Complex with a Biscoumarin Derivative. *International Journal of Polymer Analysis and Characterization*, *20*(1), 42–56.

Goerke, D., & Willner, K. (2008). Normal contact of fractal surfaces—Experimental and numerical investigations. *Wear*, *264*, 589–598.

Gołek, F., Mazur, P., Ryszka, Z., & Zuber, S. (2014). AFM image artifacts. *Applied Surface Science*, *304*, 11–19.

Hantschel, T., Tsigkourakos, M., Zha, L., Nuytten, T., Paredis, K., Majeed, B., & Vandervorst, W. (2016). Diamond scanning probes with subnanometer resolution for advanced nanoelectronics device characterization. *Microelectronic Engineering*, *159*, 46–50.

Jradi, Kh., Schmitt, M., & Bistac, S. (2012). Influence of the surface chemistry on the nanotribological behavior of (AFM tip/graphite) couples. *Applied Surface Science*, *258*, 4687–4697.

Klapetek, P., Nečas, D., & Anderson, C. (2017). Gwyddion 2.37 software. Copyright © 2004–2007, 2009–2014. Retrieved from http://gwyddion.net

Knotek, P., Chanova, E., & Rypacek, F. (2013). AFM imaging and analysis of local mechanical properties for detection of surface pattern of functional groups. *Materials Science and Engineering: C*, *33*(4), 1963–1968.

Koblischka, M. R., Hartmann, U., & Sulzbach, T. (2003). Improvements of the lateral resolution of the MFM technique. *Thin Solid Films*, *428*, 93–97.

Méndez, A., González-Arellano, S. G., Reyes-Vidal, Y., Torres, J., Ţălu, Ş., Cercado, B., & Trejo, G. (2017). Electrodeposited chrome/silver particles (Cr/AgPs) composite coatings: Characterization and antibacterial activity. *Journal of Alloys and Compounds*, *710*, 302–311.

Méndez, A., Reyes, Y., Trejo, G., Stępień, K., & Ţălu, Ş. (2015). Micromorphological characterization of zinc/silver particle composite coatings. *Microscopy Research and Technique*, *78*, 1082–1089.

Miccio, L. A., Kummali, M. M., Schwartz, G. A., Alegría, Á., & Colmenero, J. (2014). AFM based dielectric spectroscopy: Extended frequency range through excitation of cantilever higher eigenmodes. *Ultramicroscopy*, *146*, 55–61.

Moscatello, J. P., Castaneda, Ch, V., Zaidi, A., Cao, M., Usluer, O., ... Aidala, K. E. (2017). Time-resolved kelvin probe force microscopy to study population and depopulation of traps in electron or hole majority organic semiconductors. *Organic Electronics*, *41*, 26–32.

Naseri, N., Solaymani, S., Ghaderi, A., Bramowicz, M., Kulesza, S., Ţălu, Ş., ... Ghasemi, S. (2017). Microstructure, morphology and electrochemical properties of Co nanoflake water oxidation electrocatalyst at micro- and nanoscale. *RSC Advances*, *7*, 12923–12930.

Poljacek, S. M., Risovic, D., Furic, K., & Gojo, M. (2008). Comparison of fractal and profilometric methods for surface topography characterization. *Applied Surface Science*, *254*, 3449–3458.

Ramazanov, S., Ţălu, Ş., Sobola, D., Stach, S., & Ramazanov, G. (2015). Epitaxy of silicon carbide on silicon: Micromorphological analysis of growth surface evolution. *Superlattices and Microstructures*, *86*, 395–402.

Reyes-Vidal, Y., Suarez-Rojas, R., Ruiz, C., Torres, J., Ţălu, Ş., Méndez, A., & Trejo, G. (2015). Electrodeposition, characterization, and antibacterial activity of zinc/silver particle composite coatings. *Applied Surface Science*, *342*, 34–41.

Rodriguez, R. D., Lacaze, E., & Jupille, J. (2012). Probing the probe: AFM tip-profiling via nanotemplates to determine Hamaker constants from phase–distance curves. *Ultramicroscopy*, *121*, 25–30.

Ryu, S. R., Ram, S. D. G., Lee, S. J., Cho, H., Lee, S., Kang, T. W., ... Woo, Y. (2015). Vertical current-flow enhancement via fabrication of GaN nanorodp–n junction diode on graphene. *Applied Surface Science*, *347*, 793–798.

Shen, J., Zhang, D., Zhang, F.-H., & Gan, Y. (2017). AFM tip-sample convolution effects for cylinder protrusions. *Applied Surface Science*, *422*, 482–491.

Šik, O., Bábor, P., Škarvada, P., Potoček, M., Trčka, T., Grmela, L., & Belas, E. (2016). Investigation of the effect of argon ion beam on CdZnTe single crystals surface structural properties. *Surface and Coatings Technology*, *306*, 75–81.

Skarvada, P., Skvarenina, L., Tomanek, P., Sobola, D., Macku, R., Brustlova, J., ... Smith, S. (2016). Multiscale experimental characterization of solar cell defects. In J. Mullerova, D. Senderakova, L. Ladanyi, & L. Scholtz (Eds.), *Proceedings of SPIE: Vol. 10142. 20th Slovak-Czech-Polish Optical Conference on Wave and Quantum Aspects of*

Contemporary Optics (UNSP 101420U). Jasna, Slovakia: SPIE. https://doi.org/10.1117/12.2259884

Slattery, A. D., Blanch, A. J., Quinton, J. S., & Gibson, C. T. (2013). Efficient attachment of carbon nanotubes to conventional and high-frequency AFM probes enhanced by electron beam processes. *Nanotechnology*, *24*(23), 235705– 2313pp.

Stach, S., Dallaeva, D., Ţălu, Ş., Kaspar, P., Tománek, P., Giovanzana, S., & Grmela, L. (2015). Morphological features in aluminum nitride epilayers prepared by magnetron sputtering. *Materials Science-Poland*, *33*(1), 175–184.

Stach, S., Sapota, W., Ţălu, Ş., Ahmadpourian, A., Luna, C., Ghobadi, N., … Ganji, M. (2017). 3D Surface stereometry studies of sputtered TiN thin films obtained at different substrate temperatures. *Journal of Materials Science: Materials in Electronics*, *28*(2), 2113–2122.

Stępień, K. (2014). Research on a surface texture analysis by digital signal processing methods. *Tehnicki Vjesnik- Technical Gazette*, *21*(3), 485–493.

Ţălu, Ş. (2015). *Micro and nanoscale characterization of three dimensional surfaces. Basics and applications*. Cluj-Napoca, Romania: Napoca Star Publishing House.

Ţălu, Ş., Bramowicz, M., Kulesza, S., Solaymani, S., Shafikhani, A., Ghaderi, A., & Ahmadirad, M. (2016). Gold nanoparticles embedded in carbon film: Micromorphology analysis. *Journal of Industrial and Engineering Chemistry*, *35*, 158–166.

Ţălu, Ş., Stach, S., Raoufi, D., & Hosseinpanahi, F. (2015). Film thickness effect on fractality of tin-doped In_2O_3 thin films. *Electronic Materials Letters*, *11*(5), 749–757.

Ţălu, Ş., Stach, S., Zaharieva, J., Milanova, M., Todorovsky, D., & Giovanzana, S. (2014). Surface roughness characterization of poly(methylmethacrylate) films with immobilized Eu(III) β-Diketonates by fractal analysis. *International Journal of Polymer Analysis and Characterization*, *19*(5), 404–421.

Ţălu, S., Stępień, K., & Caglayan, M. O. (2015). Topographic characterization of unworn contact lenses assessed by atomic force microscopy and wavelet transform. *Microscopy Research and Technique*, *78*(11), 1026–1031.

Villarrubia, J. S. (1997). Algorithms for Scanned Probe Microscope Image Simulation, Surface Reconstruction, and Tip Estimation. *Journal of Research of the National Institute of Standards and Technology*, *102*(4), 425–454.

Yadav, R. P., Dwivedi, S., Mittal, A. K., Kumar, M., & Pandey, A. C. (2012). Fractal and multifractal analysis of LiF thin film surface. *Applied Surface Science*, *261*, 547–553.

Yeow, N., Taborb, R. F., & Garnier, G. (2017). Atomic force microscopy: From red blood cells to immunohaematology. *Advances in Colloid and Interface Science*. Retrieved from https://doi.org/10.1016/j.cis.2017.05.011

How to cite this article: Sobola D, Ţălu Ş, Solaymani S, Grmela L. Influence of scanning rate on quality of AFM image: Study of surface statistical metrics. *Microsc Res Tech*. 2017;80:1328–1336. https://doi.org/10.1002/jemt.22945

APPENDIX

Statistical analysis was carried out with the software SPSS 14 for Windows (Chicago, IL). One-way analysis of variance was applied for verification of results with Scheffé post hoc tests. A statistically significant difference P is assumed to be 0.05 or less. The statistical parameters were expressed by *Ra* (average roughness), *Rq* (root-mean-square deviation), *Ssk* (skew), *Sku* (kurtosis).

In detail, these parameters have following meaning (http://gwyddion.net):

- ***RMS* value of the height irregularities: this quantity is computed from data variance.**
- ***Ra* value of the height irregularities: this quantity is similar to *RMS* value with the only difference in exponent (power) within the data variance sum. As for the *RMS*, this exponent is $q = 2$, the *Ra* value is computed with exponent $q = 1$ and absolute values of the data (zero mean).**
- **Height distribution skewness: computed from third central moment of data values.**
- **Height distribution kurtosis: computed from fourth central moment of data values.**
- **Mean inclination of facets in area: computed by averaging normalized facet direction vectors.**
- **Variation, which is calculated as the integral of the absolute value of the local gradient.**

Appendix 2
WOS: 000489301300020

sciendo COMMUNICATIONS

Journal of ELECTRICAL ENGINEERING, VOL 70 (2019), NO-7S, 132–136

Characterization of nanoblisters on HOPG surface

Dinara Sobola*, Nikola Papež*, Rashid Dallaev*, Shikhgasan Ramazanov, Dušan Hemzal*** , Vladimír Holcman***

We report on influence of the surface functionalization on the properties of highly oriented pyrolytic graphite. The samples were processed in nitric acid and characterized by XPS, Raman and EDX spectroscopies, AFM, SEM and optical microscopy. It is shown that interaction of nitric acid with the surface of HOPG leads to two types of reactions: oxidation of the graphite and intercalation of the nitrate ions at the blistered areas.

K e y w o r d s: graphite, nitric acid, surface, delamination, topography

1 Introduction

Under normal conditions, graphite is the most stable allotropic form of carbon. Variation of its physical and chemical properties define the application range of graphite from pencil leads to cutting-edge calibration etalons in scientific applications. Thermal characteristics of graphite make it interesting for aerospace applications [1]. Intercalation of compounds can further spread properties of graphite and increase is application potential.

Both HOPG (highly oriented pyrolytic graphite) and HAPG (highly annealed pyrolytic graphite) exhibit pronounced layered structure. HOPG consists of hexagonal carbon planes situated in ABAB positions. Due to Van der Waals bonding between the planes this material is utilized for study and preparation of graphene structures. The interplanar distance between layers can be changed by intercalation of metals.

Graphene nanoblisters and nanobubbles are partially delaminated areas of one or several graphite layers. Both can be prepared on graphite itself or on interfaces of graphite with substrates from other materials. The nanobubbles are of interest because they can trap molecules from gases [2]. There are several methods of graphite nanobubbles formation on HOPG surface: pure chemical, electrochemical, plasma processing, *etc* [3]. Formation of blisters consists of penetration of the reagent through defects into near-surface layers and oxidation of graphite. In result, formation and dissociation of carbonic acid leads to blistering.

Braking of interplanar bonds at HOPG near-surface area and appearance of round-shaped blisters were reported before [4]–[6]. Our study contributes to this field by confirmation of the theoretical work of Tang and Cao [7] about stronger adsobtion of NO_3 in comparison to other nitrogen oxides. The NO_3 anion could be detected by Raman spectrsocopy at the blistered areas. We also demonstrate by XPS and Raman spectroscopies presence of NH_2 group whish is important for surface functionalization for biomedical application [8].

Appearance of blisters, delamination and "bubbles" could also occur during films deposition using carbon materials as substrates. Since control of the surface condition of the substrate is important part of deposition technologies [4, 5], modified carbon surfaces are thus of interest also for growth control during deposition of thin films [11].

2 Experiment

HOPG samples of ZYB quality (purchased from TipsNano OÜ) were exfoliated by tape and exposed to 65% nitric acid (HNO_3) under ambient conditions for 8 minutes. After the exposition, the samples were washed using demineralized water. Optical imaging of the samples before treatment and after treatment is shown in Fig. 1. The position of AFM probe is shown in Fig. 1(a).

The obtained surfaces were studied using atomic force microscopy (AFM) in semi-contact mode in order to not damage the surface features [7, 8]. The blistered areas tend to form "bubbles" on the surface with height up to 1 μm (see Fig. 2). It was suggested by Burgess at al. [14] that the blistering occurs due to functionalization of the surface defects by oxygen-containing bonds [15].

The blistered areas were also observed by SEM (scanning electron microscopy): maximum diameter of the nanobubbles was up to 3 μm (see Fig, 3).

*Department of Physics, Faculty of Electrical Engineering and Communication, Brno University of Technology, Technick 2848/8, 616 00 Brno, Czech Republic, nikola.papez@vutbr.cz, **Faculty of Physics, Dagestan State University, 367015 Makhachkala, st. M. Gadjieva 43-a, Dagestan Republic, Russia, ***Department of Condensed Matter Physics, Faculty of Science, Masaryk University, Kotlářská 267/2, 611 37 Brno, Czech Republic

DOI: 10.2478/jee-2019–0055, Print (till 2015) ISSN 1335-3632, On-line ISSN 1339-309X

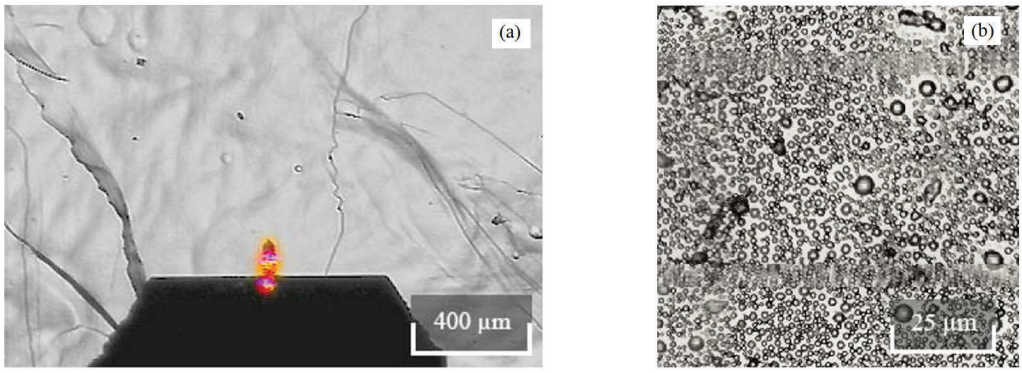

Fig. 1. Optical images: HOPG (ZYB) surface: (a) – before and, (b) – after 8 minutes of processing by HNO_3

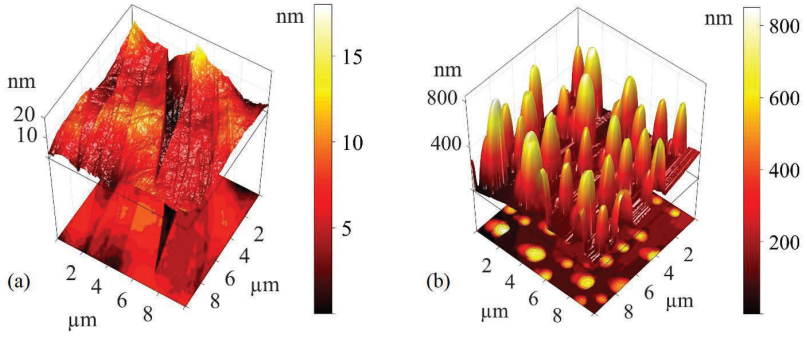

Fig. 2. AFM images: HOPG (ZYB) surface: (a) – before, and (b) – after 8 minutes processing in HNO_3.

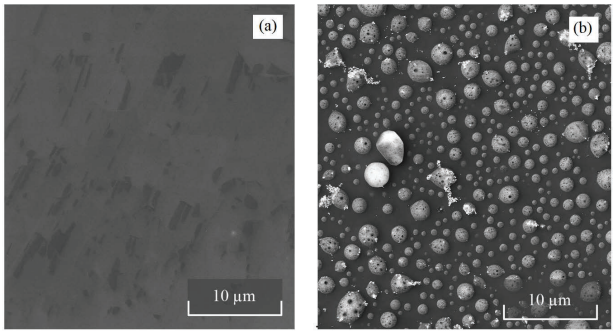

Fig. 3. SEM images: HOPG (ZYB) surface: (a) – before, and (b) – after 8 minutes of processing by HNO_3

Concerning chemical analysis, XPS showed presence of several peaks after treatment of HOPG surface with nitric acid (see Fig. 4). The N1s nitrogen peak occurring at $\sim$400 eV is usually assigned to $C-NH_2$ bond and its appearance corresponds with theory [14]. However, only 2 minutes of etching by 5 keV argon ions is sufficient to almost completely remove N1s peak, Fig. 4(b). It happens because of preferential etching of nitrogen which occurs by Ar irradiation. The other peak that emerged after HNO_3 treatment is the oxygen peak O1s at 532.4 eV corresponding to the C-O bond. To remove the O1s peak entirely, much longer Ar exposition would be required: even after 20 minutes of etching remnants of this peak persist, Fig. 4(c). Ion beam etching was performed in situ in the XPS chamber. The samples were not exposed to air in order to avoid influence of atmospheric oxygen to the surface condition.

Additionally, EDS (Energy Dispersive X-Ray Spectroscopy) was used for determination of oxygen abundance in the near-surface area. Although EDS did not prove the presence of nitrogen (which was observed by XPS due to its higher sensitivity to surface condition), oxygen content in the measured samples increased from 0.59 up to 1.02 atomic % after treatment.

The amount of oxygen increased twice after treatment, which confirms redox reaction between HOPG and HNO_3. First, surfactant elements from the acid create chemical bonds with graphite surface during reactions:

$$C + 4HNO_3 \longrightarrow H_2CO_3 + 4NO_2\,.$$

Subsequently, the carbonic acid instantly decomposes into carbon dioxide and water:

$$C + 4HNO_3 \longrightarrow CO_2 + 2H_2O + 4NO_2\,.$$

The produced stress occurs between the reacted near-surface area and the rest of the sample. The delamination of the layers and formation of blisters occurs where Van der Waals bonds are broken. Finally, Raman spectroscopy is widely used for characterization of carbon materials. We used Renishaw InVia spectrometer with laser power of 1 mW and wavelength 532 nm [16]. The observed Raman peaks (see Fig. 5) correspond to graphite intercalation

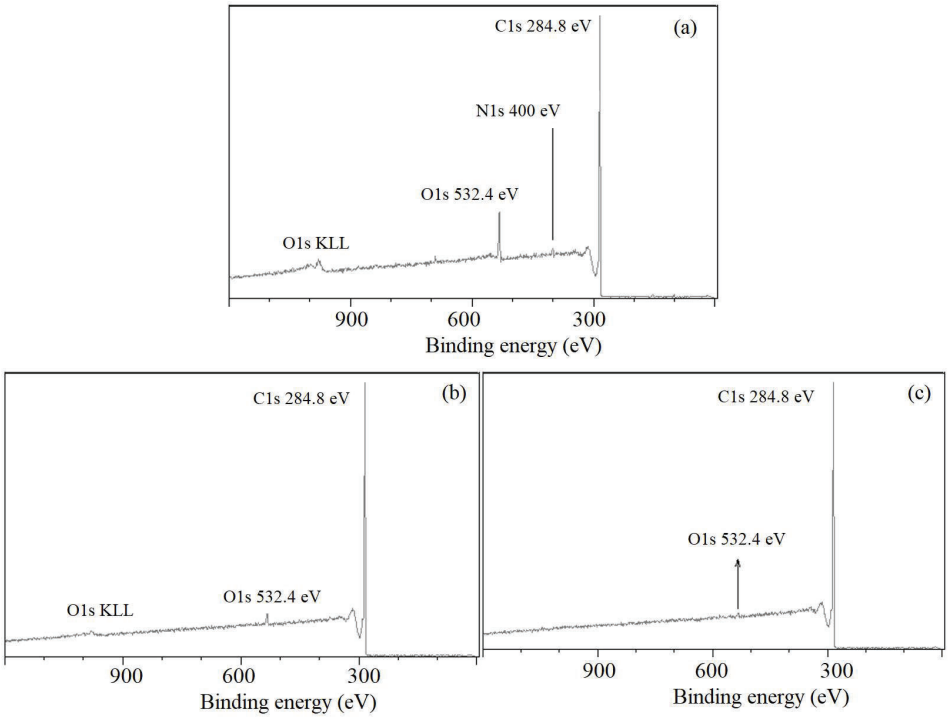

Fig. 4. Wide XPS spectra of HOPG treated with HNO_3 during 8 minutes: (a) – before Ar etching, (b) – 2 min Ar etching, and (c) – 20 min Ar etching

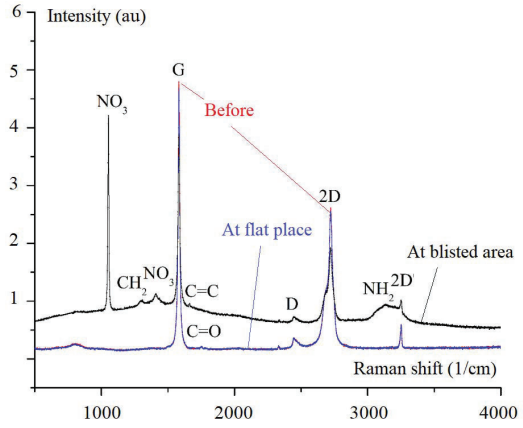

Fig. 5. Raman spectra: HOPG (ZYB) surface before and after 8 minutes of processing by HNO_3

compounds. According to Dunaev and Shapoev [17] the intercalation process could be presented as:

$$2HNO_3\ _{adsorbed} \longrightarrow H_2O + NO_3^- + NO_2^+\ _{adsorbed}$$

$$NO_2^+\ _{adsorbed} + C \longrightarrow NO_2\ _{adsorbed} + C^+$$

$$NO_2\ _{adsorbed} \longrightarrow NO_2\ _{gas}$$

$$nC^+ + NO_3^- + xHNO_3 \longrightarrow C_n^+NO_3^-\,xHNO_3$$

The main differences in comparison to pristine HOPG are in spectra from the blister areas. The common areas are observed at 1582 cm^{-1} and 2721 cm^{-1} which are positions of G and 2D peaks of HOPG [18]. Doublet of 2450 cm^{-1} and 3248 cm^{-1} is assigned to D and 2D modes of HOPG, correspondingly [19]. The blister areas show, however, additional features:

- peak at 1053 cm^{-1} refers to macro-cation NO_3 trapped between the graphite layers and the rest of non-dissociated HNO_3 [20],
- peak at 1300 cm^{-1} is connected with transverse vibrations of CH_2 group [21],
- appearance of the 1409 cm^{-1} peak can be attributed to incorporated nitrate anion [22],
- features of C=C and C=O stretching modes are noted by 1660 cm^{-1} and 1748 cm^{-1} peaks, correspondingly [23],
- peak at 3130 cm^{-1} occurs due to NH_2 groups [24].

Thus, the Raman measurement confirms presence of bonds which result from intercalation and oxidation reactions [25]. In order to check the inner structure of the surface features which occurs after the acid treatment the depth-scan Raman measurement was done. The largest blister on the surface was funded by optical microscope for this aim, Fig. 6(a). Contrasted images for NO_3 peak and G-peak at the surface, in middle(and at the bottom are investigated (Fig. 6(b)-(d). The results indicate presence of NO_3^- ions and intensive G-peak on the surface. G-peak decreases during scanning inside the blisters and growths with approaching to the HOPG bulk. The content of nitrogen oxide is higher in the middle of the blister. Peak ratio demonstrates presence of several carbon layers on the surface of the delaminated area and higher amount of the nitrogen compounds (NO_3 and NH_2) below them.

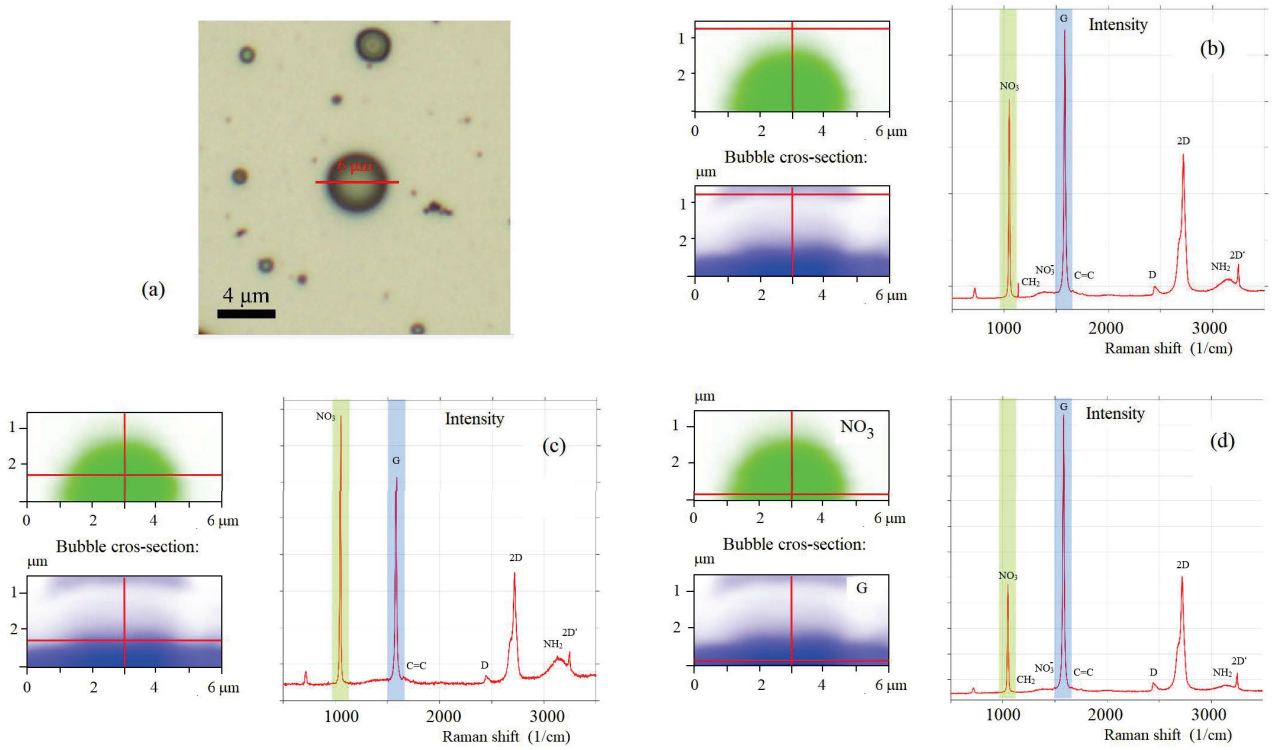

Fig. 6. Raman spectra of the blistered area in depth: (a) – optical top view of the blister for Raman depth-scan, (b) – blister cross-section, top view, (c) – bBlister cross-section, middle view, and (d) – blister cross-section, bottom view

3 Conclusion

Treatment of the surface by HNO_3 created blistered areas. AFM, SEM and optical images demonstrate formation of nanoblisters with different size but similar shape. According to EDS, there are changes in oxygen abundance in the near-surface area after processing by HNO_3.

In summary, nitric acid attacks graphite as oxidant by taking forth an electron (three electrons participate in plain covalent bonding). It is expected that CO_2, NO_2 and water occur in result of reaction between HNO_3 and graphite. Intercalated elements consist of products of redox reactions between graphite and HNO_3. We observed the presence of electron acceptor NO_3^- at the blistered areas. XPS and Raman data confirmed surface functionalization by NH_2 group.

All these defects influence physical and chemical properties of the surface and also affect the performance of the material in its potential applications. In particular, formation of blisters should be considered when HOPG is used as a substrate for epitaxy and heterostructures preparation.

Acknowledgements

Research described in the paper was financially supported by the Ministry of Education, Youth and Sports of the Czech Republic under the project CEITEC 2020 (LQ1601), by the National Sustainability Program under grant LO1401, and by Internal Grant Agency of Brno University of Technology, Grant No. FEKT-S-17-4626. For the research, infrastructure of the SIX Center was used. Part of the work was carried out with the support of CEITEC Nano Research Infrastructure (MEYS CR, 2016-2019).

References

[1] E. Ancona and R. Y. Kezerashvili, "Temperature restrictions for materials used in aerospace industry for the near-Sun orbits", *Acta Astronaut.*, 2017.

[2] E. Khestanova, F. Guinea, L. Fumagalli, A. K. Geim, and I. V. Grigorieva, "Universal shape and pressure inside bubbles appearing in van der Waals heterostructures", *Nat. Commun.*, 2016.

[3] L. Liu, M. Qing, Y. Wang, and S. Chen, "Defects in Graphene: Generation, Healing, and Their Effects on the Properties of Graphene: A Review", *J. Mater. Sci. Technol.*, 2015.

[4] S. Yang, P. Tsai, E. S. Kooij, A. Prosperetti, H. J. W. Zandvliet, and D. Lohse, "Electrolytically generated nanobubbles on highly orientated pyrolytic graphite surfaces", *Langmuir*, 2009.

[5] E. Bouleghlimat, P. R. Davies, R. J. Davies, R. Howarth, J. Kulhavy, and D. J. Morgan, "The effect of acid treatment on the surface chemistry and topography of graphite", *Carbon N. Y.*, 2013.

[6] O. V. Sinitsyna, G. B. Meshkov, A. V. Grigorieva, A. A. Antonov, I. G. Grigorieva, and I. V. Yaminsky, "Blister formation during graphite surface oxidation by Hummers method", *Beilstein J. Nanotechnol.*, 2018.

[7] S. Tang and Z. Cao, "Adsorption of nitrogen oxides on graphene and graphene oxides: Insights from density functional calculations", *J. Chem. Phys.*, 2011.

[8] H. J. Kim et al., "Synthesis and characteristics of NH 2-functionalized polymer films to align and immobilize DNA molecules", *Nanoscale Res. Lett.*, 2012.

[9] M. M. Koc, M. J. McNally, K. von Haeften, and M. J. Watkins, "AFM induced self-assembling and self-healing mechanism of silicon oxide nanoparticle linear array domains templated on Moir superlattice patterns on HOPG", *Surf. Sci.*, 2019.

[10] M. Kettner, C. Stumm, M. Schwarz, C. Schuschke, and J. Libuda, "Pd model catalysts on clean and modified HOPG: Growth, adsorption properties, and stability", *Surf. Sci.*, 2019.

[11] R. Shikhgasan, T. Stefan, S. Dinara, S. Sebastian, and R. Guseyn, "Epitaxy of silicon carbide on silicon: Micromorphological analysis of growth surface evolution", *Superlattices Microstruct.*, vol. 86, pp. 395–402, 2015.

[12] D. Sobola, S. Talu, S. Solaymani, and L. Grmela, "Influence of scanning rate on quality of AFM image: Study of surface statistical metrics", *Microsc. Res. Tech.*, vol. 80, no. 12, 2017.

[13] S. Talu, D. Sobola, and N. Papež, "Analysis and Recommendations for Education Process of Experts in the Field of Scanning Probe Microscopy", *DEStech Trans. Soc. Sci. Educ. Hum. Sci.*, vol. 0, no. aetms, 2017.

[14] R. Burgess et al., "The functionalisation of graphite surfaces with nitric acid: Identification of functional groups and their effects on gold deposition", *J. Catal.*, 2015.

[15] S. Talu, D. Sobola, S. Solaymani, R. Dallaev, and J. Brüstlová, "Scale-depended Choice of Scanning Rate for AFM Measurements", *DEStech Trans. Comput. Sci. Eng.*, no. cnai, 2018.

[16] N. Papež et al., "Degradation analysis of GaAs solar cells at thermal stress", *Appl. Surf. Sci.*, 2018.

[17] A. S. A. Dunaev, "Prolific Family of Carbon Materials", Online: http://www.nanometer.ru.

[18] P. H. Tan, Y. M. Deng, Q. Zhao, and W. C. Cheng, "The intrinsic temperature effect of the Raman spectra of graphite", *Appl. Phys. Lett.*, 1999.

[19] P. H. Tan, Y. M. Deng, and Q. Zhao, "Temperature-dependent Raman spectra and anomalous Raman phenomenon of highly oriented pyrolytic graphite", *Phys. Rev. B - Condens. Matter Mater. Phys.*, 1998.

[20] R. L. F. J. Theo Kloprogge, D. Wharton, L. Hickel, "Infrared and Raman study of interlayer anions CO3 2- , NO3 - , SO4 2- and ClO4 - in Mg/Al- hydrotalcite", *Am. Mineral.*, 2002.

[21] R. W. C. G. Wood, "Raman Spectra of a Series of Normal Alcohols and Other Compounds", vol. 42, no. 1, pp. 386–393, 1932.

[22] V. Rives, "Layered Double Hydroxides: Present and Future", 2011.

[23] P. Meksiarun, N. Spegazzini, H. Matsui, K. Nakajima, Y. Matsuda, and H. Satoa, "In vivo study of lipid accumulation in the microalgae marine diatom Thalassiosira pseudonana using Raman spectroscopy", *Appl. Spectrosc.*, 2015.

[24] A. L. M. B. De Carvalho, S. M. Fiuza, J. Tomkinson, L. A. E. B. De Carvalho, and M. P. M. Marques, "Pt(II) complexes with linear diamines-Part I: Vibrational study of Pt-diaminopropane", *Spectrosc. (New York)*, 2012.

[25] N. Papež et al., "Surface morphology after reactive ion etching of silicon and gallium arsenide based solar cells", *J. Phys. Conf. Ser.*, vol. 1124, pp. 041015, 2018.

Received 19 March 2019

Appendix 3
WOS: 000362603100047

Superlattices and Microstructures 86 (2015) 395–402

Contents lists available at ScienceDirect

Superlattices and Microstructures

journal homepage: www.elsevier.com/locate/superlattices

Epitaxy of silicon carbide on silicon: Micromorphological analysis of growth surface evolution

Ramazanov Shikhgasan [a,b], Ţălu Ştefan [c], Sobola Dinara [d,*], Stach Sebastian [e], Ramazanov Guseyn [a]

[a] SICLAB Limited Liability Company, 367030 Makhachkala, st. M. Yaragskogo 75, Dagestan Republic, Russia
[b] Dagestan State University, Faculty of Physics, 367015 Makhachkala, st. M. Gadjieva 43-a, Dagestan Republic, Russia
[c] Technical University of Cluj-Napoca, Faculty of Mechanical Engineering, Department of AET, Discipline of Descriptive Geometry and Engineering Graphics, 103-105 B-dul Muncii St., Cluj-Napoca 400641, Cluj, Romania
[d] Brno University of Technology, Faculty of Electrical Engineering and Communication, Physics Department, Technická 8, 616 00 Brno, Czech Republic
[e] University of Silesia, Faculty of Computer Science and Materials Science, Institute of Informatics, Department of Biomedical Computer Systems, ul. Będzińska 39, 41-205 Sosnowiec, Poland

ARTICLE INFO

Article history:
Received 14 April 2015
Received in revised form 3 July 2015
Accepted 10 August 2015
Available online 11 August 2015

Keywords:
Epitaxy
Silicon carbide epilayer
Atomic force microscopy
Magnetron sputtering
Substrate
Surface roughness
Fractal analysis

ABSTRACT

The main purpose of our research was the study of evolution of silicon carbide films on silicon by micromorphological analysis. Surface micromorphologies of Silicon Carbide epilayers with two different thicknesses were compared by means of fractal geometry. Silicon Carbide films were prepared on Si substrates by magnetron sputtering of polycrystalline target SiC in Ar atmosphere (99.999% purity). Synthesis of qualitative SiC/Si templates solves the questions of large diameter SiC single-crystal wafers formation. This technology decreases financial expenditure and provides integration of SiC into silicon technology. These hybrid substrates with buffer layer of high oriented SiC are useful for growth of both wide band gap materials (SiC, AlN, GaN) and graphene. The main problem of SiC heteroepitaxy on Si (1 1 1) is the large difference (~20%) of the lattice parameters. Fractal analysis of surface morphology of heteroepitaxial films could help to understand the films growth mechanisms. The 3D (three-dimensional) surfaces revealed a fractal structure at the nanometer scale. The fractal dimension (D) provided global quantitative values that characterize the scale properties of surface geometry.

1. Introduction

Silicon carbide (SiC) is one of the desirable materials for modern electronics because of the interesting properties combination. It can handle the high breakdown electric field [1], has a lattice structure very close to Gallium Nitride (GaN) [2,3], good thermal conductivity [4], high temperature and high wear resistance, high strength, chemical inertness at room temperatures [5,6].

* Corresponding author at: Brno University of Technology, Faculty of Electrical Engineering and Communication, Physics Department, Technická 8, 616 00 Brno, Czech Republic.
E-mail address: xdalla02@stud.feec.vutbr.cz (S. Dinara).

http://dx.doi.org/10.1016/j.spmi.2015.08.007
0749-6036/

Silicon carbide is a suitable material for a number of applications in electronic devices [7]: optoelectronics (solar cell [8], photodetector [3], light emitting diode [4]), and power-electronics [9] (Schottky diode, high speed switch [10]), buffer layer for GaN and AlN films fabrication [11].

Inexpensive substrates of silicon carbide are also essential for wide band gap materials fabrication in SiC-AlN system and consequent design of the power electronics on its basis [12]. It plays a role in graphene integration into modern technological base [13–15].

The standard method of semiconductor material fabrication can be uses for SiC growth, such as sublimation epitaxy [16], different modifications of chemical vapor deposition [2,3,10], solid phase epitaxial [17] and new method of magnetron sputtering [18].

The 3D surface micromorphology of epilayers is a very important parameter because all other properties – optical, electrical, and mechanical – stem from these and this should be studied and controlled.

The 3D surface micromorphology may be described in terms of its fractal geometry, which is a field of modern mathematics that uses non-integer dimensions to characterize the irregularity of a 3D complex surface geometry [19–22]. Furthermore, due to easy implementation, high precision and low computational time, the fractal analyses allow extracting different types of information from 3D complex surface characteristics, in contrast to traditional statistical parameters [23–25].

The 3D fractal surfaces possess the properties of continuity, non-differentiability, self-similar and self-affinity and can be quantitative estimated by fractal dimension (an intrinsic property of the surface, which is independent of the resolution of the instrument used) [26–28]. It indicates how much the fractal surface fills the 3D volume and represents the quantitative measure of 3D microstructure complexity [29,30].

Generally, the fractal dimension D of a surface is a non-integer value within the range $2 \leqslant D \leqslant 3$, where $D = 2$ (for ideally flat surfaces) and $D = 3$ (for surfaces with a rough that occupy all available volume) [31–33]. An increasing value of D indicates higher level of fractality, a more irregular shape of the surface roughness [19,34].

In the literature, there are many computing methods to estimate the fractal dimension based on different mathematical algorithms and specific calculations [19,22,31]. Several studies suggested a correlation between the different surface roughness parameters and the surface fractal dimension D [19,35]. Recently, there is a trend to use the fractal/multifractal analysis to characterize the 3D micromorphology of epitaxial films, enabling deeper insight into the potential of this theory for surface science. On the other hand, the fractal description of the surface should accurately reflect its characteristics, being compatible with different theoretical models for surface growth.

The objective of this study was to acquire qualitative and quantitative nano-scale data of the 3D surface micromorphology of SiC epilayers, through fractal analysis.

2. Materials and methods

2.1. Samples preparation

SiC films were prepared on the silicon substrate of the basis orientation (1 1 1), size of the substrates is 7 × 6 mm, and thickness is 380 μm. The films were obtained by magnetron sputtering of the polycrystalline SiC target in the Ar (99.999% purity).

Residual pressure in the processing chamber was 10^{-6} Torr, and the temperature of the substrate T_{sub} was 950÷1050 °C. Si substrates were cleaned in the HF solution in order to remove native oxide. This method allowed manufacturing of inexpensive and structural oriented SiC layers on Si substrates. The SiC/Si structures were prepared at the same conditions but with different growth time.

Between the prepared samples the SiC/Si structures were selected with thickness 120 nm (sample B-14) and 420 nm (sample B-37). Thickness of the films was measured by Linnik interferometer. Sample B-14 represented the beginning step of the film formation and Sample B-37 demonstrated Ostwald ripening. Technological parameters of both films preparation were the same except the growth time. The deposition rate was 5.2 nm/min.

2.2. Experimental and analytical methods

Phase analysis of SiC/Si was investigated by X-ray diffraction (XRD) using PANalytical Empyrean diffractometer with Cu Kα – radiation (λ_α = 1.5406 Å) (Fig. 1). There is a peak corresponding to SiC cubic modification in the range $2\theta = 35.70°$ as it is shown in Fig. 1. Comparison to 3C-SiC card-index data shows the difference ±0.0012°. Increasing of the film thickness leads to better structural perfection of the film and higher intensity of the peak.

Interplanar spacing of 3C-SiC epilayer is d_{hkl} = 2.513 Å, FWHM = 0.18° (sample B-37). Macrostresses decrease with increasing of film thickness of the growing layer (Fig. 1).

Values of FWHM were studied in different areas of the surface in order to evaluate the perfection of the films overall square the whole sample (Fig. 2). Size of X-ray spot was ∼60 μm. XRD data were measured four times by normal moving of the sample.

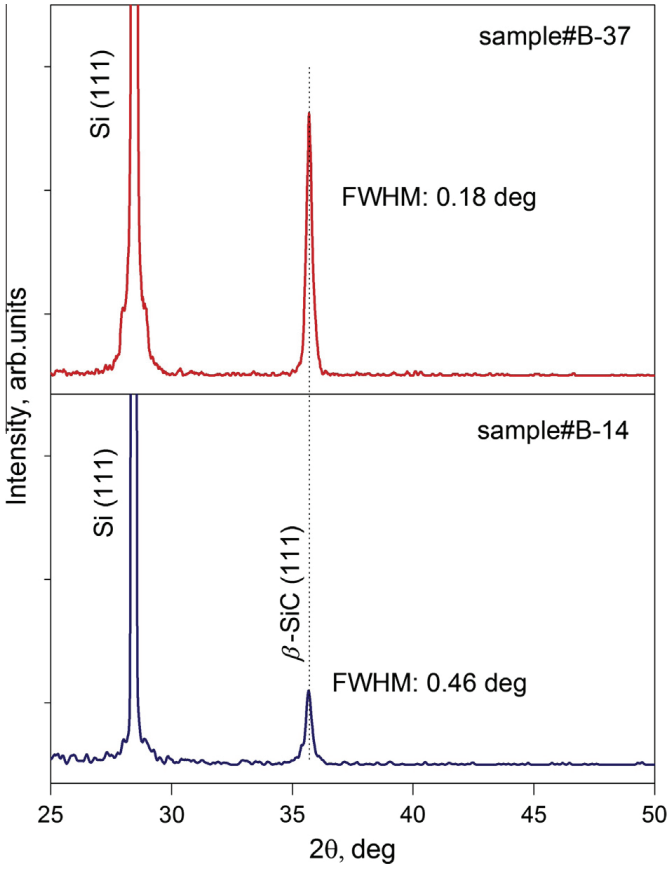

Fig. 1. Diffraction pattern of 3C-SiC/Si(1 1 1) structure of sample B-14 and sample B-37. The spectrum demonstrates peaks from the substrate Si(1 1 1) and from the prepared films (cubic modification). Peak in $2\theta = 35.70°$ corresponds to 3C-SiC (1 1 1).

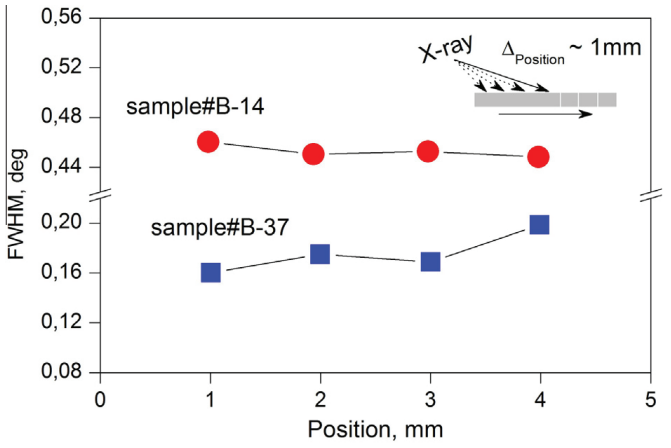

Fig. 2. Dependence of FWHM values on the position of analyzed area. Scheme of XRD measurements at every step (about ~1 mm) is shown in the corner of the figure.

Scattering of the structural parameter was larger for B-14 sample in comparison to B-37. It is caused by relaxation of elastic stresses in dependence of film thickness.

We consider surface evolution of the films by atomic force microscopy in order to understand the growth mechanism. 3D Surface and micromorphology of SiC/Si(1 1 1) structures were studied by Scanning Probe Microscope NTEGRA Prima (NT-MDT, Russia) in tapping mode, in air, at a scan rate of 1 Hz with a 256 × 256 pixels image definition over different square areas. For tapping mode, a silicon cantilever, Model NSG01 DLC (AFM «Golden» Silicon Probes) [36] with the following nominal specifications: resonant frequency 150 kHz, force constant 5.1 N/m, length 125 μm, width 30 μm and thickness 2 μm was used. The tip specifications were: tetrahedral shape, height 14 μm, tip curvature radius 6 nm, and cone angle at the apex 7–10°. All measurements were performed in the same laboratory, at room temperature (296 ± 1 K) and 50 ± 1% relative

humidity. The measurements were repeated four times for each sample on different reference areas, to validate the reproducibility of these features. Three-axis images of the samples surface are in Fig. 3.

SiC films grow as island films at heteroepitaxy in Vollmer – Weber growth mode (Fig. 3). Island growth occurs if there is a condition [37] $\sigma_s < \sigma_d + \sigma_{s\text{-}d} - \text{const} \cdot k_B T \ln(\xi + 1)$, (where σ_s is a free energy of substrate surface unit, σ_d is a free energy of adsorbate surface unit, $\sigma_{s\text{-}d}$ is a free energy of substrate-adsorbate surface unit, k_B is Boltzmann constant, ξ is a supersaturation parameter). In other case there is a layer growth.

As it shown in AFM images the small nucleus create large figures of the same shape at increasing of the film thickness. This shape is possible to explain by tetrahedral form of elementary SiC lattice. Crystallites have the same shape. The small nucleus of SiC appear directly on the substrate surface in case of island growth. Then these islands grow and turn into large islands of condense phase (Fig. 4).

Deep caverns on the substrate (Fig. 3, substrate) in 0.8–1.1 μm and 2.1–2.4 μm are steps of polishing. Fig. 4 illustrates Ostwald ripening: the small islands merge after filling the caverns between them and form the large islands. Surface morphology changes at increasing of epilayer thickness: surface is described by large growth features, the surface area with large amount of nucleation centers also grows up.

2.3. Fractal analysis of the texture

In our study, based on the performance algorithms and specific calculation used for estimating the fractal dimension, the most appropriate method of fractal analysis for the analyzed surfaces was morphological envelopes [38].

In this method [39] the upper and lower envelopes are calculated by morphological opening and closing using a structuring element which is a horizontal line segment of length ε. The graph of the calculated volume for surfaces ($V\varepsilon$) is drawn as a function of the scale (size of the structuring elements): $\ln(V\varepsilon)/\ln(\varepsilon)$. A logarithmic scale is used for the axes, but the values of the graduations are given as dimensional units. The calculated parameters are: fractal dimension, slope (slope of the regression line), and R^2 (correlation coefficient of the regression line). These parameters are calculated for two regression lines, one connecting the points to the left of the graph, the other connecting the points to the right.

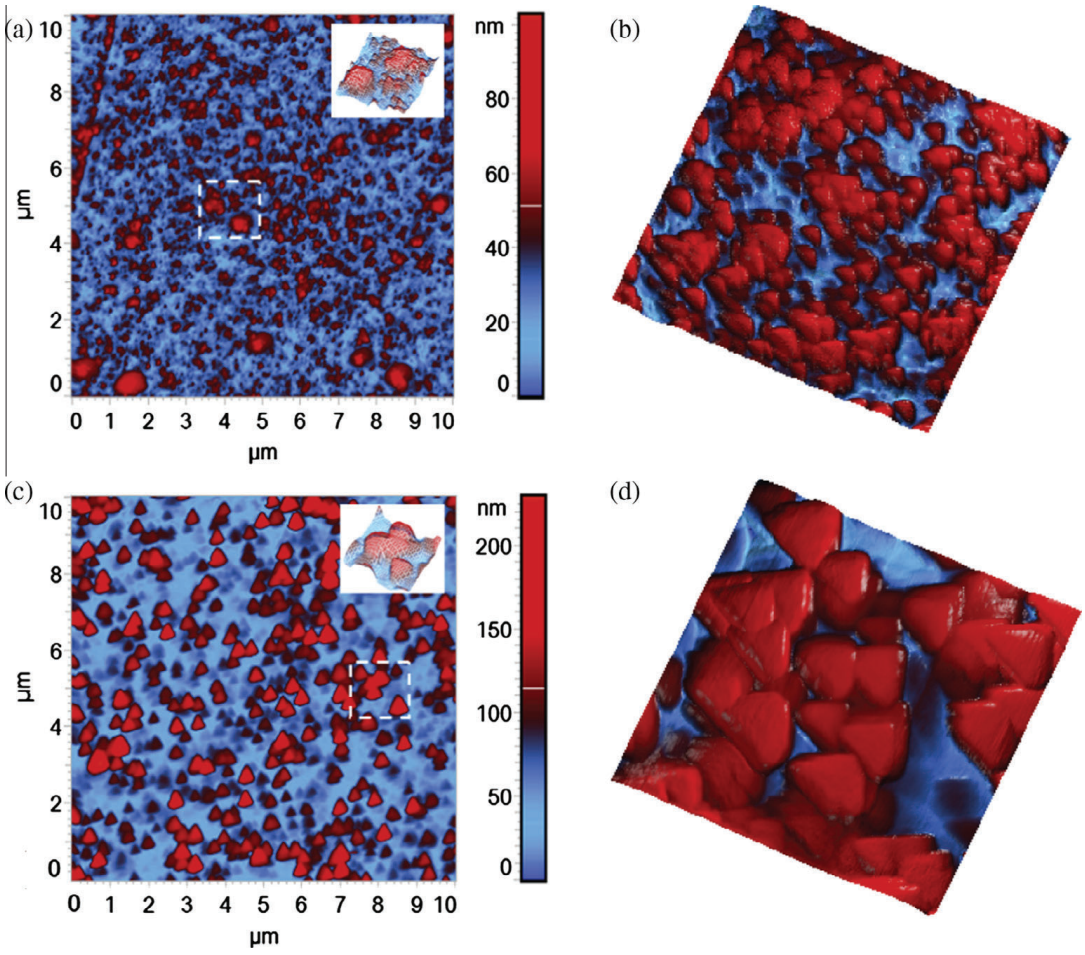

Fig. 3. AFM imaging of the B-14 sample (a and b) and B-37 sample (c and d) (10 × 10 μm^2). 3D images which are placed in the corner of 2D images (a and c) demonstrated the process of Ostwald ripening. 3D images (15 × 1.5 μm^2) of the B-14 and B-37 samples are shown in (b) and (d) respectively.

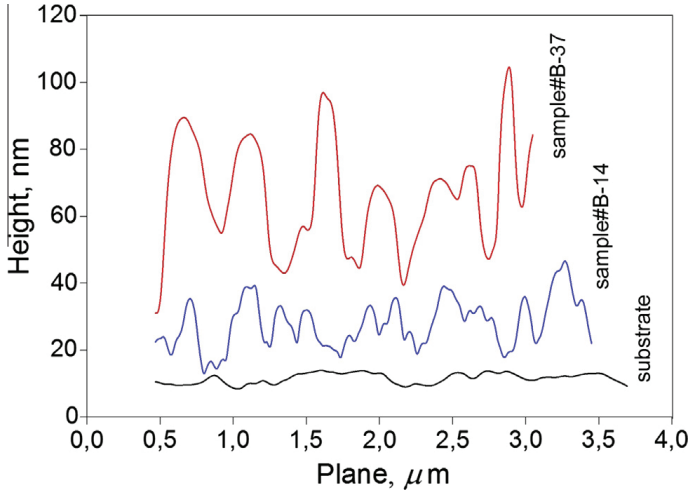

Fig. 4. Profile of growth steps: substrate, sample B-14, sample B-37. The islands coalesce with increasing of film thickness.

The AFM data from measured samples were processed by the proposed fractal analysis method, using the Mountains Map® 7 Software (Digital Surf, Besançon, France) [39].

An analysis of the stereometric files was conducted based on the original algorithm (in MATLAB software R2012b, MathWorks, Inc.) [40], which consists of fractal scaling in many approximation steps of the surface measured with an AFM. For the AFM file, every 105th, 70th, 42nd, 35th, 30th, 21st, 15th, 14th, 10th, 7th, 6th, 5th, 3rd, 2nd and 1st measuring point were selected, the whole area was measured, and 15 scalings of the surface were obtained, thus approximating its real appearance. This change of measured density is a form of surface scaling required during fractal analysis. The entire algorithm has been previously described in detail in Ref. [41].

2.4. Statistical analysis

Statistical analysis was performed using the SPSS 14 for Windows (Chicago, Illinois, USA). One-way analysis of variance was used to test the differences between the samples with two different thicknesses with Scheffé post hoc tests for multiple comparisons. The level of significance was set at $P < 0.05$.

3. Results and discussion

The watershed transform is one of best known and widely used methods for image segmentation in mathematical morphology [42].

In mathematical morphology a grey-scale image can be considered as a set of points in three-dimensional space, with the third dimension as the grey level; light and dark areas of the image may be interpreted as hills and hollows in a landscape. Applying the watershed segmentation in our study has the advantage that the resulting boundaries form closed, connected regions, which are joined to form the entire image region and adhere well to the real object boundaries.

The watershed segmentation for the analyzed surfaces is shown in Fig. 5. The segmentation method is based upon the application of a watershed algorithm, in which all peaks and hollows and passes, as well as their associated structures (hills, valleys, contours of dales and pits) are identified.

A 3D rough surface is covered by nano-asperities having different geometries with different orders of size. The surface irregularity distribution changes depending on the analyzed region, e.g. concentration of large surface irregularities occurs only in a few places and concentration of small irregularities, in many places (Fig. 4).

Fig. 3 and 4 also demonstrates the depth of the topography and it is noticeable that the bottom between gains is not completely smooth. Comparison of fractal dimension illustrates the boundary extension during growth. This pattern is a clear indication of the fractal nature of the real surface due to the manufacturing process and can be global characterized by fractal dimension. However, the surface micrograph of the epitaxial epilayers for all samples indicates that the surface is smooth and void-free, i.e. the grains are well crystallized and homogeneously distributed. Fractal dimension determined by morphological envelopes method of SiC epilayers is shown in Fig. 6.

Parameter mismatch of Si (1 1 1) substrate and 3*C*-SiC crystal lattices is compensated by changing of the layer cell sizes. Thereby, the layer is biaxial stressed at the beginning of growth process and the interface is coherently conjugate with substrate. Then the strain energy (which is accumulated in film) relaxes in proportion to thickness of the growing layer. Epilayer 3*C*-SiC becomes high oriented. Thus, it is possible to manufacture low defect SiC layers on silicon substrates by magnetron sputtering. Technology, described in Ref. [18], allows decreasing the defect density of SiC/Si structure by contribution of

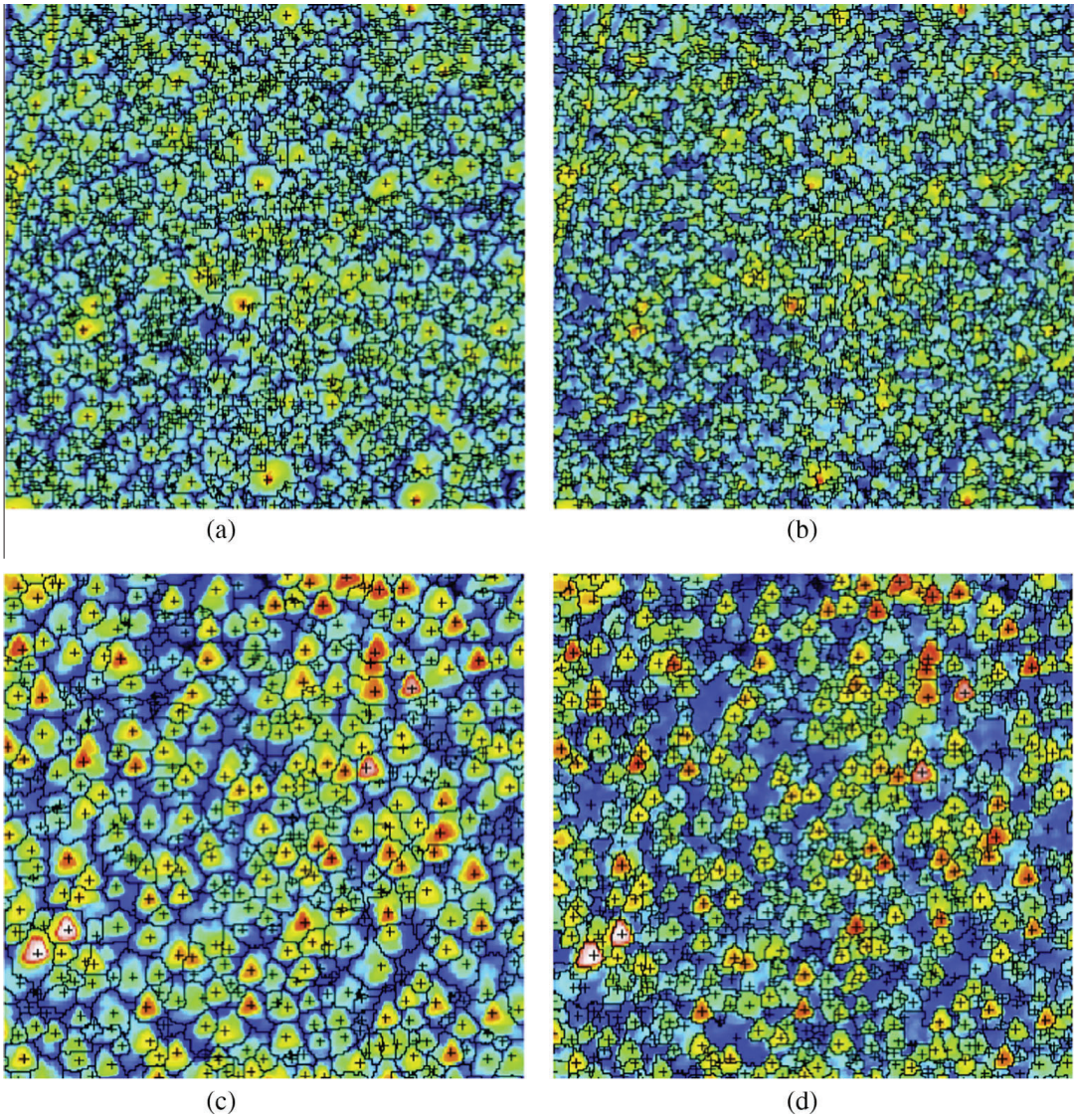

Fig. 5. The watershed segmentation for the analyzed surface, a and b sample B-14, c and d sample B-37 (a, c – detection the peaks; b, d – detection the shapes).

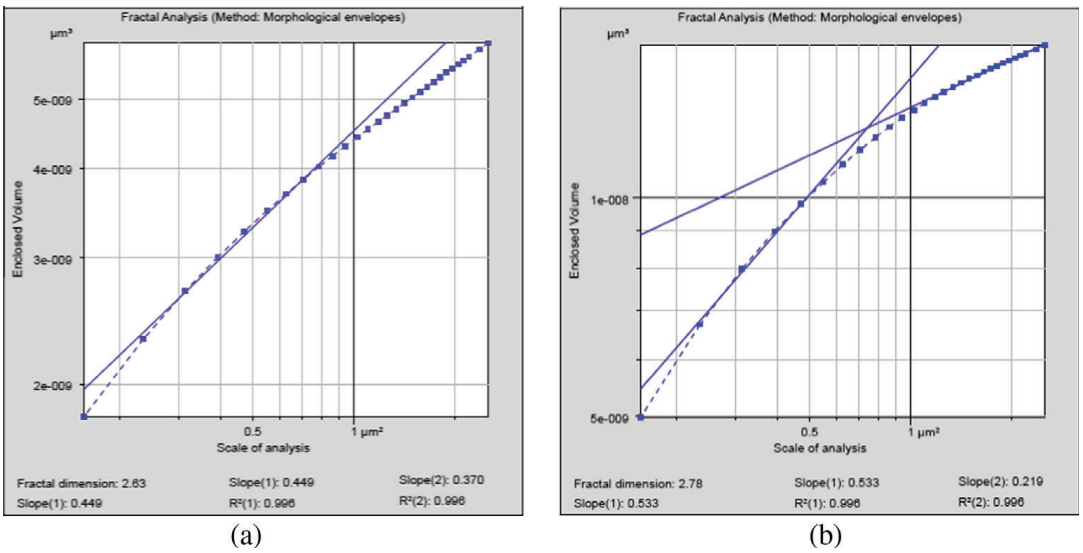

Fig. 6. Fractal dimension determined by morphological envelopes method of SiC epilayers for samples with: (a) B-14 and (b) B-37.

addition energy to the surface of the growing film. Evolution of SiC film occurs during the growth and decrease macrostresses in heterobound with Si substrate.

The fractal dimension (average ± standard deviation) of the SiC epilayers surface (Fig. 6) for sample B-14 is $D = 2.63 \pm 0.01$, while for sample with B-37 is $D = 2.78 \pm 0.01$.

Analysis and comparison of the results represent the fractal dimension as a function of film thickness or a time of the film growth process. D parameter is inversely proportional to the free energy value in the grown 3C-SiC film. The film is completely strained at $D = 2$ (single atomic layer on the substrate). The film has a layer growth at $D = 3$ (Stranski–Krastanov growth mode).

It is necessary to study regularity of technical features and changing of free energy in order to understand the model which describes the connection of fractal dimension and film growth.

Taking into consideration data from Fig. 4 such as number of motifs and profiles of films it is possible to conclude that lower the fractal dimension the larger the surface area (and consequently the important parameters which depend on it and describe the energy in the phase boundary).

Study of fractal dimension of such structures allows to predict the future properties in dependence of film thickness since fractal dimension is closely connected to material structure. Roughness of the surfaces also characterizes the micromorphology and corresponds to the films thickness (Fig. 4) but fractal analysis and watershed segmentation allow to describe the structure evolution.

4. Conclusions

The purpose of this work was to investigate evolution of 3D surface micromorphology of epitaxial epilayers at two different thicknesses in order to get insight into their microscopic formation mechanisms. For the first time SiC epilayers are deposited on Si substrate by magnetron sputtering with constant current. Noted, that energy of ionized particles promotes mean free path extension during sputtering and growth of high-oriented SiC on Si substrate.

The research in this field is focused to the development of low cost materials with superior properties allowing the fabrication of devices with improved performance. There is a need for atomic-scale methods in 3D films surfaces investigation and to try to link atomic-scale observations with macroscopic continuum models and experimental results, particularly concerning films structure and texture.

Modeling of this structures evolution has a practical importance since it help to grow low defect structures. The fractal dimension of the 3D surfaces can be used as an index not only for characterizing of the 3D surface micromorphology but also for comparison of the result of image reconstruction with the actual fracture surface morphology.

The fractal analysis reveals the existence of self-similar and fractal characteristics in the surface morphologies which are reliable metrics of surface roughness.

The processed experimental results show that at $D = 2.63 \pm 0.01$ the value of FWHM = 0.46° (sample B-14), and at $D = 2.78 \pm 0.01$ the value of FWHM = 0.18° (sample B-37). The results allow correlating the features of the growing film surface with structural properties of volume. Fractal dimension is inversely proportional to the value of the free energy in the growing film until the change of island growth mode to layer mode.

5. Declaration of interest

The authors claim to have no financial interest, either directly or indirectly, in the products or information listed in the article. The authors alone are responsible for the content and writing of the paper.

Acknowledgements

Research described in the paper was financially supported by the European Centre of Excellence CEITEC CZ.1.05/1.1.00/02.0068, by project Sensor, Information and Communication Systems SIX CZ.1.05/2.1.00/03.0072, Visegrad Fund. As well as State assignments no. 2560 and no. 16.1103.2014K.

References

[1] R. Goswami, C.H. Li, G.G. Jernigan, P.E. Thompson, C.S. Hellberg, B.T. Jonker, Acta Mater. 65 (2014) 418.
[2] J.H. Park, J.H. Park, B.T. Lee, Mater. Lett. 64 (2010) 1137.
[3] S.H. Chang, Y.K. Fang, K.C. Hsu, T.C. Wei, Sens. Actuat. A 147 (2008) 1.
[4] Y. Zhou, G. Pan, X. Shi, G. Luo, Z. Gu, Surf. Coat. Tech. 251 (2014) 48.
[5] A. Barna, S. Gurban, L. Kotis, J. Labar, A. Sulyok, A.L. Toth, M. Menyhard, J. Kovac, P. Panjan, Appl. Surf. Sci. 263 (2012) 367.
[6] Y. Wang, L. Wang, Q. Xue, Appl. Surf. Sci. 257 (2011) 10246.
[7] L. Li, Z. Chen, Y. Yang, Mater. Lett. 65 (2011) 1257.
[8] P. Ortega, I. Martın, G. Lopez, M. Colina, A. Orpella, C. Voz, R. Alcubilla, Sol. Energy Mater. Sol. Cells 106 (2012) 80.
[9] M. Syvajarvi, R. Yakimova, E.A.M. Johansson, A. Henry, Q. Wahab, C. Hallin, E. Janzen, Mater. Sci. Eng. B61–62 (1999) 147.
[10] C. Yang, Z. Chen, W. Liu, X. Zeng, Mater. Sci. Semicond. Process. 16 (2013) 1765.
[11] L.M. Sorokin, N.V. Veselov, M.P. Shcheglov, A.E. Kalmykov, A.A. Sitnikova, N.A. Feoktistov, A.V. Osipov, S.A. Kukushkin, Techn. Phys. Lett. 34 (2008) 992.
[12] Sh.M. Ramazanov, M.K. Kurbanov, G.K. Safaraliev, B.A. Bilalov, N.I. Kargin, A.S. Gusev, Techn. Phys. Lett. 40 (2014) 300.

[13] G. Sclauzero, A. Pasquarello, Appl. Surf. Sci. 291 (2014) 64.
[14] I. Deretzis, A. La Magna, Appl. Surf. Sci. 291 (2014) 69.
[15] C. Celebi, C. Yanık, A.G. Demirkol, Ismet I. Kaya, Appl. Surf. Sci. 264 (2013) 56.
[16] B. Gupta, M. Notarianni, N. Mishra, M. Shafiei, F. Iacopi, N. Motta, CARBON 68 (2014) 563.
[17] S.A. Kukushkin, A.V. Osipov, Phys. Solid State 50 (2008) 1238.
[18] Sh.M. Ramazanov, G.M. Ramazanov, Techn. Phys. Lett. 40 (2014) 44.
[19] Ş. Ţălu, A.J. Ghazai, S. Stach, A. Hassan, Z. Hassan, M. Ţălu, J. Mater. Sci. Mater. El. 25 (2014) 466.
[20] Y.R. Jeng, P.C. Tsai, T.H. Fang, Microelectron. Eng. 65 (2003) 406.
[21] D. Dallaeva, Ş. Ţălu, S. Stach, P. Škarvada, P. Tománek, L. Grmela, Appl. Surf. Sci. 312 (2014) 81, http://dx.doi.org/10.1016/j.apsusc.2014.05.086.
[22] S. Du, Y. Li, Chin. J. Mech. Eng. 26 (2013) 137.
[23] Ş. Ţălu, S. Stach, A. Mahajan, D. Pathak, T. Wagner, A. Kumar, R.K. Bedi, Surf. Interf. Anal. 46 (2014) 393, http://dx.doi.org/10.1002/sia.5492.
[24] Ş. Ţălu, S. Stach, J. Zaharieva, M. Milanova, D. Todorovsky, S. Giovanzana, Int J Polym Anal. Ch. 19 (2014) 404, http://dx.doi.org/10.1080/1023666X.2014.904149.
[25] Ş. Ţălu, S. Stach, S. Valedbagi, S. Mohammad Elahi, R. Bavadi, Mater. Sci. Poland 33 (2015) 137, http://dx.doi.org/10.1515/msp-2015-0010.
[26] Ş. Ţălu, S. Stach, Polym. Eng. Sci. 54 (2014) 1066, http://dx.doi.org/10.1002/pen.23650.
[27] Ş. Ţălu, S. Stach, S. Solaymani, R. Moradian, A. Ghaderi, M.R. Hantehzadeh, S.M. Elahi, Ż. Garczyk, S. Izadyar, J. Electroanal. Chem. 749 (2015) 31, http://dx.doi.org/10.1016/j.jelechem.2015.04.009.
[28] Ş. Ţălu, S. Stach, T. Ghodselahi, A. Ghaderi, S. Solaymani, A. Boochani, Ż. Garczyk, J. Phys. Chem. B 119 (2015) 5662, http://dx.doi.org/10.1021/acs.jpcb.5b00042.
[29] Ş. Ţălu, S. Stach, A. Méndez, G. Trejo, M. Ţălu, J. Electrochem. Soc. 161 (2014) D44, http://dx.doi.org/10.1149/2.039401jes.
[30] Ş. Ţălu, S. Stach, M. Ikram, D. Pathak, T. Wagner, J.M. Nunzi, Int. J. Nanosci. 13 (2014) 1450020–1450021, http://dx.doi.org/10.1142/S0219581X14500203.
[31] Ş. Ţălu, Anim. Biol. Anim. Husb. 4 (2012) 1.
[32] Ş. Ţălu, S. Stach, A. Mahajan, D. Pathak, T. Wagner, A. Kumar, R.K. Bedi, M. Ţălu, Electron. Mater Lett. 10 (2014) 719, http://dx.doi.org/10.1007/s13391-013-3270-4.
[33] Ş. Ţălu, Z. Marković, S. Stach, B.T. Marković, M. Ţălu, Appl. Surf. Sci. 289 (2014) 97, http://dx.doi.org/10.1016/j.apsusc.2013.10.114.
[34] S. Stach, D. Dallaeva, Ş. Ţălu, P. Kaspar, P. Tománek, S. Giovanzana, L. Grmela, Mater. Sci. Poland. 33 (2015) 175, http://dx.doi.org/10.1515/msp-2015-0036.
[35] R.K. Leach, Fundamental Principles of Engineering Nanometrology, Elsevier Inc., Oxford, UK, 2010.
[36] AFM «Golden» silicon probes. <http://www.ntmdt-tips.com> (accessed 03.07.15).
[37] K. Reichelt, Vacuum 38 (1988) 1083.
[38] S. Lou, X. Jiang, P.J. Scott, Measurement 46 (2013) 1002.
[39] MountainsMap® 7 Software (Digital Surf, Besançon, France). Available from: http://www.digitalsurf.fr (accessed 03.07.15).
[40] S. Stach, S. Roskosz, J. Cybo, J. Cwajna, Mater. Charact. 60 (2009) 1151.
[41] A. Chhabra, R.V. Jensen, Phys. Rev. Lett. 62 (1989) 1327.
[42] J. Nikodem, Comput. Inform. 28 (2009) 1001.

Appendix 4

Form № 01 IZ-2014

FEDERAL SERVICE FOR INTELLECTUAL PROPERTY
(ROSPATENT)

Berezhkovskaya emb., 30, bldg. 1, Moscow, G-59, GSP-3, 125993. Phone (8-499) 240-60- 15. Fax (8-495) 531-63-18

To № - from –
Our № 2018139626/05(065797)
For all correspondence, please refer to the application number
Outgoing correspondence from

14.02.2020

"SIKLAB" Ltd.
st. Magomed Yaragsky, 75 g
Makhachkala
Dagestan republic
36700

D E C I S I O N
on issuing a patent for an invention

(21) Application № 2018139626/05(065797) (22) Date of the application 11.11.2018

As a result of the application examination for the invention, it was essentially established that the claimed invention is related to objects of patent rights, meets the conditions of patentability, the essence of the claimed invention (inventions) in the documents of the application is disclosed with the fullness sufficient for the implementation of the invention (inventions) *, and therefore the decision was made to grant a patent for the invention.

The conclusion on the results of the examination is attached.

Application: 4 pages. In 1 copy

Head of
Public Services

Organization

The document is electronically signed
Information about the ES certificate
Certificate
011C377A0017AB0BA94AB0DB8BE2A6E57F
Owner Travnikov
Dmitry Vladimirovich
Validity from 12/02/2019 to 07/27/2033

Travnikov D.V.

**Verification of description sufficiency of the essence of the claimed invention is carried out on applications for*

Address for correspondence with the patent holder or his representative, which will be published in the official bulletin

indicated on the front side of the decision form

inventions submitted after 01.10.2014

Appendix to form No. 01 IZ-2014
10

CONCLUSION ON THE EXAMINATION RESULTS

(21) Application No. 2018139626/05 (065797) (22) Date of application submission 11.11.2018
(24) Date of the patent validity countdown start 11.11.2018

PRIORITY SET BY DATE

(22) applying 11.11.2018

(72) Author (s) Ramazanov Shikhgasan Muftyalievich, Gammataev Said Limatulaevich, Rizvanov Ilmar Gulimetovich, Ramazanov Guseyn Muftyalievich, Sobola Dinara Sultanovna, RU

(73) Patent holder(s) SIKLAB Limited Liability Company, RU

(54) Title of the invention A method for producing aluminum nitride thin films in the mode of molecular layering

(See overleaf)

01	2	DOM 02.02.2020	051009

ATTENTION! In order to eliminate errors, please check the information provided in the conclusion, as they will be entered into the State Register of Inventions of the Russian Federation without change, and immediately report any errors found.

Address for patent indicated on the front side of the decision form

As a result of the substantive examination of the application, carried out in accordance with Article 1386 and paragraph 1 of Article 1387 of the Civil Code of the Russian Federation, enforced by Federal Law of March 12, 2014 No. 35-FZ (hereinafter referred to as the Code), with respect to the claims specified by the applicant, the compliance of the claimed invention with the requirements of Article 1349 of the Code, the patentability conditions established by Article 1350 of the Code, and the compliance of the application documents with the requirement of description sufficiency of the invention essence established by Volume 2 of Article 1375 of the Code.

Invention formula is given on page(s) 3.

Form № 01a

(21) 2018139626/05

(51) IPC

C30B 25/22 (2006.01)	**C23C 16/34** (2006.01)	**H01L 21/365** (2006.01)
C30B 29/38 (2006.01)	**C23C 16/455** (2006.01)	**B82B 3/00** (2006.01)
C30B 29/40 (2006.01)	**C23C 16/46** (2006.01)	**B82Y 40/00** (2011.01)
C23C 16/18 (2006.01)	**C23C 16/56** (2006.01)	

(57)

1. A method of producing thin films of aluminum nitride in the molecular layering mode at a substrate heating temperature of up to 260 ° C using a trimethylaluminum ($Al(CH_3)_3$) precursor as an aluminum source and characterized in that hydrazine (N_2H_4) or hydrazine chloride (N_2H_5Cl) is used as a nitrogen source followed by annealing the resulting structure at temperatures up to 1400 ° C in N_2 atmosphere for up to 2 hours.

2. The method according to clause 1, characterized in that hydrazine chloride (N_2H_5Cl) is used as a nitrogen-containing precursor.

3. The method according to clauses 1 and 2, characterized in that the sapphire with r- plane to the surface is used as the substrate.

(56) TARALA, V.A. et al., The growth of oriented AlN films on sapphire substrates by the method of plasma-activated atomic layer deposition "Letters in ZhTF", 2017, Volume 43, Issue 1, pp. 67-70; DEBORAH A. NEUMAYER et al., Growth of Group III Nitrides. A Review of Precursors and Techniques, "Chem. Mater.", 1996, 8, pp 22, 24; Abdugalatov A.I. et al., Atomic layer deposition of aluminum nitride and oxynitride on silicon using tris(dimethylamido)aluminum, ammonia, and water, Journal of General Chemistry, 2018.V. 88, no. 8, p. 1385;

JERZY F. JANIK et al., The systems $LiAlH_4$ / NH_4X and N2H5Cl as precursor sources for AlN, Journal of Organometallic Chemistry, 1993, Vol.449, No.1-2, p 42; RU 2448204 C2, 04.20.2012.

When publishing information on patent issuing, the initial description of the applicant will be used.
When publishing information on patent issuing, an abstract corrected by an expert will be used.
When publishing information on patent issuing, the original drawings will be used.

Appendices: 1) A notice on the procedure for payment of patent fees levied for registration of an invention, utility model, industrial design and grant of a patent, as well as for maintaining a patent, is on p.1, in 1 copy

2) Abstract, corrected by an expert, is on p. 1, in 1 copy

Chief State
Intellectual Property
Expert of the Department of
Inorganic and Polymer
78
Compounds FIPC

Pisareva E.D.

The document is electronically signed
Information about the ES certificate
Certificate
017CE68A0043AB20964BD8059A1ABFC706
Owner Kodinets
Nadezhda Vladimirovna
Validity from 15/01/2020 to 07/27/2033

Kodinets N.V.
8 (499) 243-76-

Publish with fig. № - No. - Appendix No. 2

To application № 2018139626/05

(54) Method for producing thin films of aluminum nitride in molecular layering mode

Abstract

(57) The invention is related to the field of micro- and nanoelectronics, more particularly, to a technology for producing epitaxial films of aluminum nitride, and can be applied in the field of acousto- and optoelectronics. The method consists in deposition of AlN layer by molecular layering on a sapphire substrate at temperatures up to 260 °C using trimethylaluminum ($Al(CH_3)_3$) precursors as a source of aluminum atoms and hydrazine (N_2H_4) or hydrazine chloride (N_2H_5Cl) as a nitrogen-containing precursor followed by annealing the resulting structure in an atmosphere of molecular nitrogen at temperatures up to 1400 °C. The invention allows providing the minimum possible thickness of the applied layer with high quality characteristics, starting from the growth boundary of the film-substrate, and a constant film thickness over the entire surface of the substrate. 2 formulas, 2 illustrations, 2 misc.

Desk officer Pisareva E.D.

The method of producing thin films of aluminum nitride in the mode of molecular layering

The invention is related to the field of micro- and nanoelectronics, and more particularly to methods for producing epitaxial films, and can be applied in the field of acousto- and optoelectronics, as well as in the production of nitride semiconductor devices. The inventive method for producing epitaxial films of aluminum nitride, which consists in the formation of an AlN layer on a sapphire substrate by molecular layering using precursors of trimethylaluminum ($Al(CH_3)_3$) as a source of aluminum atoms and hydrazine (N_2H_4) or hydrazine chloride (N_2H_5Cl) as nitrogen-containing precursor, followed by annealing the resulting structure in the atmosphere of molecular nitrogen at the temperature range of 1200 °C – 1450 °C.

The invention allows providing the smallest possible thickness of the applied layer with high quality characteristics starting from the film-substrate growth boundary, as well as constant film thickness over the entire surface of the substrate.

A known method of chemical vapor deposition of organometallic compounds referred to in the literature as Metal-organic Chemical Vapor Deposition (MOCVD). There are structurally different reaction chambers and methods for synthesizing aluminum nitride films described in US 2002/0094682 A1 and in the study of Chun-Pin Huang et. al. (High-quality AlN grown with a single substrate temperature below 1200 ° C, Sci Rep. 2017; 7: 7135). Traditionally this method utilizes such precursors as trimethylaluminium (TMA) and ammonia (NH3) which require a high deposition temperature of more than 500 °C, furthermore, the resulting films are not homogenous in composition and thickness.

In most of these methods, the processes of condensation, film growth, crystallization of the material occur spontaneously or, in other words, as a result of the self-organization of the substance. The processes, composition and structure of the product are controlled by changing conditions such as temperature, vapor pressure or solution concentration, contact time, external electric and magnetic fields.

However, synthesis by molecular layering (called atomic layer deposition (ALD) in literature), unlike other deposition methods, takes place not as a result of chaotic interatomic, intermolecular interaction of the reagents, but by transferring and fixing certain structural units to advance prepared surface in accordance with the synthesis program, thereby allowing the construction of materials with desired properties.

In the literature, there is a method called Plasma Enhanced Atomic Layer Deposition which is a molecular layering method using a metal aluminum precursor in combination with N_2 as a source of nitrogen atoms that is pre-split into atoms (Sadeghpour et. Al, Crystalline growth of AlN thin films by atomic layer deposition, 2016 J. Phys .: Conf. Ser. 757 012003). The first disadvantage of this method lies in the fact that it requires an advanced module for the breakdown of molecular nitrogen which is fairly difficult to come by. Another disadvantage is the uncontrollability of the ratio of split nitrogen on the surface of the resulting layer. Quality of the obtained aluminum nitride films is insufficient to be called

epitaxial, and a large number of parasitic phases formed due to the plasma flow of nitrogen have been noticed in the resulting structures.

In the work of Cagla Ozgit et. al (Self-limiting low temperature growth of crystalline AlN thin films by plasma-enhanced atomic layer deposition, Thin Solid Films 520 (2012) 2750–2755) on silicon substrates using plasma-enhanced atomic layer deposition with TMA and NH_3 as precursors, aluminum nitride films were obtained at relatively low growth temperatures from 185 °C to 200 °C. The disadvantage of this method is the use of ammonia as a nitrogen-containing chemical which in turn forms residual ligands in the growth chamber and the plasma stream destroys them into constituent atoms affecting the quality of the resulting film. The difficulty of controlling the processes occurs in a gaseous medium above the substrate material. Thus, the obtained films were of polycrystalline quality.

Xinye Liu et. al (Atomic Layer Deposition of Aluminum Nitride Thin films from Trimethyl Aluminum (TMA) and Ammonia, MRS Online Proceeding Library Archive, 2004), where, used PEALD and thermal ALD methods in the temperature range of 370 °C – 470 °C. The same precursors were used in the process - TMA and NH_3. The disadvantage of this method is the relatively high temperature of producing films of aluminum nitride, and the use of ammonia as a nitrogen-containing precursor does not allow obtaining high-quality AlN layers. This technical solution is taken as a prototype of the invention.

The main objective of the invention is to optimize the technology of molecular layering of aluminum nitride thin films.

The essence of this invention is the method of producing epitaxial films of aluminum nitride, which consists in the formation of an AlN layer on a sapphire substrate by molecular layering using precursors of trimethylaluminum ($Al(CH_3)_3$) as a source of aluminum atoms and hydrazine (N_2H_4) or hydrazine chloride (N_2H_5Cl) as nitrogen-containing precursor, followed by annealing the resulting structure in an atmosphere of molecular nitrogen at a temperature of from 1200 °C to 1450 °C.

The specified technical result is achieved by choosing hydrazine as an alternative nitrogen-containing precursor due to its more favorable thermochemical characteristics. The difference in the reactions is well illustrated by the changes in the enthalpy ΔH and Gibbs energy ΔG for the dissociation of NH_3 and N_2H_4:

$NH_3(g) \rightarrow NH_2(g) + H(g)$; $\Delta H = 108.5$ Kcal, $\Delta G = 100.9$ Kcal;

$N_2H_4(g) \rightarrow 2NH_2(g)$; $\Delta H = 68.1$ Kcal, $\Delta G = 58.4$ Kcal.

The detailed description of AlN formation in this method is given below.

Example 1. The deposition was carried out on the ALD CERAM ML-200 equipment. Prepared single crystal sapphire substrates are placed in a vacuum chamber. The substrates are polished on one side and have r-plane to the surface. The substrates were cleaned with acetone, isopropanol and dried with a stream of high-purity flowing nitrogen. The preliminary vacuum in the chamber is 10^{-3} Pa. The substrate is heated to a temperature of 250 °C. In total, 200 cycles of molecular layering were carried out with the following parameters: TMA introduction time was 3 seconds follow by purging stage in an inert gas (N_2) for 25

seconds, the next stage is the introduction of N_2H_4 lasting 0.3 seconds. After deposition the resulting structures were subjected to high-temperature annealing at 1320 °C in nitrogen atmosphere.

Example 2. The deposition was carried out on the ALD CERAM ML-200 equipment. Prepared single crystal sapphire substrates are placed in a vacuum chamber. The substrates are polished on one side and have r-plane to the surface. The substrates were cleaned with acetone, isopropanol and dried with a stream of high-purity flowing nitrogen. The preliminary vacuum in the chamber is 10^{-3} Pa. The substrate is heated to a temperature of 260 °C. In total, 250 cycles of molecular layering were carried out with the following parameters: TMA introduction time was 4 seconds, follow by purging stage in an inert gas (N_2) for 30 seconds, the next stage was N_2H_5Cl introduction with duration of 0.5 sec. The container with N_2H_5Cl was heated to 89 ° C. After the deposition, the resulting structures were subjected to high-temperature annealing at 1400 °C in nitrogen atmosphere.

The figure 1 shows the X-ray diffraction pattern of the obtained AlN/Al_2O_3 structure where peaks from the sapphire substrate of the r-plane with d = 0.3466 nm are visible at 2θ [012] = 25.681 degrees. and d = 0.1733 nm at 2θ [024] = 52.779 degrees For AlN film, d = 0.156 nm at 2θ [110] = 59.379 degrees, the relative difference from the standard value d = 0.1541 nm at 2θ [110] = 59.983 (data from the ICSD card 98-008-2790) is less than 0.002 nm. The half-width at half the amplitude of the reflex from AlN [110] was 885 arcsec, with a film thickness of less than 20 nm, which corresponds to good quality at the initial stage of growth of the epitaxial layer.

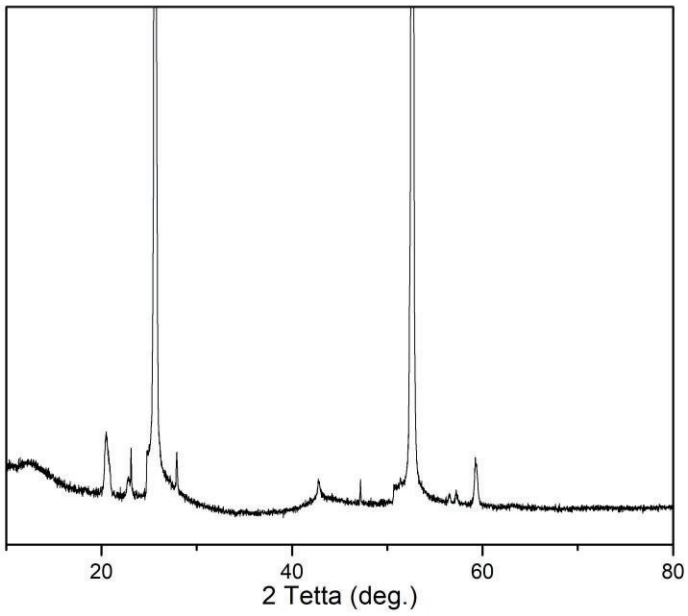

Figure 1. X-ray diffraction pattern of the obtained AlN/Al_2O_3 structure

Figure 2 shows a cleavage of the AlN / Al2O3 structure obtained by high resolution transmission electron microscopy. It can be seen from the figure that no germinating dislocations and parasitic phases were detected at the film-substrate interface.

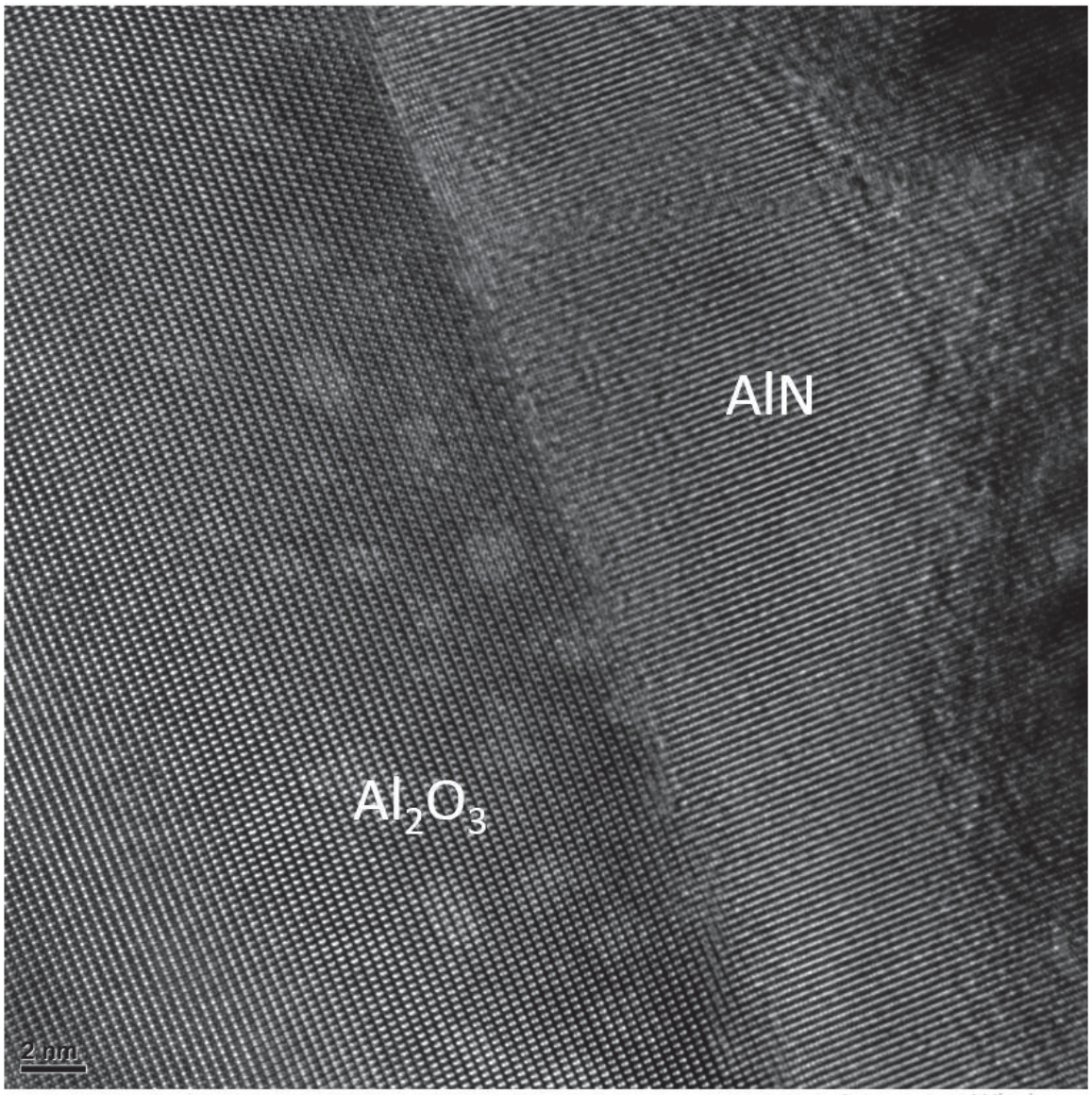

Figure 2. High resolution transmission electron microscopy of the AlN/Al_2O_3 structure

Experiments have shown that at deposition temperatures from 180 °C to 250 °C, the surface reactions of TMA and N_2H4 or N_2H_5Cl are self-limited. AlN films grown using N_2H_4 have a higher density and lower impurity content. These facts indicate that hydrazine is the best nitrogen carrier in the production of AlN films in comparison with ammonia.

The invention allows providing the smallest possible thickness of the applied layer with high quality characteristics starting from the film-substrate growth boundary, as well as a constant film thickness over the entire surface of the substrate.

Appendix 5
WOS: 000476663600109

Advances in Economics, Business and Management Research, volume 81
1st International Scientific Conference "Modern Management Trends and the Digital Economy: from Regional Development to Global Economic Growth" (MTDE 2019)

Micro-courses for education to scanning probe microscopy

Talu S.
Technical University of Cluj-Napoca
Cluj-Napoca, 400020, Cluj county, Romania
E-mail: stefan_ta@yahoo.com

Sobola D.
Brno University of Technology, Faculty of Electrical Engineering and Communication
Brno, 616 00, Czech Republic
E-mail: sobola@vutbr.cz

Dallaev R.S.
Brno University of Technology, Faculty of Electrical Engineering and Communication
Brno, 616 00, Czech Republic
E-mail: xdalla03@vutbr.cz

***Abstract* — This paper describes impact of micro-courses to education in the field of the nanoscience. The feature of the subjects which are related to nanoscience is the combination of new modern research methods and the foundations of physics and chemistry. While there are well-developed textbooks to study the fundamentals, it is necessary to refer to freshly written articles of scientists and data from technical sites. Rapidly developing fields demands flexibile form of materials to study and an innovative change in the presentation of an online environment. Here we consider education to scanning probe microscopy techniques in terms of micro courses. This type of microscope is became an important tool for three dimensional surface studies with nanoscale resolution.**

Keywords — teaching, studying, nanoscience, micro-course

I. INTRODUCTION

The widespread introduction of high technologies and the openness of the learning process are gaining more and more space in the higher education, in order to develop of highly complex knowledge structures, generic skills as well as transferability of knowledge and skills to future professional work [1-3]. The trend of the modern learning process, for the effective assimilation of material along with classical teaching, a strong place is occupied by micro-courses [4].

The micro-course concept is aimed at obtaining and fixing certain knowledge and skills by the student, being an instrument of internal learning. The step-by-step constructed algorithm will allow to optimize the learning tasks to a greater extent, to structure the information contained in this micro-course of microscopy. The volume course of the training material is given in small doses, one topic is one course, which simplifies the control over the assimilation of the educational material. The time allotted for the video lesson or short lecture is from 5-10 minutes, it is the time interval when the concentration is maximum, hence the probability of obtaining a satisfactory result is high. A logically constructed chain consisting of a set of interrelated topics, with the correct design of the curriculum, creates favorable conditions for memorization.

Efficient SPM education involves wide range of activities from operator-level problem solving to training specialist for research activities. Currently, there are a large number of manufacturers of the microscopes. The scope of microscopy provides ample opportunity to study nanostructures. In addition to high-quality and quantitative surface analysis, modern microscopes are equipped with additional devices for modifying and engineering the surface of samples. Students need to understand the advantages and limitations of the applicability of the technologies introduced in the market for SPM microscopes. Considering specificity of this modern field of study, new education methods should be applied in order to fulfill expectations of future employee [5].

II. MOTIVATION FOR IMPLEMENTATION OF MICRO-COURSES

Students will constantly remember what they learned earlier, and receive new information. New information will be placed on a newly formed database and be perceived much more efficiently [2].

The motivation for micro-studying is relevant factors such as: visibility and availability of the material, saving time, choice of the level of training, the opportunity to learn without interrupting work, learning small parts is easier, availability (using different types of communication, regardless of location); no dependence on external circumstances; unlimited viewing; visual memory is involved. As part of the implementation of adaptive learning using micro-course, it is important to cover all the issues: how the program is arranged, the conditions for switching from one module to another, how long it will take. The main aspect is full transparency as you progress through the course of the program, the ability to display progress in the percentage or percentage ratio, which is a stimulating factor in mastering the material.

In one video lesson, a lot of information is concentrated, which is perceived, both visually and by ear, which is very effective. With the video material everyone can learn and everything is basically clear.

III. Design of micro-courses in microscopy teaching

The scanning probe microscopy can be applied to various problems in a wide range of disciplines of the natural sciences, including solid-state physics, semiconductor science and technology [6-8], molecular engineering, polymer chemistry and physics [10, 11], surface chemistry [12-14], surface science [15-17], molecular biology, cell biology [18], and biomedical sciences [9, 10].

SPM is a physical interaction of a fine probe/tip with the surface of the sample to scan the surface and collect data, typically obtained as a two-dimensional grid of data points and displayed as a computer image. Teaching to SPM is complicated by the fact that this area is located at the intersection of scientific fields: engineering, fundamental science, processing of graphics. It is necessary to design the education process for teaching the student to work with the equipment, to understand the physical basis of the surface scanning and accurately process the data for extraction maximum reliable information.

The main principle in the choice of educational material for microscopy, in particular, scanning probe microscopy, is the relevance of topics and their accessibility in the understanding of the material being studied (for examples: probe-sample interface, electronics for detection of the probe-sample interaction, etc.). The concept of quality of activity includes following aspects: easy assimilation of the material; high learning efficiency at relatively low loads; ease of perception of the material. According to [4] the design of micro-coursed should contain following elements: time, objective, content, method and technology.

Modules of micro-education should contain small practical tasks that help in fixing basic and new acquired knowledge. Video course, as a visual way of information transfer, greatly facilitates the learning process and the formation of the knowledge base, which makes it easier to do self-education. With video courses, the students can learn anywhere from their mobile devices: laptops, tablets or smartphones. The video contains a maximum of useful information. To periodically monitor the assimilation of educational material and consolidate the acquired knowledge, a successful methodological tool is testing.

IV. Time allocation for SPM teaching

An important aspect of micro-course design is the distribution of the teaching time across theoretical education and practical activities.

Visual illustration is important for quick perception of information. The use of interactive presentations reduces the operation time of expensive equipment. The alternation of teaching methods: practice in the laboratory, lectures, interactive web pages, can improve the effectiveness of training. Student can pass independently though chosen theoretical parts of education material and it saves the time of the teacher.

Education time in the case of micro-courses implies its most effective use on the principle: better to keep maximum attention for a short time than to absentmindedly observe for a long time. As a result, there is a variation of studying activities during the education process.

Presence of easy-operating microscopes and accessories for demonstration of basic principles makes learning interesting and not time-consuming. Internet resources provide information about processes at the nanoscale level [19, 20] for their easier perception. Available free software (Gwyddion, ImageJ, etc.) have a number of YouTube tutorials which demonstrate data processing. Teaching model based on micro-courses implies that after determine the gaps in knowledge the student can devote more time to incomprehensible problems at any step.

V. Aims and objectives of SPM teaching

It was mentioned by R. Blonder et al. [21] that atomic force microscopy (which is one member of SPM group) attracted a lot of attention being “excitement of exploring matter at the nanoscale”. Besides this possibility of imaging the nano-topography, SPM is important of surface visualization and modification in various scientific files.

One of the main objectives of SPM teaching is explanation of correlation between SPM data and surface properties.

The basic concepts of physics and chemistry of surface in nanoscale should be explained. The aim of SPM teaching using micro courses can cover more than one SPM technique in dependence of specialization field (physics, biology, chemistry, material science). Most set-ups with they native software allows students to carry out following standard procedures: preparation to measurements: exchange of the probe, fix of the sample; measuring the samples: navigation using optical system (could be build-in optical microscope), trying different techniques (atomic force microscopy, scanning tunneling microscopy, scanning near-field optical microscopy, spectroscopy methods, etc.), trying scanning parameters (scanning rate [16], area, direction, etc.); processing of the results: evaluation of spectroscopy data; estimation of the physical values (in case of electrical, mechanical, optical measurements), image processing and extraction quantitative data (statistical data, filtering, fractal analysis [12, 14], etc.)

SPM measurements should also provide insight to features and peculiarities of the other studies in nanometer and angstrom scale. For example, the quality of the received data (images, spectroscopic data, and lithography) is influenced by external and internal noises. External noises include mechanical and acoustic vibrations of the building, ventilation, classroom conversations, electro-acoustic noise (power lines in walls, mobile phones). Internal noise is associated with the presence of mechanical and electrical elements of the microscope and depends on the instrument configuration. As every education, the SPM-teaching has the aim to provide sufficient information support for preparation well-skilled students. For this purpose, the feedback of the students should be considered. Module character of micro-courses makes them flexible and has advantages for improving quality of education.

VI. Content of micro-courses for SPM teaching

Since SPM has a great application potential from ordinary scanning of surface topography to surface modification, it is necessary to make a right choice of the measurement (or engineering) technique. Study of the principles should begin from the physical fundamentals of interaction between probe and sample surface. A set of micro-coursed at this step should

include such concepts as inter-atomic interaction (for atomic-force microscopy), tunneling effect (for scanning tunneling microcopy), wave properties of light (for scanning near-field optical microscopy), etc. On the basis of this background the specific of the suitable type of SPM should be investigated in details: choice of probes, sample preparation, conditions of measurements. Various types of SPM needs its own preparation procedure and demands in order to provide correct and reliable data.

The micro-courses of this level should include study of the probes characteristics, the methods of samples processing before measurements. Following familiarization with the tool and its software applications are aimed to demonstrate the measurements in practice. In spite the similar physical principles, the existing types can differ a lot in operation way.

A number of micro-coursed should be concentrated on description of the set-up, software of the microscope, necessary safety instructions. The special areas of this field are evaluation of results and processing of the data. In case of competent approach the important conclusions can be done.

The micro-courses should be oriented on description of possible artifacts of measurements and elimination of their negative effects and at the same time they should teach to extract maximum of useful information about the studied surface (at both visual and numeric style).

VII. Advanced methods of SPM teaching

Noting the advantages of micro courses for the training of specialists in the field of SPM, it is also worth to mention that micro-courses can be used by students at any stage of education, and also act as an independent single training program.

The integrity and consistency of a teacher's activities combined with the comprehensible hierarchy of the topics provided to students ensure achievement of the desired result. Already at the initial stages of the teaching process, a forecast for further actions and potential corrections can be made. Methods can be divided into following categories:

- Preparation - the use of micro-courses before the start of basic training - involvement into the motivational process (videos, explanation of the fundamental laws on the basis of which the microscope principle is laid down).

- Focusing - is an addition to the basic training (working on specific tasks in the laboratory and processing the data obtained).

- Consolidation - consolidation of the received information, skills and knowledge (through independent work on the instrument).

Micro-courses provide both psychological comfort (stress states are minimized) and create favorable conditions for the educational process with maximum independence in an environment of realizable possibilities (temporal, physical, physiological).

The choice of optimal teaching methods is carried out by taking into account the total amount of all intermediate decisions: principles, goals and specifics of this discipline, as a result of which knowledge transfer, reinforcement of skills, and expected learning outcomes are ensured. In this regard, micro-courses are very effective for teaching microscopy, their format simplifies knowledge transfer from person to person and delivers information to a user in small pieces that can act as independent elements, while being at the same time integrated into a common training strategy. Micro courses are also advantageous as regards to time and budget, what is especially important given the expensive equipment and the need for preliminary preparation of students for measurements.

VIII. Technology of SPM education

Not only are the content of the course, supported by appropriate methods, but also the technology of the courses preparation of great importance. The fundamental strategy of micro courses is 100% implementation of goals and objectives, consolidation of the material, the introduction of knowledge and skills in the field of nanotechnology. The proper implementation and use of micro-courses are achieved when their form (content) and the way of their introduction (techniques) are conducive to the desire to be trained in techniques of microscopy.

Educational technologies by using methods, forms, tools and techniques are always focused on the implementation of the pedagogical process with a guaranteed result.

The development of a micro-course strategy consists in:

- setting goals with an emphasis on clarity - course content is dosed;
- accessibility – speed and accessibility to any section of the course;
- evaluation - assessment of how well the given information is internalized (by doing of tasks or taking tests);
- multimedia ways of presenting material;
- use of mobile devices;
- breaking into blocks and combining microcourses into a single unit.
- The format of micro-courses taking into account modern technologies provides optimal and rational opportunities for both students and teachers:
- For students:
- Concentration - the micro-course is presented as a micro lesson (10-15 minutes), during such a short period of time the learning efficiency is at its maximum. It also allows more students to make measurements independently and with high quality.
- Web Surfing - each lesson of each course has a link to a micro-course, which is a detailed version of this lesson.
- Budget and time - on the one hand, a person gets the opportunity to pay only for the knowledge he needs, on the other - not to waste time in case the course has not met expectations.
- For teachers:
- Easy creation of micro-courses - free and fast.

- Informativeness – micro-courses can be edited, improved and adapted to user expectations.
- Income generation - (paid courses).

IX. CONCLUSION

Interdisciplinary fields need special design of education which includes modern technologies. Nanotechnology covers a wide range of engineering and science. Micro-courses are suitable approach to reach high academic level. Here we describe possible application of micro-courses for education to SPM. This methodology could be applied for other parts of education to nanotechnology. Such, single-topic parts of image processing procedures could be independently applied to a number of visualization techniques. Advanced design of micro-course ensures better understanding of the studying material at short time. The micro-courses are supposed to be useful for education of modern fast developing occupations.

Acknowledgment

Research described in the paper was financially supported by the National Sustainability Program under Grant LO1401. For the research, infrastructure of the SIX Center was used.

References

[1] https://kurso.ru/blog/e-learning/.

[2] E. Tikhomirova, Live Learning: What is e-learning and how to make it work / Elena Tikhomirova - M .: Alpina Pablisher, 2016. p. 44.

[3] R. Donnelly, and F. McSweeney, Applied E-Learning and E-Teaching in Higher Education, IGI Global: London, UK, 2009, pp. XVII.

[4] Hong-yan Shen, "Teaching design factors for micro-courses of specialized courses in university". 2017 4th International Conference on Advanced Education Technology and Management Science (Proceedings AETMS 2017). ISBN: 978-1-60595-489-9. Pp. 34-37.

[5] Ş. Ţălu, D. Sobola, and N. Papež, "Analysis and recommendations for education process of experts in the field of scanning probe microscopy". DEStech Transactions on Social Science, Education and Human Science, p. 5-9, 2017. ISSN: 2475-0042. Proceedings AETMS 2017 (2017 4th International Conference on Advanced Education Technology and Management Science, September 17-18, 2017, Shenzhen, China). ISBN: 978-1-60595-489-9.

[6] Ş. Ţălu, D. Sobola, S. Solaymani, R. Dallaev, and J. Brüstlová, "Scale-depended choice of scanning rate for AFM measurements". DEStech Transactions on Computer Science and Engineering, p. 453-459, 2018. DOI: 10.12783/dtcse/cnai2018/24197. ISSN: 2475-8841. Proceedings CNAI 2018 (2018 International Conference on Communication, Network and Artificial Intelligence, April 22-23, 2018, Beijing, China). ISBN: 978-1-60595-065-5.

[7] Ş. Ţălu, D. Sobola, N. Papež, R. Dallaev, and P. Sedlák, "Efficient processing of data acquired using microscopy techniques". DEStech Transactions on Social Science, Education and Human Science, p. 202-207, 2018. DOI: 10.12783/dtssehs/amse2018/24838. ISSN: 2475-0042. Proceedings AMSE 2018 (2018 2nd International Conference on Advances in Management Science and Engineering, June 24th-25th, 2018, Xi'an, China). ISBN: 978-1-60595-566-7.

[8] Ş. Ţălu, Micro and nanoscale characterization of three dimensional surfaces. Basics and applications. Napoca Star Publishing House, Cluj-Napoca, Romania, 2015.

[9] Ş. Ţălu, and S. Stach, "Multifractal characterization of unworn hydrogel contact lens surfaces". Polym Eng Sci., vol. 54(5), pp. 1066-1080, 2014. DOI: 10.1002/pen.23650.

[10] Ş. Ţălu, "Characterization of surface roughness of unworn hydrogel contact lenses at a nanometric scale using methods of modern metrology". Polym Eng Sci., vol. 53(10), pp. 2141-2150, 2013. DOI: 10.1002/pen.23481.

[11] S. Ramazanov, Ş. Ţălu, D. Sobola, S. Stach, and G. Ramazanov, "Epitaxy of silicon carbide on silicon: Micromorphological analysis of growth surface evolution", Superlattices Microstruct., vol. 86, pp. 395–402, 2015. DOI: 10.1016/j.spmi.2015.08.007.

[12] D. Dallaeva, Ş. Ţălu, S. Stach, P. Škarvada, P. Tománek, and L. Grmela. "AFM imaging and fractal analysis of surface roughness of AlN epilayers on sapphire substrates". Appl. Surf. Sci., vol. 312, pp. 81-86, 2014. DOI: 10.1016/ j.apsusc.2014.05.086.

[13] S. Stach, D. Dallaeva, Ş. Ţălu, P. Kaspar, P. Tománek, S. Giovanzana, and L. Grmela, "Morphological features in aluminum nitride epilayers prepared by magnetron sputtering", Mater. Sci.- Poland, vol. 33, pp. 175-184, 2015. DOI: 10.1515/msp-2015-0036.

[14] Ş. Ţălu, S. Stach, D. Raoufi, and F. Hosseinpanahi. "Film thickness efect on fractality of tin-doped In2O3 thin films". Electron. Mater. Lett. Vol. 11, pp. 749-757, 2015. DOI: 10.1007/s13391-015-4280-1.

[15] Ş. Ţălu, S. Stach, S. Valedbagi, S.M. Elahi, and R. Bavadi, "Surface morphology of titanium nitride thin films synthesised by DC reactive magnetron sputtering", Mater. Sci.- Poland, vol. 33, pp. 137-143, 2015.

[16] D. Sobola, Ş. Ţălu, S. Solaymani, and L. Grmela, Influence of scanning rate on quality of AFM image: Study of surface statistical metrics, Microsc. Res. Tech. 80, pp. 1328-1336, 2017. DOI: 10.1002/jemt.22945.

[17] Ş. Ţălu, N. Papez, D. Sobola, A. Achour, and S. Solaymani, "Micromorphology investigation of GaAs solar cells: case study on statistical surface roughness parameters". J Mater Sci-Mater El., vol. 28(20), pp. 15370-15379, 2017. DOI: 10.1007/s10854-017-7422-4.

[18] Ş. Ţălu, I.A. Morozov, D. Sobola, and P. Skarvada, "Multifractal Characterization of Butterfly Wings Scales". Bull Math Biol., vol. 80(11), pp. 2856-2870, 2018. DOI: 10.1007/s11538-018-0490-7.

[19] NT-MDT. Available https://www.ntmdt-si.com/resources/spm-principles (last accessed 10th January 2019).

[20] nanoHUB Home Page. https://nanohub.org/ (last accessed: 10th January 2019).

[21] R. Blonder, E. Joselevich, and S. R. Cohen, "Atomic Force Microscopy: Opening the Teaching Laboratory to the Nanoworld". Chemical Education Today, vol. 87(12), pp. 1290-1293, 2010. DOI: 10.1021/ed100963z..